On the understanding of organic thin film growth and the changes in structure formation induced by molecular chemical tuning

Dissertation

zur Erlangung des akademischen Grades

doctor rerum naturalium
(Dr. rer. nat.)
im Fach Physik
Spezialisierung Experimentalphysik

eingereicht an der
Mathematisch-Naturwissenschaftlichen Fakultät
Institut für Physik
Humboldt-Universität zu Berlin

von
Herrn M.Sc. Anton Zykov

Präsidentin der Humboldt-Universität zu Berlin:
Prof. Dr-Ing. habil. Dr. Sabine Kunst

Dekan der Mathematisch-Naturwissenschaftlichen Fakultät:
Prof. Dr. Elmar Kulke

Gutachter:

1. *Prof. Dr. Stefan Kowarik*
2. *Priv.-Doz. Dr. Bert Nickel*
3. *Prof. Dr. Joachim Dzubiella*

Tag der mündlichen Prüfung: 11.01.2017

Abstract

Functional organic molecules are promising for the application in future relevant technologies such as organic light emitting diodes (OLEDs), solar cells, transistors and bio-sensors. One of the processing methods to fabricate organic devices is organic molecular beam deposition. In this process, the complexly interacting molecules grow via self-assembly as thin films on a substrate. Due to the close structure-property relationship, the growth process constitutes a highly interesting and important scientific challenge for both application oriented as well as fundamental research and is the topic of the present thesis.

A primary aim of this thesis is to contribute to the quantitative understanding and analysis of organic structure formation and the non-equilibrium molecular growth process. In our experiment, we[1] focus on the growth kinetics of the prototypical PTCDI$-C_8$ molecule and pursue to rationalize its notable layer-dependent growth behavior, which manifests itself in a transition of molecular shapes and a decreased molecular island density. In an advanced X-ray scattering experiment combining growth oscillations and small angle scattering measurements, we simultaneously monitor the temporal evolution of the in- and out-of-plane film morphology. By discussing several growth regimes within the framework of nucleation theory, we evaluate the nucleation energy E_{nuc}, the attempt frequency for surface diffusion ν_0 and the size of the largest non-stable island i. While comparable studies restrict the analysis of nucleation to the 1st monolayer (ML), we utilize the smooth film growth of PTCDI$-C_8$ to investigate multilayer structures. In the 2nd ML we determine a decrease of the diffusion barrier energy E_d by 140 meV going along with a higher in-plane diffusivity. This finding explains the smaller island density, which we consistently observe from X-ray scattering experiments and atomic force microscopy measurements.

The second key objective of this work is the study on the potential of chemical tuning to control molecular thin film growth for an optimized structure and interface design. Therefore we analyze the growth of derivatives of the rod-like *para*-sexiphenyl (6P), where local dipole moments at both (6PF4) or at one end of the molecule

[1] This doctoral thesis is written by a single author. However, in accordance with the common practice in scientific publications, the first person plural form is used throughout the work.

(6PF2) are induced through fluorination. Importantly, the desired optical properties, e.g. the blue fluorescence, are preserved. Our study on the growth of the symmetrical 6PF4 on an anisotropic ZnO substrate demonstrates that fluorination can cause a significant decrease of film roughness by a factor of 2. Additionally, we find 6PF4 favoring a phase pure growth, while the untuned 6P exhibits a simultaneous growth of the β- and γ-crystal phases. A larger tilt angle, as we observe for 6PF4 molecules in upper MLs compared to 6P, is known to reduce the Ehrlich-Schwoebel barrier. In combination with the suppression of bimodal growth, this contributes to a reduced film roughness. For the asymmetrical 6PF2, grown on isotropic silicon oxide surfaces, we also achieve a beneficial film smoothing. Focusing on the nanoscale growth processes, we observe that fluorination induces an increase of seven orders of magnitude in the attempt frequency for surface diffusion, as well as an increase of the critical island size and the nucleation energy. Within the diffusion-limited aggregation regime of nucleation theory, this implies an increased E_d of 6PF2 compared to 6P. We further demonstrate that fluorination not only impacts the in-plane but also the step-down diffusivity S in the case of 6PF2.

The experimental results and conceptual methods presented in this thesis contribute new stimuli to the understanding of the molecular self-assembly. The demonstrated influence of chemical tuning on various facets of structure formation, such as film roughness, crystal phase purity and molecular diffusivities, uncovers the strong potential of this approach for steering organic growth. Therefore, the present work has implications for future research and application of functional organic thin films.

Kurzfassung

Funktionale organische Moleküle bergen ein hohes Potential für den Einsatz in zukunftsprägenden Technologien wie organischen Leuchtdioden (OLED), Solarzellen, Transistoren und Bio-Sensoren. Eines der Herstellungsverfahren beruht auf der Gasphasenabscheidung der Moleküle, die auf dem Substrat mittels Selbstorganisation zu dünnen Schichten wachsen. Auf Grund der komplexen Wechselwirkungen stellt der Wachstumsprozess sowohl für die anwendungsorientierte als auch für die Grundlagenforschung eine hochinteressante und wichtige wissenschaftliche Herausforderung dar, mit der sich die vorliegende Arbeit auseinandersetzt.

Ein primäres Ziel dieser Arbeit besteht darin, einen Beitrag zum quantitativen Verständnis des Molekül-Wachstums, welches zumeist fernab eines energetischen Gleichgewichts abläuft, zu leisten. In einem ersten Experiment liegt unser Fokus auf der Untersuchung der Wachstumskinetik des prototypischen PTCDI$-C_8$ Moleküls. Wir verfolgen das Ziel, die beträchtlichen ML-abhängigen Unterschiede im molekularen Nukleationsverhalten zu verstehen, welche sich u.a. in einer Änderung der Inseldichte und -form auswirkt. Durch innovative Kombination von Wachstumsoszillationen der Röntgenreflektivität und Kleinwinkelstreu-Experimenten, bestimmen wir simultan die Morphologieevolution in der Oberflächenebene als auch senkrecht dazu. Wir diskutieren unsere Ergebnisse unter Einbeziehung von mehreren Modellen innerhalb der Nukleationstheorie und bestimmen die Nukleationsenergie, die Bestrebungsfrequenz zur Diffusion ν_0 und die Größe i, der größten noch instabilen Insel. Während vergleichbare Studien, die Wachstumsuntersuchung auf die erste Monolage (ML) beschränken, nutzen wir das glatte Schichtwachstum von PTCDI$-C_8$ und weiten die Analyse auf Multilagen aus. In der 2. ML bestimmen wir eine Verringerung der molekularen Diffusionsbarriere E_d um 140 meV, sowie eine einhergehende erhöhte Diffusivität. Dieses Resultat erklärt die kleinere Inseldichte, die wir konsistent aus Röntgenmessungen und Rasterkraftmikroskopie-Aufnahmen finden.

Das zweite zentrale Anliegen dieser Arbeit stellt die Untersuchung von chemischer Modifikation zur Kontrolle des molekularen Dünnschichtwachstums für ein optimiertes Struktur- und Interfacedesign dar. Wir untersuchen das Wachstum von Derivaten des stäbchenförmigen *para*-sexiphenyl (6P), welche an beiden (6PF4) oder

an einem (6PF2) Molekülende fluoriniert sind. Durch diese Modifikation werden im Molekül lokale Dipolmomente erzeugt. Die anwendungsrelevanten optischen Eigenschaften von 6P, z.B. die blaue Fluoreszenz, bleiben dabei erhalten. In Studien zum Wachstum des des symmetrischen 6PF4 auf anisotropen ZnO Oberflächenzeigen wir, dass durch die Fluorinierung eine Reduktion der Filmrauigkeit um einen Faktor 2 induziert werden kann. Zusätzlich können wir zeigen, dass das 6PF4 in einer einzelnen Kristallphase wächst, während das unsubstituierte 6P paralleles Wachstum der β- und γ-Kristallphasen zeigt. Der im Vergleich zu 6P größere Kippwinkel der 6PF4 Moleküle in höheren Monolagen weist auf eine kleinere Ehrlich-Schwoebel-Barriere hin. Zusammen mit der Unterdrückung des bimodalen Wachstums unterstützen diese Faktoren ein glatteres Wachstumsverhalten. Für das Wachstum des asymmetrischen 6PF2 auf isotropen Siliziumoxid-Oberflächen finden wir einen vergleichbar starken, positiven Einfluss auf die Filmrauigkeit. Im Hinblick auf Wachstumsprozesse auf der Nanoskala, bestimmen wir im Fall von 6PF2 zudem eine um sieben Größenordnungen höhere Bestrebungsfrequenz zur Diffusion, sowie einen Anstieg in der kritischen Inselgröße und der Nukleationsenergie. Innerhalb des diffusionslimitierten Aggregationsregimes der Nukleationstheorie ermitteln wir die mit diesen Befunden korrelierte Erhöhung von E_d sowie von der Diffusivität. Weiterhin zeigen wir, dass die Fluorinierung im Falle von 6PF2 auch die Stufenkantendiffusivität S verändert.

Die experimentellen Resultate und Konzepte, die in dieser Arbeit vorgestellt werden, leisten neue Beiträge für das Verständnis von organischem Wachstum. Der demonstrierte Einfluss von chemischer Modifikation auf verschiedene Aspekte des Strukturwachstums, wie z.B. auf die Filmrauigkeit, Kristallphasenreinheit und molekulare Diffusivität, zeigt zudem das hohe Potential dieser Methode zur Steuerung des organischen Wachstums. Aus den genannten Gründen kann diese Arbeit neue Impulse für die Erforschung und spätere Anwendung von funktionalen organischen Dünnschichtsystemen setzen.

Contents

1 Introduction

The technological progress of the last several decades is strongly connected with semiconducting materials. On the basis of semiconductors, devices have been fabricated, which have changed our everyday lives in a truly revolutionary way. Personal computers, mobile phones, efficient light emitters, solar cells, which convert sun light into electric power, and many other applications have been invented just 50-70 years ago, but are now indispensable in modern, progressing societies. Looking at the evolution of the design of these devices over the years, a clear trend towards miniaturization can be observed. Higher capabilities in tinier volumes are desired and demanded. At the same time, lowering energy consumption and production costs is inevitable. Smaller, cheaper and yet always more and more efficient - approaches are needed to reach these three goals simultaneously. Taking a look on the historical progress in photovoltaics as an example, we will find that an intense research activity quickly pushes initial ideas to their limits and further optimization needs new concepts and/or new materials. A publication by Chapin *et al.* from 1954[1] on the first silicon solar cell can be regarded as a starting point for focused solar cell research and up to now this material plays the dominant role in the photovoltaic market. However, cells holding the current world record efficiency are so-called concentrator multi-junction cells, differing from the traditional silicon cell in both, the technological concept and particularly in the materials.[2] Materials, initially regarded as interesting alternatives, can quickly take a key role for overcoming existing limits.

Organic semiconductors, whose growth will be studied in this thesis, can be considered as an alternative to the conventional inorganic ones, which at the moment are prevailingly used for opto-electronic devices. Although known since the beginning of the 20^{th} century,[3] the extensive research on organic semiconductors with the focus on application has started in the mid 1990's. The interest in organic materials arises due to several reasons. Firstly, a wider application range compared to inorganic materials including, e.g. a better compatibility with flexible and stretchable substrates is expected. Potential future applications, already realized partially, are solar cells implanted in clothing and accessories like bags or rollable displays. In

contrast, devices based on inorganic semiconductors like silicon are often fabricated on rigid surfaces, which restricts their mobile usability and increases their total weight. Furthermore, organic materials carry a high potential to reduce production costs. The reason is that organics can typically be processed at much lower temperatures than inorganics and there is a high potential to implement roll-to-roll methods, such as e.g. inkjet printing,[4] which would additionally decrease the costs. But probably the most significant property of organic materials is their almost infinite chemical flexibility. Functional groups or just single atoms can be interchanged, molecular chains can be expanded or shortened, carbon single bonds can be converted into double or triple bonds. All these transformations may have an influence on the functionality of the material, e.g. on optical properties or the mobility of charge carriers.[5] In comparison to inorganics, where material tuning is mainly restricted to doping, there are incomparably more degrees of freedom to fine-tune functional properties of organics. As a result, there exists a huge variety of semiconducting organic materials. We can roughly distinguish two classes: polymers, like e.g. P3HT, and small molecules, among which are such representatives as pentacene, perylene or *para*-sexiphenyl. In this thesis we will focus on the latter.

The shape of common organic semiconductor molecules is often planar and rodlike with typically a long and a narrow symmetry axis. This spatial anisotropy causes an anisotropy of the opto-electronic properties. Using an extreme example, the absorption of the molecule diindenoperylene differs by an order of magnitude comparing the lying down and the standing upright orientation on a substrate due to the different strength and direction of optical dipole moments.[6] A similar anisotropy is also found for the charge carrier transport. In the case of *para*-sexiphenyl (6P), a molecule, which is in the focus of this thesis, a flat lying orientation is demanded for light-emitting applications (organic light emitting diodes - OLEDs). In contrast, an efficient charge carrier transport from source to drain in organic field effect transistors (OTFT) based on 6P requires upright standing molecules.[7] Importantly, not only the molecular orientation, but also factors such as the crystallinity, crystal phase purity,[8,9] and roughness,[10] hence the structure and morphology, have a crucial impact on the functionality. In organic thin films the individual molecules are bonded by relatively weak van-der-Waals forces, so that the growth process is highly sensitive to external factors like the substrate temperature. Choosing growth conditions for optimised structures would be more efficient when reaching a fundamental understanding of the growth process and when finding new ways to control the molecular self-assembly. The aim of the present thesis is to contribute to these two research topics.

We organized our work in the following way. The consecutive **chapter 2** will deal with **the growth processes and deposition of organic thin films**. We will introduce and summarize important studies, which are focusing on nanoscale processes of structure formation. Further, we discuss mean-field nucleation theory, which was originally developed for the growth of atomic systems, and has been successfully used in the last years for organic materials. This theory demonstrates how factors such as substrate temperature and growth rate influence the growth process. In the second part of this chapter we will present the method of OMBD (organic molecular beam deposition) and the experimental setup we have used to deposit the organic thin films within this thesis. An understanding of growth requires techniques, which allow us to follow the molecular self-assembly. In **chapter 3** we will present the here applied **experimental methods to study the thin film growth**. The key method is ***in situ* and real-time X-ray scattering**, which constitutes a non-invasive mechanism to probe a comparatively large area of material as demanded for good statistical averaging. The real-time capability allows us to follow the dynamic growth process. Hence, transient phenomena such as a continuously changing molecular inclination angle, film roughening or thickness dependent sticking coefficients can be investigated.

In Chapter 4 and 5 we present the results of this work. They account for the **two main aims of this thesis**:

- **Chapter 4: Enhancing the understanding of organic thin film growth**
- **Chapter 5: Exploring novel mechanisms for growth control**

In **chapter 4** we apply modern synchrotron X-ray scattering techniques to simultaneously study the in- and out-of-plane morphology evolution during the **growth of the exemplary molecule PTCDI$-\mathbf{C_8}$**, a perylene derivative. While most previous studies have restricted the analysis of nucleation and growth to the 1st monolayer (ML) only, our analysis focuses also on the processes beyond this limit to explain the interesting layer-dependent nucleation behavior of the molecule, which shows a decreasing molecular island density and a transition of island shapes. By using nucleation theory and applying models beyond the common diffusion-limited aggregation (DLA), we analyze and **quantify important growth parameters such as the critical nucleus size, the attempt frequency for surface diffusion, the nucleation energy and the diffusivity**. In particular, we find that the nucleation energy decreases by 70 meV in the 2nd ML, while the critical nucleus size and the attempt frequency for surface diffusion of 10^{19}-10^{20}s^{-1} are constant. Within

the DLA and the more complex attachment-limited aggregation models, we correlate these findings with a decrease of the diffusion barrier energy by 140 meV in the 2nd ML, which goes along with a decreased in-plane diffusivity.

In **chapter 5** we make use of the aforementioned **chemical flexibility** of organic molecules and study its potential **impact on the growth**. The well-known *para*-sexiphenyl (6P) molecule is used as a backbone for the partial substitution of hydrogen atoms by fluorine atoms. In the first part, we study the growth of symmetrically fluorinated 6P (6PF4 - substitution of two hydrogen atoms each at both termini) on anisotropic ZnO (10$\bar{1}$0) substrates. In the second part of chapter 5, we grow an asymmetric 6PF2 (substitution of two hydrogen atoms at one terminus) on isotropic silicon oxide. Importantly, these chemically tuned derivatives of 6P preserve essentially the same dimensions and functional properties as the original 6P molecule. However, fluorination changes the chemical environment and induces local dipole moments in 6PF4 and 6PF2. The interaction of the molecules with each other and with the substrate may be influenced by the chemical modification and the question arises, if this will have an effect on the growth. As follows from our results, **both chemically tuned derivatives induce a significantly smoother film growth** reducing the roughness of 4-5 ML thick films by a factor of 2.

First analyzing the growth of 6PF4, we additionally observe **enhanced crystal phase purity as compared to the growth of 6P**. The latter exhibits bimodal coexistence of the known β- and γ- crystal phases on ZnO. We further determine an increasing inclination of 6PF4 molecules in upper MLs, which can be related to a decreasing barrier for the interlayer transport (Ehrlich-Schwoebel-barrier) and supports the smoother film growth. In the second study, we analyze 6PF2 and 6P growth in the framework of nucleation theory. We determine that the apparently tiny chemical substitution of just two atoms, induces an increase of the energy barrier for surface diffusion by approximately 560 meV and a seven orders of magnitude increase in the attempt frequency. As a result, the in-plane diffusivity D of 6PF2 at the lowest of the studied temperatures T=60 °C is about 1/30 compared to that of 6P. However, at this temperature the differences in the film roughnesses of 6P and 6PF2 are most prominent. Consequently, we demonstrate that beside the in-plane diffusivity D, the step-edge diffusivity S is also influenced as a result of fluorinating 6P to 6PF2.

Therefore our results demonstrate that chemical tuning may be regarded as a new control parameter to successfully improve molecular thin film growth. The resulting smoother thin films are beneficial for potential opto-electronic applications, since they provide an enhanced lateral charge carrier transport and a better interface definition in stacked layer structures.

Finally, **chapter 6** summarizes the results discussed in the two previous chapters and highlights the main findings in a compact fashion.

2 Growth and deposition of organic thin films

2.1 Nanoscale processes during growth

The main focus of the present thesis lies on the study of nucleation and growth phenomena of functional organic molecules on silicon oxide and zinc oxide substrates. A better understanding of this phenomena is desired and the analysis of fundamental experiments requires a theoretical backing. In the following we will describe nanoscale processes occurring during the deposition of molecules on substrates from a molecular beam in vacuum conditions. Further, by applying nucleation theory we will show, how and which physical observables can be used to quantify these nanoscale processes.

Thin film growth is a very complex process, which is the reason for the rich set of experimental and theoretical work that has been published and reviewed on this topic.[11–15] However, the majority of the theoretical work describes atomic inorganic systems, such as the growth of metals on metal surfaces. Comparing such systems to the organic molecules, which are in the spotlight of this work, one can identify several significant differences.[16,17] First, organic molecules have an extended, often flexible shape and consequently more internal degrees of freedom. This includes vibrations, confirmations, e.g. twisted or planar,[18] and orientations, e.g. lying down or standing upright.[19–21] Compared to atoms further differences are the usually larger sizes of the unit cells and the nature of the binding between the molecules and the substrate, which relies on weak van-der-Waals forces in the case of organics. The weaker binding causes softer materials, which can be strained. Despite these differences, significant results and considerations concerning growth modes and mean-field nucleation theory can be transferred to organics as has been demonstrated in various publications.[22–25]

When considering growth from a thermodynamic perspective, we can distinguish three different growth-modes. Assuming thermal equilibrium, in which the lowest surface and volume energy state is adopted, these three modes are denoted as

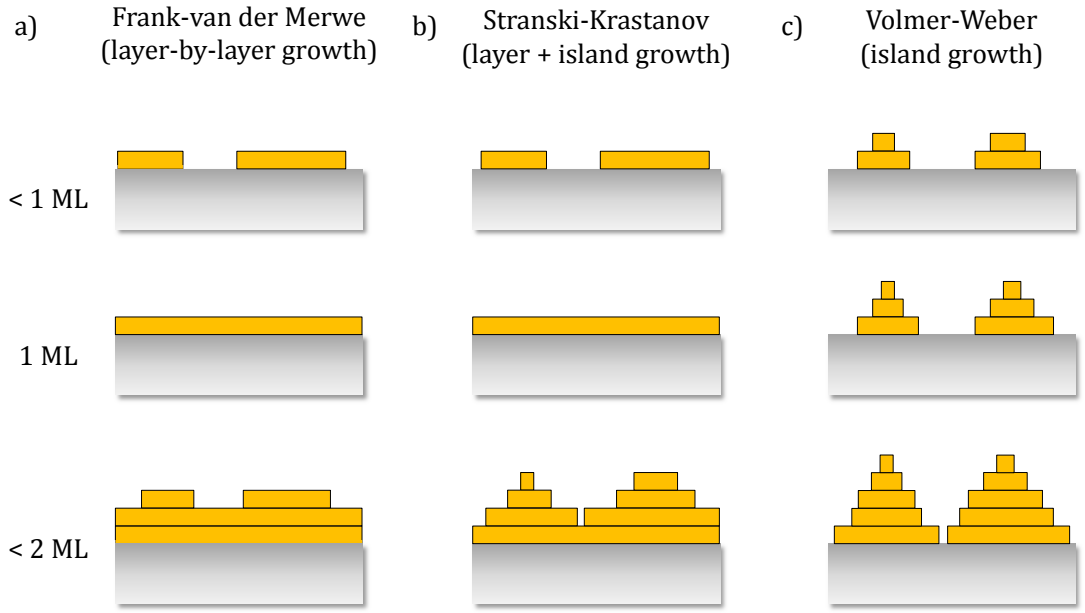

Figure 2.1: Illustration of the three different growth-modes occurring in OMBD in thermodynamic equilibrium. a) Smooth Frank-van-der-Merwe growth, which is also known as layer-by-layer (LBL) growth. b) An intermediate mode, referred to as Stranski-Krastanov. c) Rough Volmer-Weber growth with 3d "wedding cake"-like structures, also known as island growth mode.

Frank-van-der-Merwe, Stranski-Krastanov and Volmer-Weber. In Figs. 2.1 a)-c) we schematically display the differences between the modes. The Frank-van-der-Merwe mode describes the situation of perfectly smooth layer-by-layer (LBL) growth. The growth of a successive monolayer sets in at the moment when the preceding layer covers the surface completely. The opposite occurs in the Volmer-Weber mode, which is also referred to as island growth. Here, clusters of a monolayer (ML) height, which are referred to as islands, distribute on the surface and the further incoming material does not close the first monolayer, but the molecules start to nucleate on top of the islands. As a result, morphologies resembling wedding cakes can be observed. In contrast to the LBL growth, such rough, 3d growth is generally not desired for functional thin films, since a lateral charge carrier transport is significantly hampered. The third mode, which is the Stranski-Krastanov mode, is a blend of the two aforementioned modes. In the beginning one observes one or more monolayers completely covering the surface, before the growth transforms to an isolated island growth due to energetic changes such as strain relaxation at a critical thickness.

The occurrence of these three different modes is derived from free energy considerations. One takes into account the surface free energies of the substrate $\gamma_{substrate}$, the

growing thin film $\gamma_{thinfilm}$ and an interfacial surface energy between the substrate and the film $\gamma_{interface}$. The relation between these involved energies is decisive for the growth-mode. In a situation, where

$$\gamma_{substrate} \geq \gamma_{thinfilm} + \gamma_{interface}, \tag{2.1}$$

one will observe the LBL or Frank-van-der-Merwe growth-mode.[14] In the opposite case, where the free energy of the substrate is smaller than the sum of $\gamma_{thinfilm}$ and $\gamma_{interface}$, the rough Volmer-Weber growth sets in. In the intermediate Stranski-Krastanov mode, relation (2.1) holds for the case of layer-by-layer growth, before the energy relation is disturbed by different factors and island growth begins. As mentioned, such factors may be a change in molecular orientation or lattice parameters, strain or symmetry arguments.[11]

Although these three growth-modes can be observed in real systems, thin film growth is rather a non-equilibrium process. Structures, which in equilibrium conditions are not the most stable ones, can be formed if kinetically favored. A profound understanding of molecular self-assembly, thus, necessarily needs an analysis on the microscopic level comprehending kinetic arguments.

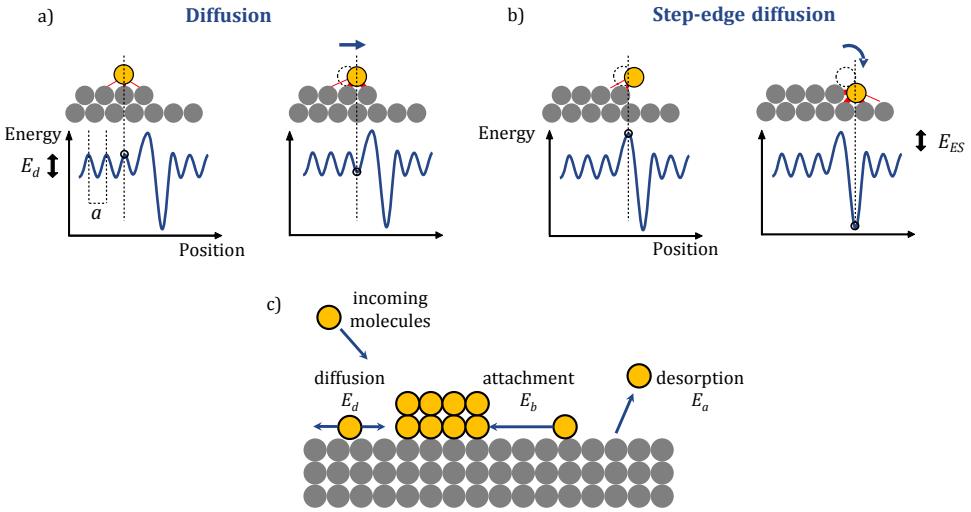

Figure 2.2: a) Scheme of the diffusion process of a single molecule on a crystalline substrate. During hopping the molecule has to overcome the energetic barrier of diffusion E_d. A hopping step equals the lattice constant a of the substrate. b) Downward transport of a molecule from the top of an edge. The molecule has to overcome an additional energy barrier, the Ehrlich-Schwoebel barrier E_{ES}. c) Visualization of selected processes and energetic barriers involved in the nucleation and growth process.

In Fig. 2.2 c) we display a selection of nanoscale processes occurring to individual molecules, which arrive from a molecular beam on a surface. A requirement for film growth is, evidently that molecules are not instantly reflected back, but adsorb or stick on the surface. Depending on the circumstances, e.g. on the substrate temperature, this must not be the case. The sticking factor is a quantity describing the probability of adsorbing the molecule. Later, in the results chapter, we will demonstrate that the sticking factor can be different on the substrate and on a monolayer of a film.

After being adsorbed, the molecules usually dissipate their kinetic energy to the lattice and adopt the temperature of the surface. The further lateral motion of the molecules on the surface is known as diffusion and can be regarded as a hopping process between different surface sites, i.e., local surface energy minima. For each hop the molecules have to overcome a diffusion barrier energy E_d, as sketched in Fig. 2.2 a). In perfect crystals the height of the energetic barriers is constant over the whole surface. However, defects, contaminations or step edges can have higher potential energy barriers. Transition state theory mathematically describes the hopping or diffusion process as:[14,26]

$$D = C \cdot a^2 \cdot \nu_0 \cdot \exp(-E_d/kT), \tag{2.2}$$

where D is the diffusivity, ν_0 is the attempt frequency, E_d the activation barrier for diffusion or the diffusion energy, a the lattice constant, C is a symmetry factor, k is the Boltzmann constant and T the substrate temperature. As follows from equation (2.2), higher temperatures increase the diffusivity of the molecule. This is beneficial for film growth, since this equally increases the diffusion length and, thus, the probability of the molecule to find a binding partner and initiate the nucleation of stable, large islands. On the other hand, higher temperatures facilitate the re-evaporation or desorption of already attached molecules. Desorption is likewise described as a thermally activated process and its rate is proportional to $\exp(-E_a/kT)$.[11] E_a is referred to as the activation energy for desorption. Further, higher temperatures may have an influence on the sticking factor in a way that less molecules get adsorbed on the surface and, instead, are being instantaneously reflected. Temperatures have thus to be optimized to enable sufficient diffusion on the one hand and low desorption/backreflection rates on the other.

When two diffusing molecules meet, they can form a cluster, a so-called dimer. The dimer can either integrate a new molecule and become a trimer or it can dissolve again. This continues until a critical island size i is reached. Islands containing at

least i+1 molecules are more likely to stay stable than to decay. The quantity of i depends on many parameters such as the material of the growing film and the substrate or even on the substrate temperature.[27,28] It is a very important quantity for the understanding of structure formation. One can infer that systems with a large i will contain a smaller amount of stable islands. This may influence the number of grain boundaries in the monolayer, which in turn affects the efficiency of charge-carrier transport.[29] For many inorganic materials, e.g. metals, critical island sizes of i=1 have been found at temperatures around room temperature.[13,30] In contrast, for organic systems usually larger i's are reported.[22,31–33] A further important quantity is the binding energy of the critical cluster E_i, which is defined as the energy needed to break an island of n molecules into n adsorbed molecules.[22]

With increasing deposition time, the number of stable islands will increase, if the molecules stick to the surface and the desorption is zero or insignificant. The nucleation of new islands continues until the separation between the islands is smaller than the diffusion length of individual molecules. Once reaching a maximum island density, the islands grow laterally. In this phase the island density remains almost constant until the edges of different islands begin to touch. The islands coalesce and their density begins to decrease until it falls to zero when a completely closed monolayer is formed. Such a three step process constituting of nucleation, lateral growth and coalescence is characteristic for a smooth layer-by-layer growth and can be identified in experiments.[34] For smooth LBL growth the prerequisite is that molecules, landing on top of existing islands, will be transported downwards. If, instead, the molecules will nucleate new islands on top of the growing first monolayer, wedding cake structures or Volmer-Weber growth will set in. The molecular downward or interlayer transport can also be regarded as a hopping process. To hop downwards from an edge the molecule has to overcome an additional energetic barrier, the Ehrlich-Schwoebel barrier E_{ES}, see Fig. 2.2 b).[35,36] The origin for this additional energy is that during the downward motion the molecule has to traverse a state with fewer binding partners than on top of the island. This state is energetically unfavored and corresponds to a higher potential energy.[37] The knowledge of E_{ES} is necessary for a better understanding of the film morphology, yet its experimental determination is very challenging and thus rather a matter of theoretical calculations.[7,34,38–40] It is important to note that during the growth, but also after finishing the deposition, some systems may undergo transformations, e.g., wetting or dewetting.[41–44] The occurrence of such processes demonstrates the kinematic component of the growth and underlines the significance of *in situ* real-time measurements for growth analysis.[45]

2.1.1 Nucleation theory based on rate equations

The above-sketched nanoscale processes of monolayer formation can be described mathematically and connected to observables accessible in experiments. The classical description relies on rate-equations, which we will summarize here, following the review by Krug.[37]

We consider two quantities, the lateral average density of individual molecules or monomers, n_1, and that of clusters containing s molecules, n_s. We assume that only monomers are mobile and, consequently, clusters grow exclusively by incorparating monomers. In such a scenario, the temporal evolution of n_s can be described as follows:

$$\frac{dn_s}{dt} = \Gamma_{s-1} - \Gamma_s, \tag{2.3}$$

where Γ_s and Γ_{s-1} are net ratios describing the creation of clusters of size s from *s-1* clusters and of *s+1* clusters from s clusters, respectively. The detailed definition of the net ratio includes the possible detachment of monomers from the cluster:

$$\Gamma_s = \sigma_s D n_1 n_s - \gamma_{s+1} n_{s+1}, \tag{2.4}$$

with γ_{s+1} being the rate of monomer detachment from an *s+1* cluster. Further, σ_s is referred to as capture number, indicating the propensity of a cluster to aggregate a monomer. In the case of complete condensation with zero or negligible desorption (important: sticking factor can be <1) the change of the monomer density n_1 with time can be described as:

$$\frac{dn_1}{dt} = GR - 2\Gamma_1 - \sum_{s\geq 2} \Gamma_s. \tag{2.5}$$

The density of monomers increases due to the growth rate *GR*, which is the number of all incoming molecules (per time and area) minus the number of molecules which are not adsorbed and instantly backreflected in case of a non-unity sticking factor. In contrast, n_1 decreases if two molecules aggregate to a dimer and also if one monomer attaches to a larger cluster. These are the two loss terms in equation (2.5).

As stated above, clusters larger than the critical island size i, thus $s \geq i$, are called islands and are regarded as stable. Accordingly, the monomer detachment from islands is zero, i.e. $\gamma_s = 0$ for $s \geq i$. The density of islands N is expressed by:

$$N = \sum_{s=i+1}^{\infty} n_s \tag{2.6}$$

and by inserting equation (2.3), we find the temporal evolution of N as:

$$\frac{dN}{dt} = \sigma_i D n_1 n_i. \tag{2.7}$$

Assuming thermal equilibrium of the unstable clusters, their net formation rate becomes Γ_s=0 ($s \leq i$-1). In accordance to[46], their density n_s can be correlated with the binding energy of a cluster E_s (for 2$\leq$ s $\leq$$i$-1):

$$n_s = (n_1)^s \exp\left(\frac{E_s}{kT}\right). \tag{2.8}$$

Consequently, equation (2.7) can be rewritten as:

$$\frac{dN}{dt} = \sigma_i D (n_1)^{i+1} \exp\left(\frac{E_i}{kT}\right). \tag{2.9}$$

By further defining an average capture number of the stable clusters $\bar{\sigma}$, the temporal evolution of the monomer density transforms to:

$$\frac{dn_1}{dt} = GR - \sigma_i D n_1 n_i - \bar{\sigma} D n_1 N. \tag{2.10}$$

Two regimes can be formulated for solving the equations (2.9) and (2.10). The first regime is the transient regime, where the capturing of monomers does not play a role. The densities of monomers and islands are then defined as:

$$n_1 \approx GR \cdot t = \Theta \cdot t \tag{2.11}$$

$$N \approx (GR \cdot t)^{i+2} = \Theta^{i+2}, \tag{2.12}$$

where Θ is known the coverage. When capturing of monomers sets in, the transient regime transforms into the steady state regime, which is characterized by a balance of the first and third term of equation (2.10). The monomer density becomes then $n_1 \approx GR/\bar{\sigma} D N$, while the island density N can be described as:

$$N \approx \eta(\Theta, i) \cdot \left(\frac{GR}{D}\right)^{\frac{i}{i+2}} \cdot \exp\left(\frac{E_i}{(i+2) \cdot kT}\right) \tag{2.13}$$

$$\Rightarrow N \approx \eta(\Theta, i) \cdot \left(\frac{GR}{\nu_0}\right)^{p} \cdot \exp\left(\frac{E_{nuc}}{kT}\right). \tag{2.14}$$

We used the definition of the diffusivity and further introduced the nucleation energy E_{nuc} and the exponent p. The factor η is a weakly varying function of the coverage and i.

In the present thesis we will use equation (2.14) to determine the critical island sizes, the nucleation energy and the diffusivity of organic molecules by performing growth experiments at various growth rates and substrate temperatures. We note that the above sketched derivation and equation (2.14) is valid for *homogenous complete condensation*, i.e. a defect-free surface and no desorption are assumed. Furthermore the probability of molecule attachment to islands is assumed to be unity, if the molecules are just close enough to the island edge. Finally, we also supposed that the kinetic energy of the incoming molecule is completely dissipated once it is adsorbed on the surface. Naturally, for some systems these assumptions may not be valid and equation (2.14) has to be revised and adjusted. We will discuss this in detail in section 4.1, when analyzing our experimental results. At this point we want to mention that the general form of equation (2.14) will remain in most other cases, such as the *initially incomplete condensation* or the *attachment limited aggregation*. We also refer to the literature for more information on other nucleation regimes than the one discussed here.[11,23,47,48]

2.2 Deposition methods of organic thin films

The deposition methods of organic thin films can in general be classified into vacuum and non-vacuum technologies. Non-vacuum methods are often based on solution-processing and are widely used for functional polymers, which are applied, e.g., in organic solar cells or field effect transistors.[49–53] A very common deposition method is spin-coating, where a drop of a solution containing the functional organic material is deposited on a flat substrate, which is then rotated to distribute the liquid over the whole surface. Instead of spinning the substrate, one can also add chemicals, which support the wetting process. Deposition out of solution is probably one of the cheapest options with a high potential to be implemented in industrial roll-to-roll or ink-jet printing methods.[4] However, good solubility of materials is a prerequisite for solution-based deposition. Further, a precise control of the deposited volume on a (sub-) monolayer level is difficult to achieve. Additionally, to follow the structure formation of spin-coated films *in situ* and in real-time, measurements on a millisecond timescale are required, which is a challenging task, although

progress is made in this direction.[54] Despite these constraints, in the literature one still can find many examples for solution processed small molecule thin films.[55–59]

Although usually requiring more effort and costs, vacuum based deposition techniques offer the advantage of keeping a clean and very well defined surface. Especially for reactive surfaces such as ZnO, high vacuum conditions are inevitable for reproducible growth studies. Contaminations, condensed water films and other impurities may strongly influence the nucleation behavior, causing potentially misleading experimental results. In the present thesis we mainly apply the vacuum based deposition method of organic molecular beam deposition (OMBD). In the following section we will briefly describe the working principle and introduce the experimental setup. Alternative vacuum-based methods, which we will not discuss in detail, are e.g. supersonic beam deposition,[32,60–63] which enables to directly control the kinetic energy of the incoming molecules, and pulsed laser deposition (PLD), where a focused laser sublimes the target and a beam of growing material is generated.[64–66]

Although operating in vacuum, an accurate substrate cleaning prior to the deposition is essential. In the second part of this chapter we will describe the procedures used to prepare clean silicon oxide and zinc oxide surfaces for the conducted growth studies.

2.2.1 Organic Molecular Beam Deposition (OMBD) and deposition setup

The deposition of the molecular thin films for the experiments in this thesis was realized in a home-built portable ultrahigh vacuum (UHV) chamber, see Fig. 2.3. The chamber consists of three parts: the bottom part with the sample holder, the middle part, which is the Beryllium window, and the top part containing optical viewports and the effusion cells for the molecules. Due to its dimensions and the comparatively light weight of about 25 kg, it is possible to mount the chamber not only at the diffractometer of the home lab but also at different synchrotron beamlines.

All of the molecules used in the framework of the present thesis exist in form of a powder at room temperature and at ambient conditions. In OMBD the molecules are deposited on the substrate from a gaseous phase. The molecule powder is loaded into a crucible, which is resistively heated by a tungsten wire through an electric feedthrough located in the top part of the deposition chamber. Heating the crucible up to the evaporation point of the molecules starts the deposition process. Due to

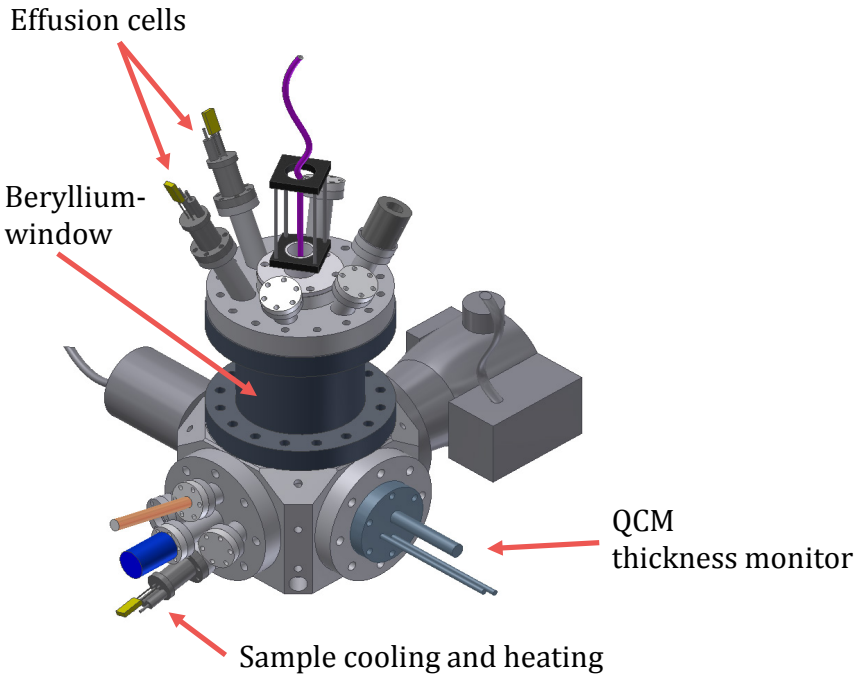

Figure 2.3: Sketch of the portable UHV chamber, in which the deposition of the organic thin films has been performed.

the vacuum conditions the molecules fly in a cone shaped beam towards the sample, where they nucleate and form a thin film layer. The flux of the molecules can be adjusted by decreasing or increasing the temperature of the crucible. The amount of deposited molecules per time is monitored by a quartz crystal micro-balance (QCM), which is placed close to the sample. When molecules hit the QCM, the mass of the oscillating crystal changes and so does the oscillation frequency. From this, the thickness of the deposited film can be calculated. The molecular flux or the growth rate is an important parameter in OMBD and has a strong influence on the nucleation process of molecular islands. The operating temperatures for the evaporation of the molecules used in this thesis were in the range of 150-300 °C.

The substrate temperature is an important parameter to influence the thin film growth. In the UHV chamber the substrate temperature is controlled by using a commercial halogen lamp which is inside of a molybdenum cube, providing good and homogeneous heat conductivity. The lamp is contacted through an electric feedthrough. The dissipated electrical power of the lamp, and consequently also the substrate temperature, is adjusted by applying a voltage on the lamp. At maximum voltage (12 V), substrate temperatures of about 650 °C can be reached. To ensure efficient heat transport, the sample is connected with the holder by a heat-conducting adhesive silver paste, which additionally fixes the sample after drying.

Above the sample a shutter is mounted, which allows us to block the sample from the molecular beam. The shutter is connected to an electrical motor, allowing a precise lateral positioning. Consequently, stripes with different film thicknesses can be deposited on the same substrate during a single growth run.

One of the largest advantages of the presented deposition chamber is that it allows us to monitor X-ray scattering *in situ* and in real-time. X-rays enter and exit the chamber through the Beryllium window, which is a highly toxic material and has to be handled with extreme care, but due to its low electron density it is transparent for X-rays.

2.2.2 Preparation of substrates

This thesis deals with the understanding and controlling the growth of ultra-thin organic semiconductor films on inorganic surfaces. As we will show in the results section, the coverage of the deposited material is often on the order of a few monolayer (ML) or even on the sub-ML scale. The resulting thickness of the layers reaches often only several 10 Å. At such scales, surface contaminations and defects like tiny scratches, solvent residuals, dust particles may influence the nucleation, diffusion and growth of molecular films. Thus, a clean and well-defined surface becomes a prerequisite for reproducible experiments and well-grounded conclusions. In the following two subsections we will present the methods, which we have applied to prepare such surfaces on silicon oxide and ZnO substrates.

2.2.2.1 Preparation of silicon oxide substrates

In the present thesis silicon wafers with a thin native oxide layer were used as substrates for the deposition of organic thin films. The wafers were cut using a diamond cutter and then cleaved into ca. 10 x 10 mm^2 pieces. Great care has been taken to not scratch the surface with the tiny silicon pieces resulting from the cleaving.

Prior to the deposition of the organic film, the substrates were cleaned in a standardized cleaning process consisting of three steps. In the first step the substrates were placed in a test tube containing acetone. After 10 min cleaning in an ultrasonic bath the test tube was rinsed out. Likewise followed a 10 min ultrasonic cleaning in 2-propanol and in distilled water. The samples were then dried using a gentle flow of nitrogen gas. The last cleaning step is carried out at vacuum conditions in the

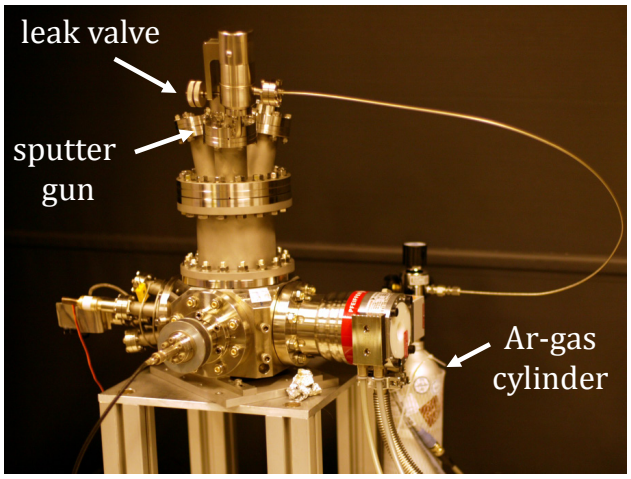

Figure 2.4: Photograph of the setup of the argon atom sputtering gun on top of the deposition chamber. This setup was installed in the framework of the present thesis. The keyparts of the setup are marked with arrows: argon gas cylinder, the ultra-precise valve to regulate the flow of the argon ions and the sputtergun.

deposition chamber. The silicon substrates are heated to temperatures >400 °C for about 1 h so that potential contaminations from the organic cleaning solvents can evaporate. If possible, the cleanliness of the substrate was finally checked by X-ray reflectivity measurements prior to the deposition process.

2.2.2.2 Preparation of ZnO substrates

ZnO (10$\bar{1}$0) single crystals were obtained from *Crystec GmbH*. The samples were 10 x 10 mm^2 in size and were polished by the manufacturer either from both sides or only from the topside, where the film has been deposited onto.

The ZnO (10$\bar{1}$0) surface is non-polar and consists of parallel rows of Zn and O atoms. An effective preparation and cleaning mechanism with reproducible results was proposed by Goetzen and Witte.[67] It was applied in a slightly modified form for this thesis and consists of two steps.

The aim of the first step is to mechanically clean the sample from any contaminations. This is achieved by argon sputtering. In the framework of this thesis, a portable sputter setup (*Specs IQE 11*) was assembled and mounted on the deposition chamber, see Fig. 2.4. The setup consists basically of an Argon gas cylinder, the sputtergun, a precise valve to control the flow of the Argon ions and a control unit to adjust the kinetic energy of the argon ions. For the ZnO cleaning, sputtering proceeds

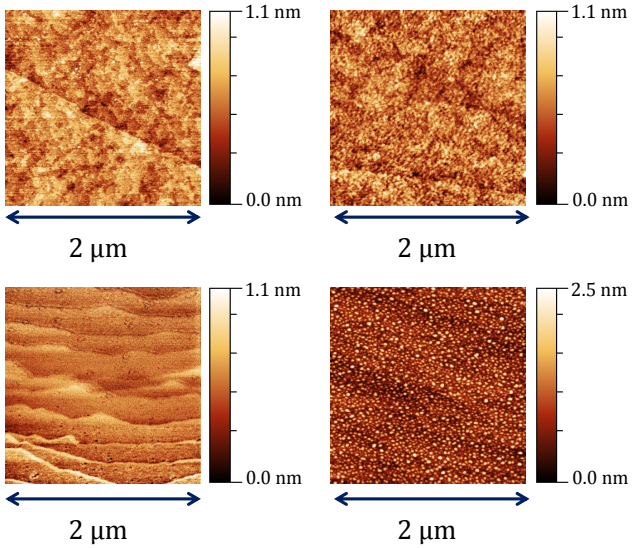

Figure 2.5: AFM images of a ZnO (10$\bar{1}$0) surface: a) as-received, b) after 1 h sputtering with Ar^+ ions, c) after 1 h annealing at 950 °C under ambient air and d) a cleaned sample after 6 days of storage at ambient air. The images visualize how a surface with atomically flat ZnO terraces is achieved after applying sputtering and annealing and how this smooth surface ordering is lost if stored for a couple of days in air.

for 1 h at an kinetic energy of 1 keV at high vacuum conditions below $1 \cdot 10^{-7}$ mbar.

The bombardment with Ar^+ ions leads to a strong increase in the roughness of the substrate as demonstrated in Fig. 2.5 b). To achieve well-defined and atomically flat surfaces, the substrate is heated in air in a furnace for 1 h at a temperature of 950 °C, which constitutes the second cleaning step. During heating, smooth terraces of single ZnO layers form, as can be seen in Fig. 2.5 c). The annealing of the substrates in air conditions is important, since it prevents an oxygen depletion. Likewise, the storage of freshly cleaned ZnO substrates in (ultra) high vacuum is critical, since otherwise a degradation and roughening of the surface sets in, as exemplary shown in Fig. 2.5.

3 Experimental methods to study organic thin film growth

Understanding and tuning growth processes requires tools to follow the kinetics of molecular self-assembly. A large amount of experimental techniques is nowadays available, which have the demanded resolution in space and time and offer *in situ* capabilities. An example are techniques based on electron diffraction. Reflection high energy electron diffraction (RHEED) is an established method to analyze the growth mode of thin films and has also been applied to organic growth.[68–71] Low-energy electron microscopy (LEEM) and low-energy electron diffraction (LEED) provide an interesting combination of microscopy and structure analysis and are also widely-used to study the nucleation and growth of organic molecules and to derive important quantities like the critical nucleus size.[72–75]

In this thesis, X-ray scattering constitutes the main characterization technique. One of the advantages of X-ray scattering is the comparatively large surface area which is analyzed. This increases the statistical averaging. Importantly, X-ray scattering is non-invasive and allows for a wide sample environment including liquid, gas and vacuum conditions. Thus, over the last years modern X-ray scattering experiments have proven to be a powerful tool for studying organic thin film growth *in situ* and in real-time. In particular, specular X-ray reflectivity (XRR) has been successfully used to study the evolution of the out-of-plane structure of a variety of different of organic systems.[19,76–80] The growth-mode, a quantification of surface roughness and changes of the molecular orientation during the self-assembly can be extracted from XRR measurements. Additionally, grazing-incidence small-angle X-ray scattering (GISAXS), which probes the diffusively scattered fraction of the incoming X-rays, can be used to examine the time evolution of the in-plane morphology, e.g., the island densities.[34,81–84] Modern synchrotron facilities offer the possibility to combine XRR and GISAXS to gain complementary information. We will use this for our study presented in section 4.1.

A complementary characterization technique used throughout this thesis is atomic force microscopy (AFM). AFM usually suffers from tip shadowing effects, which restrains its use for *in situ* growth studies. However it provides important information on the shape of structures, which is usually challenging to extract from X-ray scattering experiments. AFM is also an established method to study island densities. Furthermore, though not in the scope of this work, information on electronic and mechanical properties of thin films can be yielded from AFM. In the following we will introduce the working principles of the main characterization techniques of this thesis.

3.1 Atomic Force Microscopy (AFM)

In the present thesis an atomic force microscope (AFM) was used to resolve the morphology of the deposited organic thin films. In contrast to X-ray techniques, AFM allows one to study the films in real-space and gain direct information about the densities of molecular islands, their size and shape. All AFM images shown in this thesis were acquired on a *Bruker MultiMode 8*, see Fig. 3.1 a), in the so called *ScanAsyst PeakForce Tapping* imaging mode. In the following, we briefly outline the working principle of the microscope.

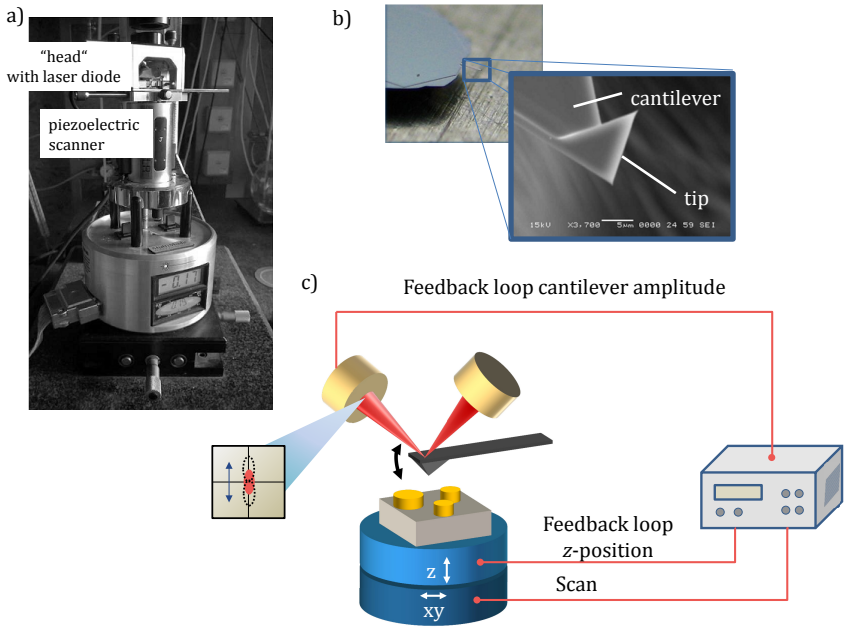

Figure 3.1: a) Photograph of the *Bruker MultiMode 8* AFM device used for image acquisition. b) Exemplary image of an AFM cantilever and tip (captured by M. Gensler). c) Sketch of the AFM working principle.

The AFM was introduced in 1986 by Binnig, Quate and Gerber.[85] To acquire an image, a small tip with a typical radius of 5-10 nm is brought in close proximity to the surface and scans a defined area of the sample (usually not larger than 100 × 100 µm^2), which is the reason for the AFM being also referred to as scanning force microscope (SFM). The provided AFM resolution exceeds by far values achieved with conventional optical microscopes and reaches <1 nm in the vertical and about 10 nm in the lateral direction. The tip is mounted on a cantilever as shown exemplary in Fig. 3.1 b) constituting a spring-like construction with a spring constant k. Interaction forces like Coulomb and van der Waals forces between the tip and the sample will deflect the cantilever in the vertical and eventually in the horizontal direction when moved over the scan area. Each deflection causes a displacement of the laser beam reflection from the upper side of the cantilever and is detected on a photodiode, which typically consists of four parts, see Fig. 3.1 c). By comparing the measured light intensities at each of the four parts of the photodiode, the deflection signal can be calculated via:

$$Deflectionsignal = (A + B) - (C + D), \tag{3.1}$$

with A, B, C and D being the light intensities at each single part of the photodiode. A change of the laser deflection angle is amplified due to the comparatively large distance between the cantilever and the diode. In consequence even deflections in the sub-Angstrom range can be detected.

Classically, the AFM can be used in three different imaging modes, which are known as contact-mode, non-contact-mode and intermittent-contact-mode. In the contact-mode the tip is in mechanical contact with the sample and literally scans over the surface. The atomic (or molecular) orbitals of the tip and sample overlap, resulting in a repulsive force on the cantilever, see Fig. 3.2a) and d). One operates either in a constant height or in a constant force mode. In the first mode, the height of the cantilever is kept constant and the changes of the tip deflection can be directly converted into changes of the surface heights. In contrast, in the constant force mode, the force between tip and sample is kept constant. This is realized by moving the cantilever holder up and down in accordance to higher or lower regions of the surface. From those movements the three-dimensional topography of the sample surface can be restored. The drawback of the contact-mode, is an increased risk of damaging both sample and tip, which especially counts for very soft samples. An interesting option of the contact-mode, though usually requiring specialized tips, is the measurement of frictional forces by detecting the tip deflection in the horizontal

directions (lateral force microscopy - LFM). These measurements may be used to map differently oriented molecular crystals, as demonstrated e.g. in the studies by Rabe and Koch *et al.* and Kalihari *et al.*.[86,87] Different frictional forces are visualized in the LFM image as a colour contrast and domains can thus be assigned to their respective crystal orientation on a nm-scale.

In the non-contact-mode, first introduced in 1987,[88] the tip and the sample are - as the name reveals - not in contact, see Fig.3.2c) . Due to the larger separation between tip and sample the forces that cause the cantilever deflection, are of different nature (mainly van der Waals forces) and much weaker. To start the measurement the cantilever is stimulated at its eigenfrequency f_0 by a piezoelectric drive. The interaction forces between sample and tip induce a change in the oscillation frequency of the cantilever, which can be expressed in form of an additional frequency term df:

$$f = f_0 + df = f_0\sqrt{1 - \frac{F'(z)}{k}}. \tag{3.2}$$

In the above equation, k is the spring constant of the cantilever, $F'(z)$ is the force gradient induced by the sample and f is the new oscillation frequency. At larger distances the interaction is attractive and, thus, the oscillation frequency f of the cantilever reduces. However at smaller tip-sample distances, e.g. due to elevations of the surface, the interaction force becomes more repulsive, see Fig. 3.2, and the oscillation frequency increases. Using a feedback loop, a constant oscillation frequency can be maintained by adjusting the tip-sample distance at each xy-point. Consequently, a reconstruction of the surface morphology can be realized. A disadvantage of the non-contact mode is that at ambient conditions, many surfaces are covered with a thin liquid film e.g. by condensed water. This film distorts the measurement of the weak long-range forces and the image quality is decreased.

Avoiding such effects on the measurement is possible by using the intermittent-contact-mode or tapping-mode, see Fig. 3.2b). The operating principle is similar to the non-contact mode with elements of the contact-mode. Far from the sample surface the cantilever is stimulated to oscillate close to its eigenfrequency and high amplitude. The oscillating tip is approached to the surface until the tip gently "‘taps"’ the surface. Such a tip-surface contact results in energy losses of the oscillation and, thus, reduces the oscillation amplitude. A feedback mechanism regulates then the tip-sample separation in z-direction, so that the amplitude is kept constant throughout the scan. From the motions of the z-piezo the sample morphology can be restored such as in the contact-mode. In contrast to the contact-mode the interaction

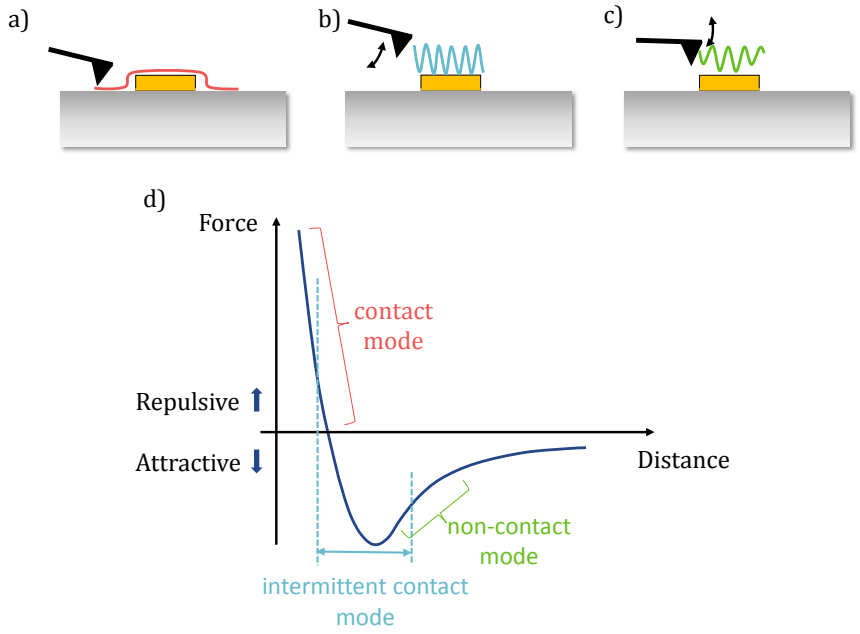

Figure 3.2: Three different AFM operation modes: a) contact mode, b) intermittent contact mode, and c) non-contact mode. d) The curve shows schematically the character of the force-distance-interaction of sample and tip. At larger distances the force is attractive, however the closer sample and tip get the more repulsive becomes the interaction force.

of tip and sample is short-termed and soft, so that sample damages can be avoided. Further the tip motion occurs solely in the vertical direction and lateral shear forces are minimized.

While the above outlined modes are nowadays very common, throughout this thesis a comparatively novel, so called *PeakForce tapping* mode was used to acquire the images. In this regime, the sample oscillates at a frequency of typically 2 kHz. The amplitude of the oscillation is high and at the lower reversal point the tip touches the surface for a short period of time. A force versus separation curve is recorded for each single tap and the maximum interaction force, the peak force, is held constant during the scan process by using feedback loops. The peak forces are usually very small, in the range of nano- or even pico-Newtons, and hence do not harm the surface. An important difference to the intermittent-contact-mode is that in PeakForce tapping the instrument parameter set-point is directly proportional to the maximum tapping force as a physical quantity. Applying an elastic fit to the force versus separation curves, it is then even possible to map the elastic modulus of a sample.[89] In comparison in the intermittent-contact-mode there is not such a direct coupling of parameters and physical quantities, since the tip-sample interactions become very complex.[90,91]

The here used *MultiMode 8* AFM device enables to combine the PeakForce tapping mode with *ScanAssyst*. In this combination the feedback loop automatically optimizes the parameters: set-point, feedback gain and z-limit (limit for the vertical movement of the cantilever holder). The permanent readjustments of the acquisition parameters increases the stability of the measurement. The feedback loop reacts instantly on e.g. thermal fluctuations and enables measurements under constant conditions.

The centerpiece of each AFM are the cantilevers and tips, which substantially determine the resolution of the image. They are available in different sizes and forms and are usually made from silicon or silicon nitride. In most cases, the radius of the tips varies from 5-15 nm, however there are also tips with a radius of only 1 nm and of up to 80 nm available. Additionally the cantilevers differ in their spring constant. For this thesis silicon cantilevers and tips from *Olympus* with a nominal spring constant of 2 and 42 N/m and a tip radius of about 10 nm were used. While well suited for many applications, in this thesis we encountered problems while acquiring AFM images of some organic thin film samples. It turned out that some molecules tend to easily adhere on the as-received tips, which was especially the case for fluorinated derivatives of *para*-sexiphenyl (6P) such as 6PF2. Consequently a serious decrease of the image quality was observed. A strategy which was developed to greatly minimize molecule-tip interaction is described in sec. 5.4 for the example of 6PF2 films.

3.2 X-ray scattering techniques

3.2.1 X-ray reflectivity (XRR) for the analysis of the out-of-plane morphology

XRR is a well-established technique for the characterization of surfaces and thin films. During the measurement the intensity of X-rays reflected from a sample is measured as a function of the angle of incidence α_i. The scattering geometry is sketched in Fig. 3.3, showing incoming X-rays with a wavevector $\vec{k_i}$ being elastically reflected at a surface. The resulting outgoing X-rays have a wavevector $\vec{k_f}$ and are acquired by a detector. The angle of incidence is thus equal to the angle of exit, so that the measurement is analogous to the $\theta/2\theta$ Bragg-Brentano configuration, yet in XRR the angles are usually smaller. Since the scattering is elastic, $\vec{k_i}$ and $\vec{k_f}$

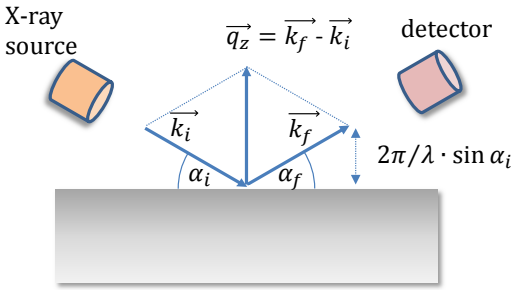

Figure 3.3: Sketch of the scattering geometry of an XRR measurement. X-rays with the wavelength λ and the wavevector k_i impinge the sample at an angle of α_i and get symmetrically reflected. The transfered momentum is along the surface normal with the transfer vector q_z.

have the same length, which equals $2\pi/\lambda$. Here, λ is the wavelength of the probing X-rays. Physically the scattering process constitutes a transfer of momentum, with the corresponding momentum transfer vector $\vec{q_z} = \vec{k_f} - \vec{k_i}$ pointing along the surface normal. This is displayed in Fig. 3.3, from which we can now derive the magnitude of the momentum transfer vector as $q_z = |\vec{q_z}| = 4\pi/\lambda \cdot \sin(\alpha_i)$. On the basis of this relation, in the literature, XRR curves are commonly plotted as a function of q_z instead of the angle of incidence (such representation is furthermore independent of the chosen λ). In the following and throughout the thesis we will stick to this convention.

XRR can be used to characterize the out-of-plane crystallinity. However, the field of application is not restricted to well-ordered structures. The technique can also be applied to amorphous materials in order to unravel properties like electron densities, film thicknesses and roughnesses in the range of few Ångströms as we have done it in section A.1. In the following we will use simulated XRR curves of modeled systems to discuss how to infere the aforementioned material properties.

Determination of the electron density

The interaction of X-rays with thin films is commonly described by the dimensionless quantity known as the refractive index n. This is physically the analogous of the refractive index as known from optics. In accordance to ref. [92], for X-rays n can be described as:

$$n = 1 - \delta + i\beta. \tag{3.3}$$

Here δ accounts for the X-ray dispersion, while β describes the absorption. Both are correlated with the material properties of electron density ρ_{el} and the absorption coefficient μ as well as the wavelength λ of the incoming X-rays:

$$\delta = \frac{\lambda^2}{2\pi} r_0 \rho_{el}, \tag{3.4}$$

$$\beta = \frac{\lambda}{4\pi} \mu. \tag{3.5}$$

The constant r_0 denotes the classical radius of an electron. Typically δ is in the range of 10^{-5}-10^{-6}, while the absorption of X-rays is very low and β varies between 10^{-6}-10^{-9}. In accordance with Snell's law, the refractive index is related with the angle of the incidence α_i and the refraction angle α_r:

$$\cos(\alpha_i) = n \cos(\alpha_r). \tag{3.6}$$

In contrast to conventional light, X-rays have a refractive index of n <1. As a consequence, there is a solution of equation (3.6) for the case of α_r=0, which is the regime of total reflection. All incoming X-rays will be completely reflected. This happens for incidence angles below or equal to a critical angle α_c, whose value can be determined by:

$$\cos(\alpha_c) = n = 1 - \delta + i\beta. \tag{3.7}$$

By neglecting absorption and using a Taylor expansion for the cosine term, we find the dependency of the critical angle on the electron density:

$$\alpha_c = \sqrt{2\delta} = \lambda \sqrt{\frac{r_0 \rho_{el}}{\pi}}. \tag{3.8}$$

In the XRR curves the regime of total reflection can be associated to the plateau of a constant reflectivity as observed at small incidence angles / low q_z values. The critical angle corresponds to the edge of this plateau. This is displayed in the example curve of a modeled perfectly smooth substrate in Fig. 3.4 a). As can be observed, at $q_z > q_c$ the reflectivity drastically decreases by several orders of magnitude. For these idealized conditions, the dependency of the reflectivity on q_z can be described by Fresnel equations showing that the decline is proportional to q_z^{-4}, which is also referred to as the Porod slope.[93,94]

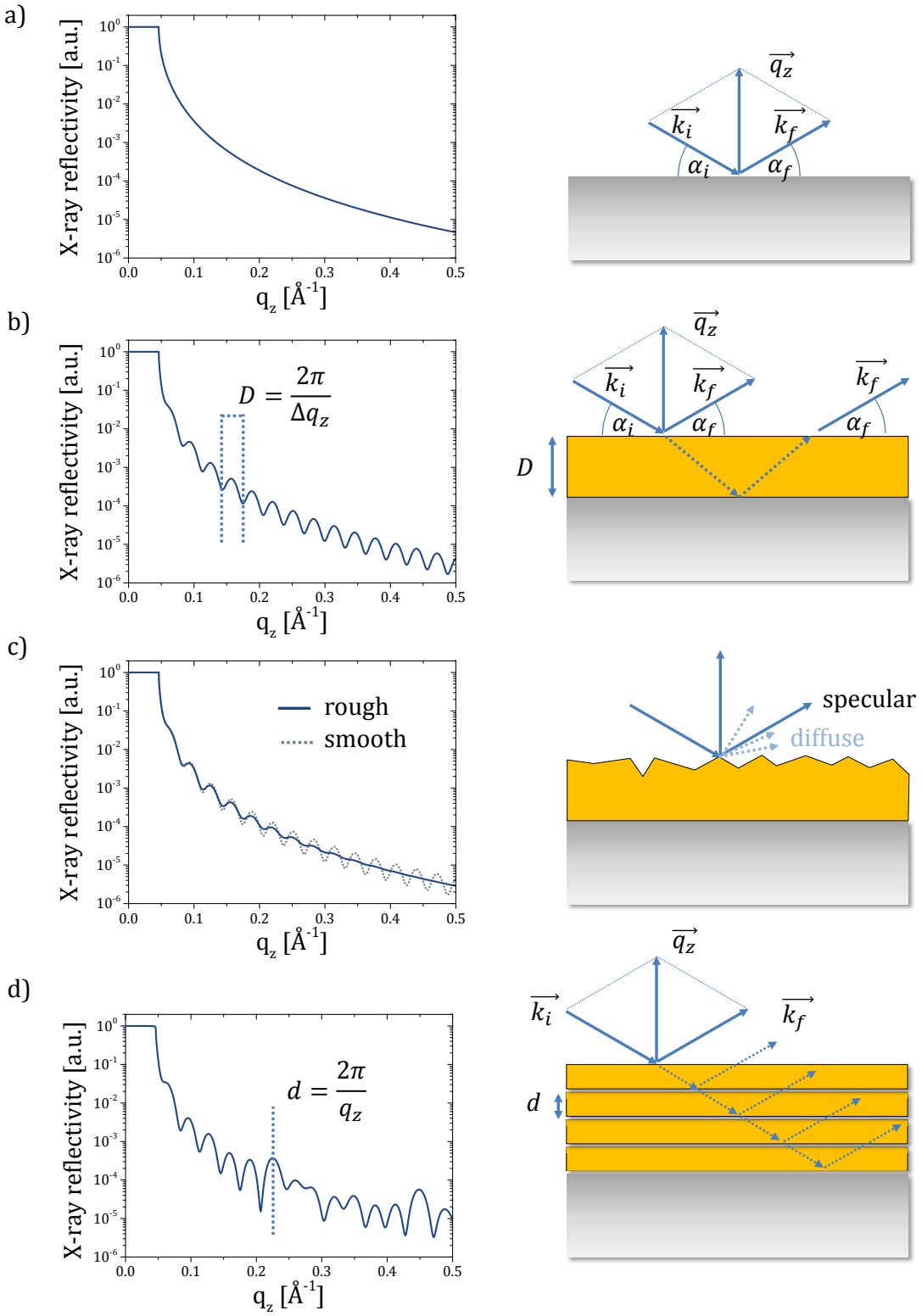

Figure 3.4: Simulated XRR curves and the corresponding models: a) smooth substrate layer, b) smooth thin film grown on smooth substrate, c) smooth thin film grown on smooth substrate, d) smooth multilayer structure grown on substrate.

Determination of the layer thickness

From XRR the thickness of thin films can be determined. We demonstrate this exemplary for a perfectly smooth thin film of thickness D grown on a perfectly smooth substrate. Importantly, thin film and substrate are different materials, i.e. their electron densities are not equal. The corresponding simulated curve for an XRR measurement of such a model system is shown in in Fig. 3.4 b). Similar to XRR on a bare substrate, we observe a decreasing intensity of the reflectivity, yet in this case the curve is periodically oscillating. The origin of these oscillations, which are known as Kiessig fringes,[95], are constructive and destructive interferences of X-rays reflected from two different interfaces: vacuum - thin film and thin film - substrate. In other words, there is an angular-dependent phase shift between these two reflections causing oscillations of the reflected intensity. The interference is constructive if the phase difference is a multiple of the X-ray wavelength. The distance between two minima is inversely proportional to the film thickness $\Delta q_{kiessig} = 2\pi/D$. It is noteworthy that the difference of the electron densities of both materials will also influence the shape of the XRR curve. A larger electron density difference between vacuum and film as well as between film and substrate will result in more pronounced oscillations.

Analysis of the film roughness

Leaving the idealized examples of perfectly smooth surface for a moment, we now discuss how roughness will affect the intensity of the reflectivity. The rougher surface will increase the absorption and therefore decrease the reflectivity. For optical wavelengths this effect is used for solar cells, where silicon wafers are texturized achieving an increased light harvesting and a decreasing of the reflectivity.[96] An additional, minor, effect reducing the reflected intensity, is that at an uneven surface, parts of the incoming X-rays will be scattered diffusively. Compared to a smooth surface, the XRR intensity of a rough sample will thus diminish and the Kiessig fringes will smear out or vanish completely as displayed in the sketch of Fig. 3.4 c).

Determination of the out-of-plane crystallinity

One of the most important fields of application of XRR is probing the out-of-plane crystallinity of thin films. Crystals are periodically ordered structures in space, similar to the exemplary multilayer structure shown in Fig. 3.4 d). For simplicity,

we again assume a perfectly smooth system, where each layer has a thickness d and an electron density ρ_{el}. In the aforementioned situation of a homogenous thin film of thickness D, the impinging X-rays had two surfaces to be reflected at. Here the situation is similar, yet the number of interfaces is higher. If the individual layer thickness d is the distance between lattice planes, the well-known Bragg's law describes the condition for the occurrence of constructive interference of the reflections at the interfaces:

$$m\lambda = 2d\sin(\alpha_i), \tag{3.9}$$

with m being an integer. The equation tells us that each time the phase difference of the reflected beams is equal to a multiple of the X-ray wavelength, constructive interference will occur and a so-called Bragg reflection will appear at the corresponding angle. An equivalent condition is the Laue-condition:

$$\vec{G} = \vec{k_i} - \vec{k_f}, \tag{3.10}$$

with $\vec{k_i}$, $\vec{k_f}$ being the wave vectors of the incoming and outgoing wave (in analogy to Fig. 3.3) and $\vec{G}$ being the reciprocal lattice vector defined as:

$$\vec{G} = h \cdot \vec{a^*} + k \cdot \vec{b^*} + l \cdot \vec{c^*}, \tag{3.11}$$

with (h,k,l) being integers known as the *Miller indices* used to label the crystal lattices. The length of $\vec{G}$ equals $2\pi/d$ on the one hand and for elastic scattering it equals $4\pi/\lambda \cdot \sin(\alpha_i)$. Consequently, in a reflectivity curve as a function of q_z the Bragg reflection will appear at $q_z = 2\pi/d$. This is shown in the exemplary curve in Fig. 3.4 d). Next to the Bragg reflection, we observe additional oscillations. These are referred to as *Laue oscillations*. The number of the oscillations corresponds to the number of layers scattering coherently. Thus, the pure observation of pronounced Laue oscillations indicates a highly ordered structure, i.e. high crystallinity. The distance between the minima of Laue oscillations is inversely proportional to the thickness of the coherently ordered domain $\Delta q_{Laue} = 2\pi/D_{domain}$. In single crystalline materials D_{domain} will correspond to the total film thickness D as obtained from the Kiessig oscillations. The important difference of Laue and Kiessig oscillations is that the first is sensitive only to the coherently ordered film thickness, while the latter depends on the total thickness and will as well occur for amorphous materials.

3.2.1.1 Footprint correction

At this point we want to mention an important detail for XRR measurements. At low angles of incidence, i.e. at low q_z values, the projection of the width of the X-ray beam d may cover an area which is larger than the lateral size of the sample. Consequently, only a fraction of the incoming photons will be reflected by the sample, as sketched in Fig. 3.5. However from a certain q_z value on, the so-called footprint will be equal to the sample dimensions and the photons will be reflected exclusively from the sample surface. A so-called footprint correction needs to be applied to account for the discontinuity in the number of photons reflected from the sample. The correction depends on the geometry of the beam and the sample, but assuming both as rectangular the corrected intensity reads:

$$I_{corrected} = \frac{d}{L} \cdot \frac{I_{measured}}{\sin(\alpha_i)}, \tag{3.12}$$

where d is the width of the incoming beam and L the sample width. From eq. (3.12) we calculate the largest angle of incidence for which the correction has to be performed as $\alpha_i \leq \arcsin(\frac{d}{L})$.

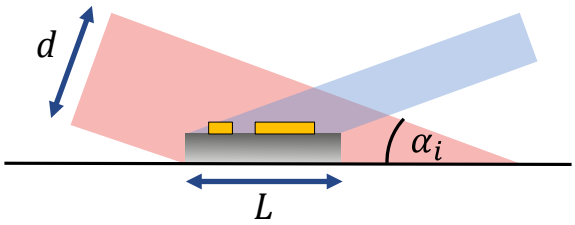

Figure 3.5: Illustration of the necessity of a footprint correction for q_z values, where the projection of the width d of the incoming X-ray beam (reddish) onto the sample plane is larger than the sample size L. In such a case only a fraction of the incoming photons can be reflected from the sample (blueish), while at larger angles, photons will be reflected exclusively from the sample surface.

3.2.2 Parratt formalism for modeling XRR data

All simulations of the XRR curves of the modeled systems shown in Figs. 3.4 a)-d) have been executed with the software *Parratt32*. Within this thesis, the same software has also been used to fit real XRR data as acquired from experiments. The *Parratt32* algorithm is based on the so-called Parratt formalism,[97] which we want to briefly summarize.

The formalism constitutes a recursive algorithm and is based on dynamical theory, i.e. it takes into account multiple scattering events. As a starting point one considers a general system with many interfaces similar to the one shown in Fig. 3.4 d), but as an additional feature each layer j can have its unique refractive index n_j. Conventionally j=1 is assigned with the medium the X-rays are incidenting from (i.e. commonly air or vacuum), j=2 is the topmost layer of the sample and $j+1$ corresponds to the substrate. The impinging beam can be either transmitted or reflected at each interface of the multilayer system. Hence for each single layer a ratio X_j of the reflected (R_j) and transmitted amplitude (T_j) of the wave can be formulated. This ratio can be described by:

$$X_j = \frac{R_j}{T_j} = e^{-2ik_{z,j}z_j} \frac{r_{j,j+1} + X_{j+1}e^{2ik_{z,j+1}z_j}}{1 + r_{j,j+1}X_{j+1}e^{2ik_{z,j+1}z_j}}. \tag{3.13}$$

The coefficient $r_{j,j+1}$ is known as Fresnel's law:

$$r_{j,j+1} = \frac{k_{z,j} - k_{z,j+1}}{k_{z,j} + k_{z,j+1}}. \tag{3.14}$$

The initial values at the beginning of the iteration process are R_{j+1}=0 and T_1=1 describing a unity amplitude of the incoming wave and no reflection from inside the substrate.

3.2.3 Temporal evolution of the out-of-plane morphology studied by XRR growth oscillations

A powerful method, based on XRR, to study the temporal evolution of the out-of-plane morphology of a growing thin film is monitoring and analyzing the so-called growth oscillations. These constitute periodic modulations of the reflected X-ray intensity of a growing thin film when measured at a fixed q_z position, which is non-zero and not the Bragg value of the thin film structure. In Fig. 3.6 a) we sketch the origin of the oscillations. The incoming X-rays are reflected from each growing monolayer and of the substrate surface. These individual reflections alternatingly interfere constructively or destructively. As a result one observes oscillations of the total reflected intensity of the whole system as a function of the deposition time.

Exemplary growth oscillations, as shown in Fig. 3.6 b), contain information on the out-of-plane structure and the crystalline layering. Quantities such as the monolayer thicknesses and coverages, and consequently the film roughness can be excerpted. This permits us to follow and understand changes in the film growth-mode.

A quantitative analysis requires, however, an underlying model for the evolution of the individual layer coverages in connection with the observed intensity oscillations.

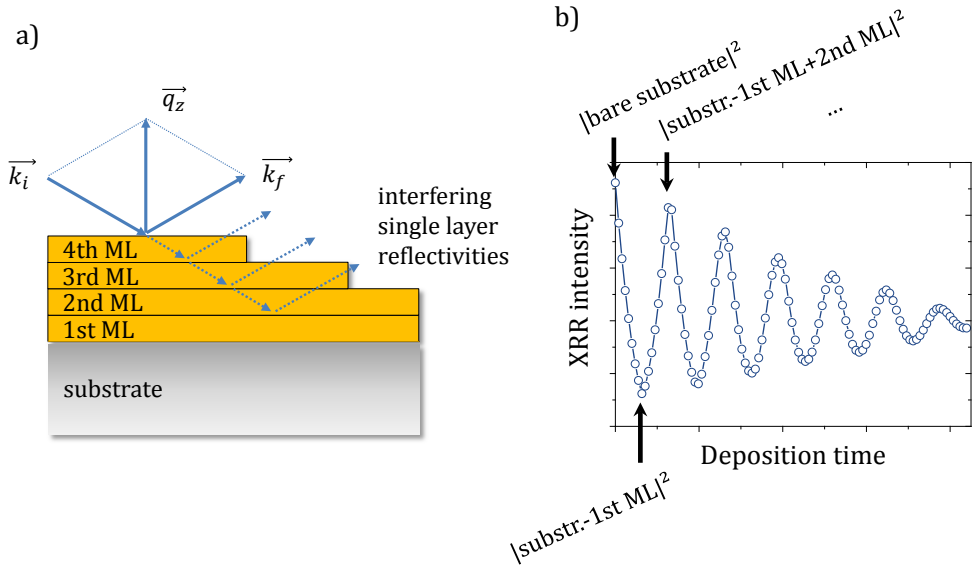

Figure 3.6: a) Schematic sketch on the origin of growth oscillations. In an experiment one measures the specular reflected beam intensity of a growing thin film at a fixed q_z position, obeying $0 < q_z < q_{Bragg}$. Constructive and destructive interference between the reflections originating from the individual monolayers and of the substrate result in oscillations of the reflected beam intensity with film thickness. The period of the oscillations depends on the chosen q_z. b) Example of growth oscillations recorded at the anti-Bragg point, where $q_z = q_{anti-Bragg} = 1/2 \cdot q_{Bragg}$. The oscillation period is 2 ML, i.e. each maximum/minimum of the curve corresponds to a closed ML.

In literature, growth oscillations are widely applied to study growth phenomena.[63,77,80,83,98–104] In the present thesis, this method was one of the key experiments. In the following, we will give a mathematical description of the oscillating XRR intensity and introduce the rate-equation model, which has been applied here to fit the growth oscillations.

3.2.3.1 On the origin of growth oscillations

The total intensity of the X-ray reflection can be described within the kinematic approximation, which is based on the Born approximation. The approximation neglects multiple scattering, i.e. no X-ray photon is scattered more than once. This holds true in a regime far from the critical angle, so $q_z \gg q_c$. The total intensity of

the scattered X-ray beams can be regarded as the Fourier transform of the electron density of the sample[105]:

$$I_q = \left| \int \rho_{el}(\mathbf{r}) \exp(-i\mathbf{q} \cdot \mathbf{r}) d\mathbf{r} \right|^2 . \tag{3.15}$$

As aforementioned, we monitor the time evolution of I at a fixed $\mathbf{q}$=q_z value. Since only single-scattering events are considered, one can split the scattering in two parts, corresponding respectively to scattering from the substrate (time independent) and from the growing thin film with n monolayers (time dependent). The reflected intensity becomes[79]:

$$I_{reflected}(t) = \left| \underbrace{A_{substrate}(q_z) \cdot \exp(i\phi(q_z))}_{I_{substrate}} + \underbrace{f(q_z) \cdot \sum_n \theta_n(t) \exp(inq_z d)}_{I(t)_{thinfilm}} \right|^2 \tag{3.16}$$

$A_{substrate}(q_z)$: substrate scattering amplitude
$f(q_z)$: molecular form factor
$\phi(q_z)$: phase between substrate and ad-layer scattering
n: layer number
$\theta_n(t)$: fractional coverage of the n-th layer
q_z: X-ray wave-vector transfer upon reflection
d: out-of-plane lattice spacing within the crystalline thin film.

This allows us to evaluate the time evolution of $I_{reflected}(t)$ at a specific q_z-point. One of the most prominent choices is the anti-Bragg point, where $q_z = q_{anti-Bragg} = 1/2 \cdot q_{Bragg} = \pi/d$. Inserting $q_{anti-Bragg}$ in equation (3.16), one finds that the individual reflections of directly neighboring layers will interfere destructively. The second term in equation (3.16) can then be denoted as:

$$I(t)_{thinfilm} = f(q_z) \cdot (\theta_1(t) - \theta_2(t) + \cdots - \cdots). \tag{3.17}$$

The alternation of the sign is the origin for the oscillations of $I_{reflected}(t)$ in time, referred to as growth oscillations. At the anti-Bragg point the period of growth oscillations will equal 2 ML's and each minimum and maximum of a growth oscillation curve will correspond to the completion of one ML, see Fig. 3.6. In a perfect layer-by-layer growth scenario there is no simultaneous growth of more than one ML, so $I_{reflected}(t)$ will oscillate between a fixed minimum and maximum. However, if

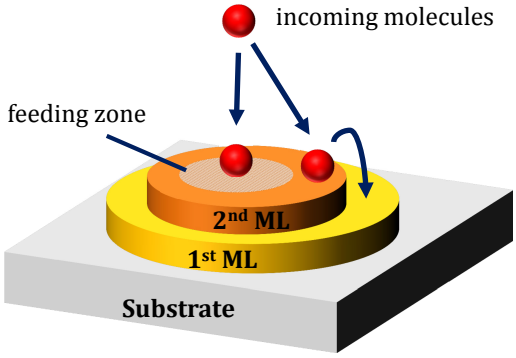

Figure 3.7: Illustration of the feeding-zone concept as used in the rate-equation model and applied to fit growth oscillations. Each molecule landing inside the feeding zone on top of an island will stay inside this zone and initiate the formation of the next monolayer. In contrast, molecules landing outside the feeding zone will be transported downwards and contribute to the lateral growth of the island. The area of the feeding zone changes with deposition time.

the film roughens, several ML grow simultaneously, since island nucleation on top of a ML sets in before the layer is complete. As evident from equations (3.16) and (3.17) such a process will induce a damping of $I_{reflected}(t)$ with time as shown in the example in Fig. 3.6 b). Consequently, comparing the damping of growth oscillations on a qualitative level allows us to conclude on the velocity of film roughening.

3.2.3.2 Trofimov-model / rate equation model

For a quantitative analysis and fits of the growth oscillations, a model for the temporal evolution of the coverage θ_n from equation (3.16) is needed. In the past, different growth models have been successfully applied to describe the growth of a number of different molecular thin films.[78,80,101,106] The growth model we use in this thesis, is based on a distributed growth model proposed by Trofimov *et al.*[107] However, the original model by Trofimov describes the growth in both the in- and out-of-plane directions. Therefore a simplification is used prior to applying this model to growth oscillations, where only the film growth in the out-of-plane direction is investigated.

The simplified Trofimov model, as introduced by Woll *et al.*[101], describes the growth process only via the growth rate R_n and the effective critical layer coverage $\theta_{n,cr}$ of each layer as shown in eq. (3.18) and (3.19). The critical layer coverage of the n-th layer $\theta_{n,cr}$ gives the coverage of layer n before the $(n+1)$-th layer starts to nucleate and grow on top of the n-th layer. The feeding zone parameter ξ_n marks

the size (in units of coverage) of the zone on top of the n-th layer. Molecules landing inside this zone will contribute to nucleation and growth of the (n+1)-th layer. In contrast molecules landing in the region outside the feeding zone will diffuse over the edge into the n-th layer. This is schematically sketched in Fig. 3.7. The rate equation then reads:

$$\frac{d\theta_n}{dt} = \begin{cases} R_1(1-\theta_1) + R_{n>1}(\theta_1 - \xi_1), n = 1 \\ R_{n>1}(\xi_{n-1} - \xi_n), n > 1, \end{cases} \tag{3.18}$$

with the size of the feeding zone given by

$$\xi_n = \begin{cases} 0, \theta_n < \theta_{n,cr} \\ 1 - e^{-\left[\sqrt{-ln(1-\theta_n)} - \sqrt{-ln(1-\theta_{n,cr})}\right]^2}. \end{cases} \tag{3.19}$$

Using the Trofimov model we can fit the growth oscillations at any q_z point. As mentioned, at the anti-Bragg point, q_z=$1/2q_{Bragg}$, an oscillation period of 2 ML is observed. At other q_z-values, e.g. $2/3q_{Bragg}$, $3/4q_{Bragg}$, $4/5q_{Bragg}$ etc., the oscillation period will be 3 ML, 4 ML, 5 Ml etc., as can be followed from equation (3.16) and as described in detail in ref. [79]. If the experimental setup offers a precise and - in terms of the growth speed - sufficiently fast sample positioning combined with a high X-ray intensity, it is advisable to monitor growth oscillations quasi-simultaneously at different q_z positions. This allows one to further constrain the fit parameters, since only $A_{substrate}$, ϕ and f will differ for the fits at different q_z points. A further advantage is the gain of additional information from the oscillations at higher q_z values. For example, in the case of fast roughening, the anti-Bragg oscillations may be strongly damped. But in combination with the oscillations at larger q_z values, a fit of the physical parameters such as ML thickness and ML growth rate will still be possible within the Trofimov model. We will describe such a scenario in section 5.3 for the case of 6P growth on non-polar ZnO surfaces.

Examples of growth oscillations at different growth-modes

By using simulated examples, we want to illustrate how the film roughening with deposition time (or film thickness) influences the growth oscillations recorded at the anti-Bragg point. We show in Figs. 3.8 a) and c) two opposite extremes with a perfectly smooth layer-by-layer (LBL) growth in a) and an extremely rough growth in c). In Fig. 3.8 b) an intermediate growth mode shows the ongoing transition from LBL growth to 3d growth (layer + island growth).

As discussed in section 2.1, a perfect LBL growth is characterized by a strict growth sequence of the individual MLs. The growth of a consecutive ML n+1 starts only when the preceding layer n completely covers the surface, i.e. only when $\theta_{cr,n}$=1. In such a case, the growth oscillations are not damped and the intensity of the reflected X-ray beam oscillates between a constant minimum and maximum. As evident from the RMS roughness evolution curve, the roughness in perfect LBL growth is zero each time the growth of a monolayer is finalized. A prerequisite for such growth is an efficient downward transport, e.g. due to a small Ehrlich-Schwoebel-barrier.

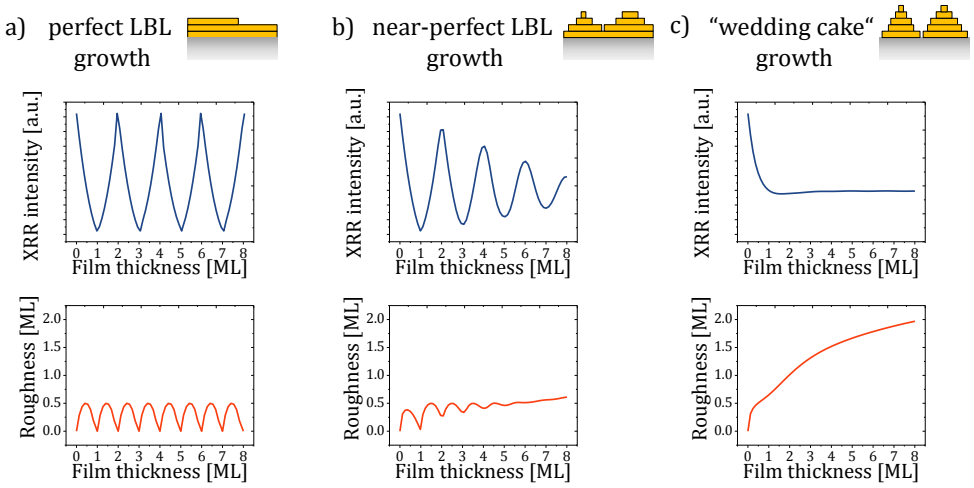

Figure 3.8: Examples of simulated XRR growth oscillations at the anti-Bragg point and the corresponding roughness evolutions for different growth-modes. a) and c) represent the respective extreme modes of thin film growth: ideal layer-by-layer (LBL) growth and rough 3d growth. In b) the ongoing transition from ideal LBL growth to 3d growth is displayed.

Although desired, such a perfect LBL growth will most likely not be observed for real organic systems. Even for the very smooth growth of C_{60} on mica, the growing film continuously deviates from the LBL growth mode and roughens with time.[34] The amplitude of the growth oscillations will be damped as shown in a modeled example in Fig. 3.8 b). The corresponding roughness curve shows in the beginning the same progress as in the LBL mode, but then constantly deviates and finally a steady increase of the roughness with time is observed. In the extreme case of wedding cake growth shown in Fig. 3.8 c) not a single growth oscillation can be observed and the film roughness increases continuously. The ML's do not close, i.e. θ_n is never unity which may be, e.g., due to a high Ehrlich-Schwoebel barrier. Interestingly, such a growth behavior was observed in real systems.[108] The simulated curves in Figs. 3.8 a)-c) have been produced with the software *TroFit*,[21] which has

been used throughout this thesis to fit the experimental growth oscillations.

3.2.4 Studying the in-plane morphology with GISAXS

Grazing incidence small angle X-ray scattering (GISAXS) constitutes an experimental method to probe the in-plane morphology of thin films. In section 4.1 we apply GISAXS to unravel island densities of growing organic thin films. Here we want to briefly introduce the working principle of the method.

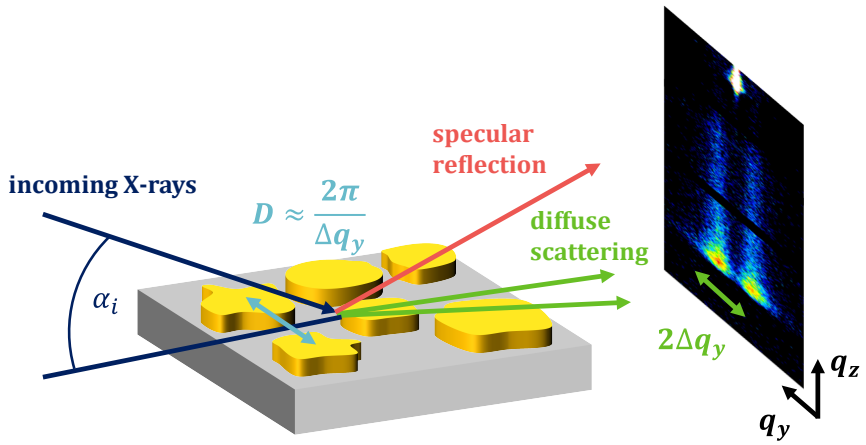

Figure 3.9: Sketch of a GISAXS measurement. Incoming X-rays are scattered diffusively at the islands which gives rise to two peaks on the detector along the q_y direction. The spacing of the peaks, $2\Delta q_y$ is inversely proportional to the mean-island distance L, which can be used to calculate island densities.

A typical setup for GISAXS measurements is shown in Fig. 3.9. X-ray beams impinge the sample under a small, grazing angle α_i. Parts of the X-rays will be reflected specularly, which is the aforementioned XRR signal and can be observed as a bright spot on the detector at q_y=0, $q_z \neq$0. However, a minor part of the incoming photons will be scattered diffusively by the objects on the sample, e.g. by islands, and two side peaks will appear on the detector at $|q_{y1}|$=$|q_{y2}|$=$\Delta q_y \neq$0. Mathematically the observed scattered intensity in q_y-direction can be described as the product of the form factor $F(q_y)$ and the structure factor $S(q_y)$:

$$I(q_y) \approx |F(q_y)|^2 \cdot S(q_y). \tag{3.20}$$

$F(q_y)$ is the Fourier transform of the island shape and carries information, e.g., on the diameter of roundish islands. The structure factor $S(q_y)$ is an inter-island correlation or interference function and constitutes the Fourier transform of the

spatial arrangement, i.e., the position of the islands. The position of the appearing side peaks Δq_y is inversely proportional to the mean distance between the center of masses of the islands L, with $L = 2\pi/\Delta q_y$.[81,109] In our experiments we will use this relationship to calculate the density of islands and its temporal evolution from time-dependent GISAXS measurements. We will compare these quantities with measurements of established imaging techniques like AFM. Detailed information on the shapes, sizes and orientations of the objects requires a precise analysis of the GISAXS profiles as done in literature.[110–113] At this point we also mention the powerful software packages for the simulation of the GISAXS profile of complex samples comprising objects of different shapes and distributions.[114,115]

3.2.5 X-ray sources for scattering experiments

The X-ray scattering experiments of the present thesis have been performed at different X-ray sources, which can be categorized into lab- and synchrotron-based. Here, we want to briefly introduce the sources we have used.

3.2.5.1 Lab-based X-ray source - *EFG* diffractometer

The laboratory facilities in the working group include a diffractometer by *EFG GmbH*. The setup is shown on a photograph in Fig. 3.10 a). It comprises an X-ray generator from *Rigaku*. The UHV deposition chamber, as presented in detail in section 2.2.1, can be mounted on a *Huber* positioning stage. In the laboratory experiment setup X-rays are generated as a result of a collision of electrons with a copper (Cu) anode 3.10 b). The electrons are emitted via thermal emission from a hot filament wire and accelerated in vacuum towards an anode by an applied electric field (here 50 kV). When the electrons hit the Cu target, they are rapidly decelerated. The main part of their kinetic energy is transformed into heat, which requires the target Cu anode to be watercooled. However, a minor part of the electrons from the beam will contribute to the emission of electromagnetic radiation either in the form of *Bremsstrahlung* or *characteristic X-ray radiation*. *Bremsstrahlung* is emitted when the partly or completely decelerated electrons transfer their kinetic energy loss into X-ray radiation energy. A continuous energetic spectrum is obtained for this radiation process, with a maximum radiation energy corresponding to the highest kinetic energy of the electrons. A different mechanism is behind the emission of *characteristic X-ray radiation*. Here, the incoming electrons eject electrons from the inner shells of the atoms of the target material, e.g., from the Cu K-shell. The vacant level will be filled by electrons from higher shells, e.g., from the L-shell, which hop

down under emission of X-ray radiation of a characteristic wavelength, s. inset of Fig. 3.10 c). In the example of L-shell electrons filling up the K-shell, the emitted radiation is referred to as K_α. At the same time Cu K_α constitutes the strongest characteristic emission for copper anodes and corresponds to an energy of 8.05 keV or a wavelength of 1.54 Å. The selection of this single photon energy is realised by a monochromator, e.g., in the form of two Göbel mirrors. In the shown laboratory setup the anode is constantly rotated, which increases the maximum photon flux, being in the range of 1-6 $\cdot$ 10^8 photons/second.

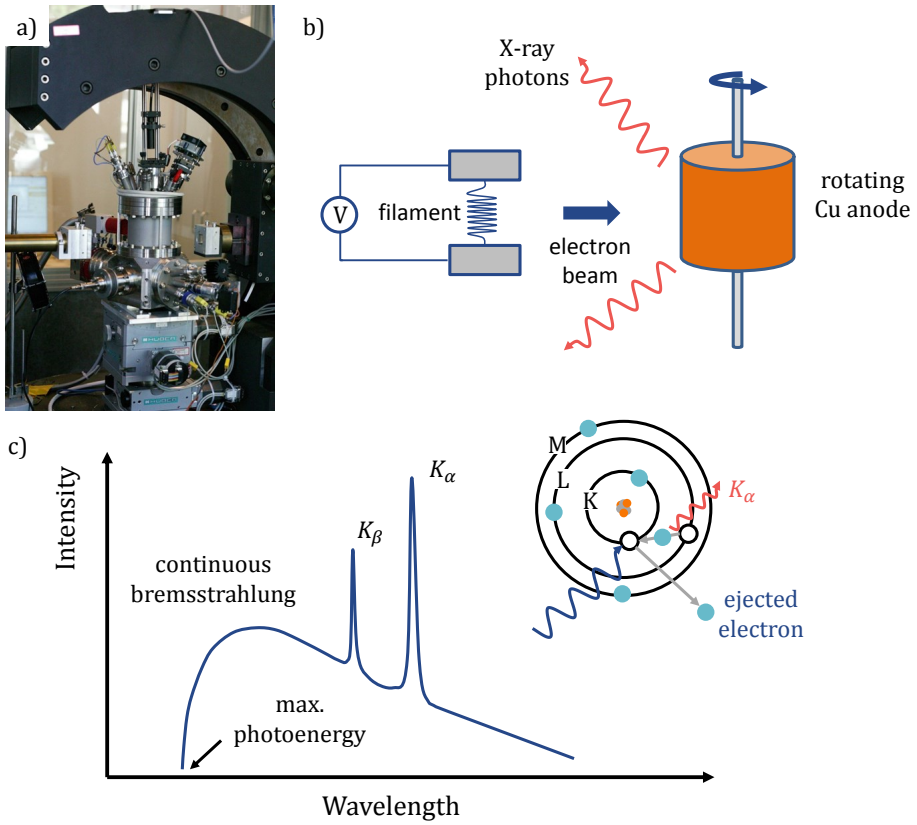

Figure 3.10: a) Photograph of the lab-based X-ray diffractometer with the UHV chamber mounted on a positioning stage, with the beam impinging from the left side. b) Sketch of the working principle of lab-based X-ray generation by using a rotating Cu anode. c) Scheme of the electromagnetic radiation emitted by the accelerated electrons when hitting the Cu target anode. Inset: Physical principle of the origin of characteristic X-ray radiation. Accelerated electrons can eject atomic electrons of the target material from their inner shells. The vacant position is filled with electrons hopping from higher shells under emission of characteristic radiation.

As can been from the photograph of the *EFG* setup, the beam tube is fixed. In order to perform X-ray reflectivity or grazing incidence X-ray diffraction experiments the chamber is mounted on the *Huber* positioning system, which can be rotated and tilted. Furthermore, the detector can be moved along the hemispherical construction, which also can be rotated in-plane.

3.2.5.2 Synchrotron-based X-ray sources

Significant parts of the X-ray experiments of this thesis have been performed at synchrotron light sources. In a synchrotron, a charged particle beam, e.g. electrons, is moving on a circular trajectory at relativistic velocities in ultrahigh vacuum storage rings, see Fig. 3.11 a). The magnetic field of so-called bending magnets is used to influence and enforce the circular motion of the particle. By passing the magnets, the trajectory of the electron is bent to fit to the curvature of the ring, Fig. 3.11 b). Every change of the moving direction of the electrons can be regarded as a change of the electron acceleration, which is accompanied by the emission of the broadband synchrotron radiation. In addition to bending magnets, synchrotrons are equipped with straight sections of undulators. Undulators consist of an array of dipole magents, whose magnetic field forces the electrons to an oscillating trajectory, as shown in Fig. 3.11 c). Thus, passing each single magnet, the electrons emit radiation, which interferes with the radiation generated from passing the other magnets. The overlapping radiation results in a much more directed and brilliant photon beam compared to the one from the bending magnets, but it is still polychromatic. The emitted X-ray radiation is further directed towards so called beamlines, being constructed tangentially to the ring. Commonly before being inserted in the experimental hutch, where the scattering experiments are performed, the beams pass a so called optics hutch. The hutches are usually equipped with a monochromator, allowing to select the beam energy. Furthermore by using X-ray mirrors and refractive Fresnel lenses or Kirkpatrick-Baez mirrors, a focusing of the beam is achieved as demanded for the specific profile of each single beamline.

Compared to lab-based X-ray sources, synchrotrons offer a several orders of magnitude higher brightness, a smaller angular beam divergence and the possiblity to choose the energy of the X-rays. Consequently, monitoring of weak scattering features and of fast real-time processes is significantly facilitated. However, especially for organic materials a collimated and high intense beam can seriously damage the sample. Thus, it is essential to check for beam damage and properly adjust the experiment to preserve the probe (e.g. decreasing the beam intensity/counting times

or using fresh spots on the sample).

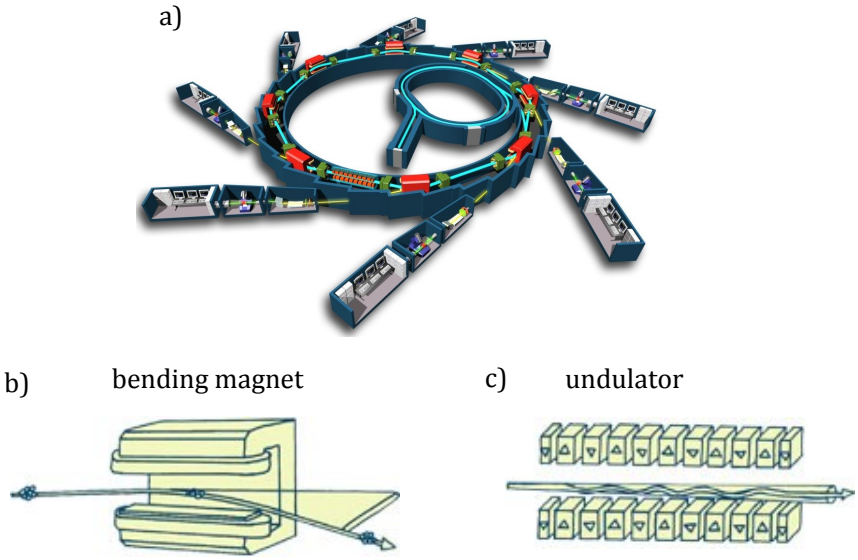

Figure 3.11: a) Sketch of a synchrotron showing the circular storage ring and the tangentially constructed beamlines for X-ray scattering (printed with permission, copyright EPSIM 3D/JF Santarelli, Synchrotron Soleil). b) When passing a bending magnet, the trajectory of the electron beam is bended and *Bremsstrahlung* is emitted. c) When the electron beam passes an undulator, its pathway oscillates due to the influence of the magnetic fields of a series of dipolar magnets. Each change in the direction of motion causes the emission of X-rays, which interfere and overlay to a bright beam. Figs. b) and d) are taken from ref. [116] and printed with permission of the copyright holder, the ESRF.

3.2.5.3 P03 Beamline at PETRA III, DESY Hamburg

The X-ray experiments discussed and analyzed in section 4.1 have been performed at the Micro- and Nanofocus X-ray Scattering P03 beamline at the PETRAIII synchrotron of the DESY (Deutsches Elektronen-Synchrotron) in Hamburg, Germany. The available X-ray energy range is 8-23 keV. A photograph of our experimental setup is shown in Fig. 3.12. The portable deposition chamber is mounted on the local *Huber* goniometer for sample positioning in the angular and translational direction. At the end of an about 5 m long flighttube a large two-dimensional detector is mounted (PILATUS 300K by *Dectris*). The flighttube is evacuated to exclude air scattering. The long detector-sample distance together with the high dynamical range and the small 172 x 172 µm^2 pixel size, allows to resolve the evolution of characteristic in-plane features of growing organic films by GISAXS. However, due to the large area of the detector, simultaneous XRR growth oscillations can be monitored providing additional information on the evolution of the out-of-plane structure.

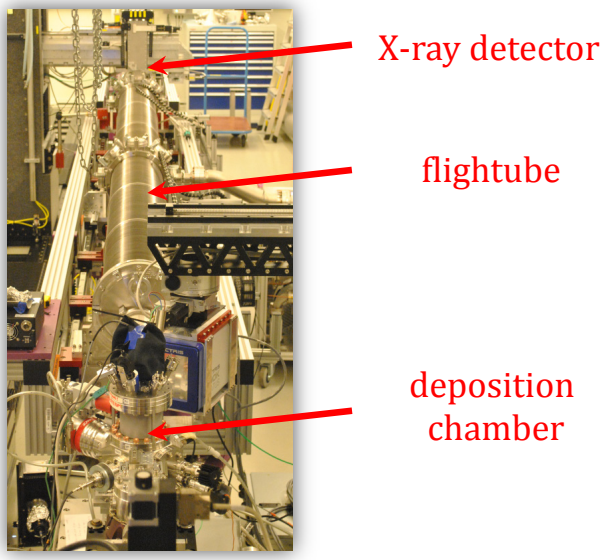

Figure 3.12: Photograph of the experimental setup at the P03 beamline.

3.2.5.4 ID03 Beamline at the ESRF, Grenoble

All X-ray experiments shown in section 5.3 of this thesis have been performed at the ID03 surface diffraction beamline of the European Synchrotron Radiation Facility (ESRF) in Grenoble, France. At ID03, the energy of the incoming beams can be adjusted in the range of 5-24 keV, while the photon flux is in the range of 10^{13} ph/s and thus five orders of magnitude higher than in the lab-based system. For the experiments our growth chamber was mounted on the local hexapod positioning system providing angular and translational degrees of freedom. An areal *MAXIPIX* [117] photon-counting detector was used for data acquisition.

4 Results: Understanding organic thin film nucleation and growth by X-ray scattering

In this chapter we will present, analyze and discuss experiments performed with the aim of enhancing the understanding of important processes governing organic growth and structure formation. Such processes are e.g. nucleation, molecular diffusion and stable island formation. While within this thesis we also analyzed *ex situ* the structural ordering of grown ultra-thin molecular films, as exemplary demonstrated in appendix A.1, here we focus on the dynamic aspects of multilayer film formation studied *in situ* and in real-time. In particular, we present results on the growth of the functional small molecule PTCDI$-C_8$ on silicon oxide substrates, which have been published in ref. [118].

4.1 Studying the evolution of PTCDI$-C_8$ nucleation beyond the 1st ML

In what follows, we study the growth of the prototypical PTCDI$-C_8$ molecule, by applying an advanced combination of simultaneous *in situ* real-time synchrotron XRR and GISAXS measurements. From XRR growth oscillations, as discussed in section 3.2.1, we gather information about the evolution of the out-of-plane film morphology. From complementary *in situ* GISAXS measurements as introduced in section 3.2.4, we evaluate the in-plane information. Therefore the combination of both techniques contains rich information on the nucleation behavior of the molecule.

In contrast to similar investigations, we extend the focus of our growth study beyond the common first (sub-) ML. This enables us to identify significant differences in the growth of the 1st and 2nd ML, including an increased molecular adsorption probability and a transition of the island shapes from roundish in the 1st ML to

rectangular in the 2nd ML. Furthermore we determine a lower island density in the 2nd ML, which points towards an enhanced in-plane diffusion of the molecules. To probe this, we first evaluate the evolution of the maximum island density N_{max} as a function of the substrate temperature T and the growth rate GR and make use of mean-field nucleation theory to fit the scaling of N_{max}. We apply not only the frequently used diffusion limited aggregation (DLA) model, but also the attachment limited aggregation (ALA) model, as recently established for organic molecular growth.[47] We find the same critical nucleus size i in both MLs, but a 70 meV lower nucleation energy E_{nuc} in the 2nd ML. From the fits we also evaluate the attempt frequencies ν_0, which are in the order of $10^{19}s^{-1}$-$10^{20}s^{-1}$ and therefore larger than for atomic systems. Combining these results, we find a 140 meV decrease of E_d and correspondingly an increase in the molecular diffusivity in the 2nd ML, explaining the decreased island density. We further discuss potential differences of the molecular thermalization in different MLs by applying the hot-precursor model of nucleation theory.[48]

4.1.1 The organic semiconductor PTCDI−C_8

Before moving on to the details and results of our study on the growth of PTCDI−C_8, we would like to first summarize preceding works. We stress out that our selection is not complete and is meant as a brief introduction on the used material.

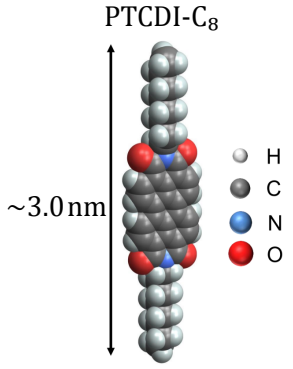

Figure 4.1: Sketch of the PTDCDI−C_8 molecule, which is a perylene derivative and is built up of hydrogen, carbon, nitrogen and oxygen.

The perylene derivative PTCDI−C_8, *N,N'*-dioctyl-3,4,9,10-perylene tetracarboxulic diimide ($C_{40}H_{42}N_2O_4$), is built up of a PTCDI backbone with two octyl chains at its termini, s. sketch in Fig. 4.1. The chains possess rotational freedom, so that the molecule is not stiff as the sketch may imply. PTCDI−C_8 is known to grow

in a highly crystalline fashion and nearly upright standing orientation on silicon oxide. Further, it shows a significant n-type semiconducting behavior with a reported electron mobility of up to 1.7 cm^2/Vs.[119,120] The molecule has already been successfully implemented in OFETs and organic solar cells.[121–124] However, aside from a recent publication on the growth of pentacene/PTCDI−C_8 bilayer systems,[63] little is known about the decisive initial stages of PTCDI−C_8 nucleation and growth in the first few MLs, which crucially impact the functionality of a potential device. The unit cell of PTCDI−C_8 contains two molecules and was determined in ref. [119]. It is possible to substitute the octyl chains by alkyl chains of a different length to synthesize related molecules, which all can be symmarized by the chemical formula PTCDI-C_n. Known representatives are e.g. PTCDI−C_5 and PTCDI−C_{13}, which also exhibit n-type semiconducting behavior and likewise grow in a nearly upright standing fashion on different tested substrates.[25,122,125,126]

4.1.2 Experimental procedures

The PTCDI−C_8 (Sigma Aldrich, purity >98.5 %) molecules were deposited via organic molecular beam deposition (OMBD) in a vacuum chamber at a base pressure below $3.0 \cdot 10^{-7}$ mbar on silicon wafers covered with a native oxide layer at substrate temperatures of 30 to 100 °C and growth rates of 0.01, 0.1 and 1 nm/min. Deposition details are described in chapter 2.2.1. For information on the substrate preparation and cleaning the reader is referred to chapter 2.2.2.

The X-ray scattering experiments were performed at the MiNaXS P03 beamline of PETRAIII[127,128] at the DESY synchrotron in Hamburg, Germany at a wavelength of $\lambda = 0.0957$ nm (see chapter 3.2.5.3). The intensities of the specular reflection and of the diffuse X-ray scattering (in grazing incidence small-angle X-ray scattering -GISAXS - geometry) were monitored simultaneously on a Dectris PILATUS 300K detector *in situ* and in real-time during the thin film growth as schematically shown in Fig. 4.2. During all growth experiments the angle of incidence was kept fixed at α_i=0.67 °, which equals an out-of-plane scattering vector $q_z = 4\pi/\lambda \cdot \sin(\alpha_i) = 1.54\,\mathrm{nm}^{-1}$. This value corresponds to the so-called anti-Bragg point of the (001) PTCDI−C_8 Bragg reflection $q_z = 1/2 \cdot q_{Bragg}$. To avoid beam damage we linearly translated the sample perpendicular to the incident beam during the real-time growth. The AFM images were recorded on a Bruker MultiMode 8 in ScanAsyst PeakForce tapping mode (see section 3.1). For the acquisition we used 2 N/m tips (Olympus).

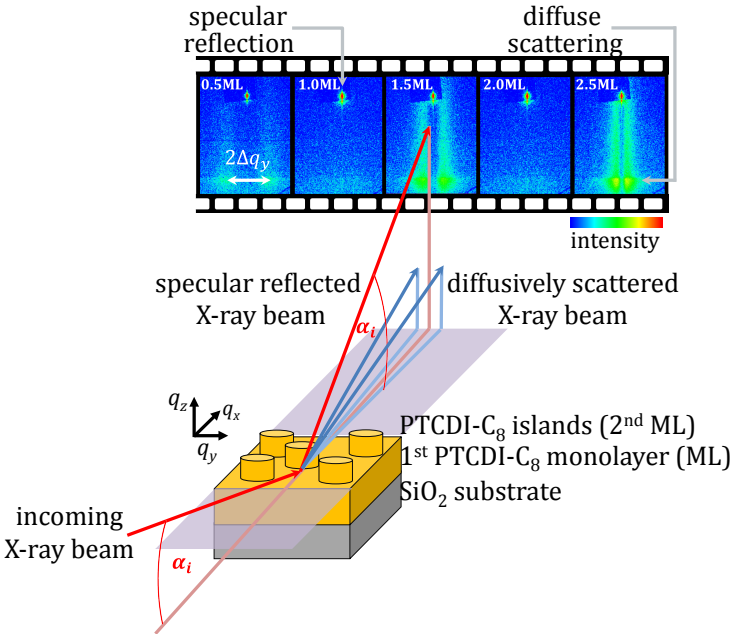

Figure 4.2: Scattering geometry during the growth of PTCDI−C_8 on silicon oxide. The simultaneous measurement of the specular reflected and diffusively scattered signals is performed as a function of time.

4.1.3 *Ex situ* morphology of PTCDI−C_8 films at different growth stages.

In Fig. 4.3 characteristic AFM images of PTCDI−C_8 films are shown as a function of substrate temperature and film thickness (growth rate = 0.1 nm/min). The molecules assemble in a nearly upright standing fashion and form islands of about 1 ML height. For higher substrate temperatures and film thicknesses we find a decreasing island density. In thicker films simultaneous growth of more than one layer is observed, indicating a slow transition from a layer-by-layer (LBL) growth towards a rougher 3d growth mode with increasing thickness. Further, islands in the 1st ML have a roundish shape, which changes in the 2nd and higher MLs towards anisotropic, elongated, rod like islands with almost rectangular edges. The form of these islands is comparable to earlier studies[120] of several ML thick PTCDI−C_8 and is also similar to PTCDI−C_{13} islands.[25] Anisotropic island shapes indicate the existence of preferential growth directions due to different surface energies of the crystal facets as well as different growth speeds of different facets.[129]

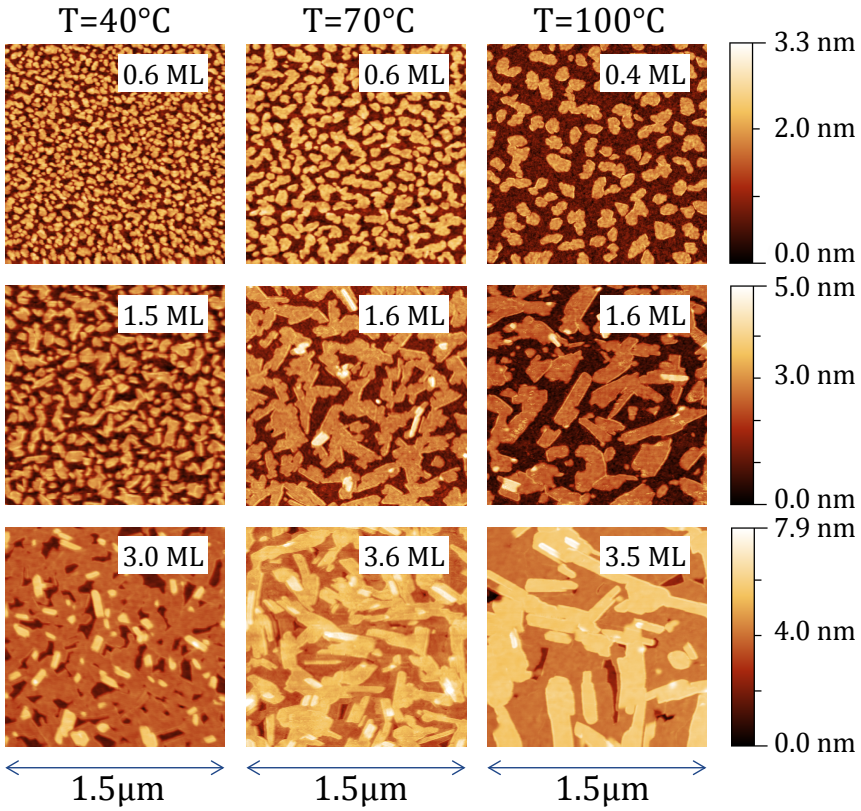

Figure 4.3: *Ex situ* AFM snapshots ($1.5 \times 1.5\,\mu m^2$) of 0.5 to 3.6 ML thick PTCDI−C_8 films grown at three different temperatures. A decrease in the island densities for higher substrate temperatures is visible.

4.1.4 Time-dependent roughness evolution and layer-dependent molecular adsorption studied *in situ*

While AFM yields real space information about the thin film morphology, it is usually not feasible to obtain *in situ* and real-time information during the growth e.g. due to tip shadowing effects. In contrast, it is possible to follow thin film growth in real-time with X-ray scattering experiments. Our setup, see Fig. 4.2, allows us to simultaneously collect information about the evolution of the in- and out-of-plane morphology.

To monitor the evolution of the out-of-plane morphology of the growing PTCDI−C_8 film, we applied *in situ* real-time X-ray reflectivity (XRR) measurements at the anti-Bragg point of the PTCDI−C_8 (001) crystal plane ($q_{anti-Bragg} = 1/2 \cdot q_{Bragg}$). With increasing molecular exposure (exposure time × growth rate) we observe characteristic growth oscillations of the XRR intensity with a period of two MLs. These originate from alternating constructive and destructive interferences of the X-ray

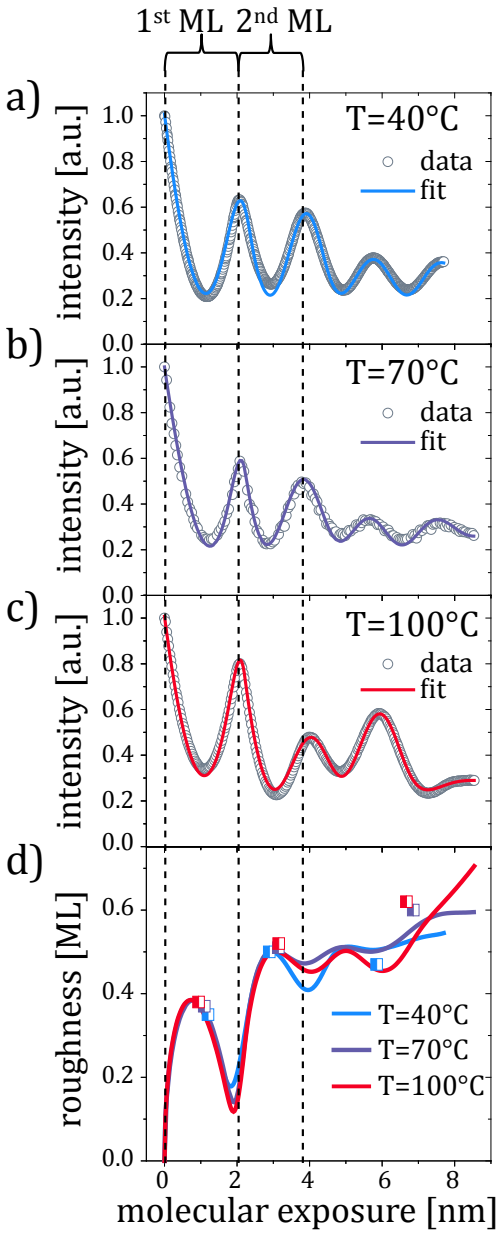

Figure 4.4: a) - c) Oscillations of the intensity of the specular reflected X-ray beam at the anti-Bragg point acquired *in situ* during the PTCDI−C_8 growth contain information about the time-evolution (molecular exposure = exposure time × growth rate) of the out-of-plane film morphology. The damping of the oscillations is a measure of film roughening indicating a growth-mode transition from layer-by-layer to a rough 3d growth. The solid lines show the best fits of the anti-Bragg oscillations using a rate equation model. d) Evolution of the surface roughness as calculated from the model (continuous lines) and from the AFM images (half-filled squares).

reflections from the individual PTCDI−C_8 MLs.[79] As displayed in Figs. 4.4 a)- c) PTCDI−C_8 exhibits growth-oscillations for several MLs. Such persistently smooth growth has been also observed for the similar PTCDI−C_{13} molecule.[25] As described in more detail in section 3.2.3, the damping of the oscillations depends on the film roughness and hence indicates a slow transition from a smooth layer-by-layer (LBL) growth towards a rougher 3d growth-mode with increasing film thickness, which is in agreement with our observations from the AFM snapshots. This transition proceeds slower than for other organic molecules like pentacene,[77] diindenoperylene,[79] or *para*-sexiphenyl.[104]

We fit the growth oscillations using the software Trofit 0.7.9,[21] which is based on a model by Trofimov *et al.*[107] and Woll *et al.*[101] and has been applied previously in refs.[83],[104] and[21]. The fits allow us to quantify the height and effective growth rate of the individual MLs and thus the time evolution of the film roughness. The continuous lines in Figs. 4.4 a)-c) show the good agreement of the fits with the data and the calculated roughness evolution is plotted in Fig. 4.4 d). The roughness oscillates between low values for completely closed layers and high values for half-filled layers. Further, the roughness continuously increases due to the slow transition from the LBL growth to a 3d growth mode. The half-filled squares in Fig. 4.4 d) correspond to roughnesses obtained directly from the AFM images. We observe a good agreement with the values from the anti-Bragg fits.

From the anti-Bragg fits we determined also the layer thickness and effective growth rates of the individual MLs. Independent of the substrate temperature and growth rate a layer thickness of about 2.0 nm was determined for each ML corresponding to almost upright standing molecules. Concerning the effective growth rate, we find that the 1st ML growth proceeds on average 1.4 times slower than the growth of the 2nd and the subsequent MLs. This finding can also be directly deduced from Figs. 4.4 a)-d), where it is clearly visible that it takes less exposure time to accomplish the 2nd ML than the 1st. A slower growing 1st ML was also observed in a study of the similar PTCDI−C_{13} molecule on diverse substrates,[25] where it was attributed to a coverage-dependent adsorption probability of the molecules.

4.1.5 Temperature and growth rate dependent island densities studied by *in situ* real-time GISAXS.

In addition to the out-of-plane information from the anti-Bragg oscillations we simultaneously monitored the time evolution of the GISAXS scattering to determine the time evolution of the island density N. In Fig. 4.5 a) we show the signal on the X-ray detector as measured for a 0.5 ML PTCDI−C_8 film in the scattering geometry of Fig. 4.2 during the growth at a substrate temperature of 70 °C and a growth rate of 0.1 nm/min. We observe two separated bright spots in the GISAXS measurement shown in Fig. 4.5 a). After vertically line-integrating the GISAXS signal in the region of interest (red rectangle) we obtain an intensity distribution in the reciprocal space as shown by the red curve in Fig. 4.5 c). The spacing $2\Delta q_y$ is inversely proportional to the mean island distance L, with $L = 2\pi/\Delta q_y$.[109] According to our simulations with the GISAXS software BornAgain 1.3.0[115] the peak spacing is predominantly determined by the mean island spacing, while the influence of the island size and form is insignificant for the peak position.

To demonstrate the equivalence of the GISAXS analysis with the established AFM methods for determining the island density, we directly compare both techniques. An example is given in Fig. 4.5 b), where we show an AFM image of a 0.5 ML PTCDI−C_8 film deposited at 70 °C and the corresponding 2d fast Fourier transformation (FFT) of this image. A line scan through the center of the so-called Henzler ring[82,130,131] results in an intensity distribution in the reciprocal space. In equivalence to the GISAXS measurement, the peak spacing $2\Delta q_y$ is related to the mean island distance $L = 2\pi/\Delta q_y$. As shown in the example of our datasets in Fig. 4.5 c), the GISAXS (red) and FFT-AFM (grey) curves agree well yielding the same mean island distance L.

The high brilliance of the MiNaXS beamline and the dynamic range of the PILATUS 300K detector enable us to acquire 10-15 frames/ML similar to the one shown in Fig. 4.5 a) during the growth of PTCDI−C_8. Technically even higher time resolutions are possible, but we set this artificial limit to avoid beam damage. An example of the time evolution of the GISAXS intensity distribution is displayed in Fig. 4.6 a). For a bare substrate or for a smooth, closed ML essentially no GISAXS signal is acquired. However, with the emergence of molecular islands the GISAXS intensity increases. Subsequently, these islands grow laterally and coalesce, so that the mean island distance $L = 2\pi/\Delta q_y$ increases. We thus observe that both the intensity and the peak spacing oscillate with a period of 1 ML.

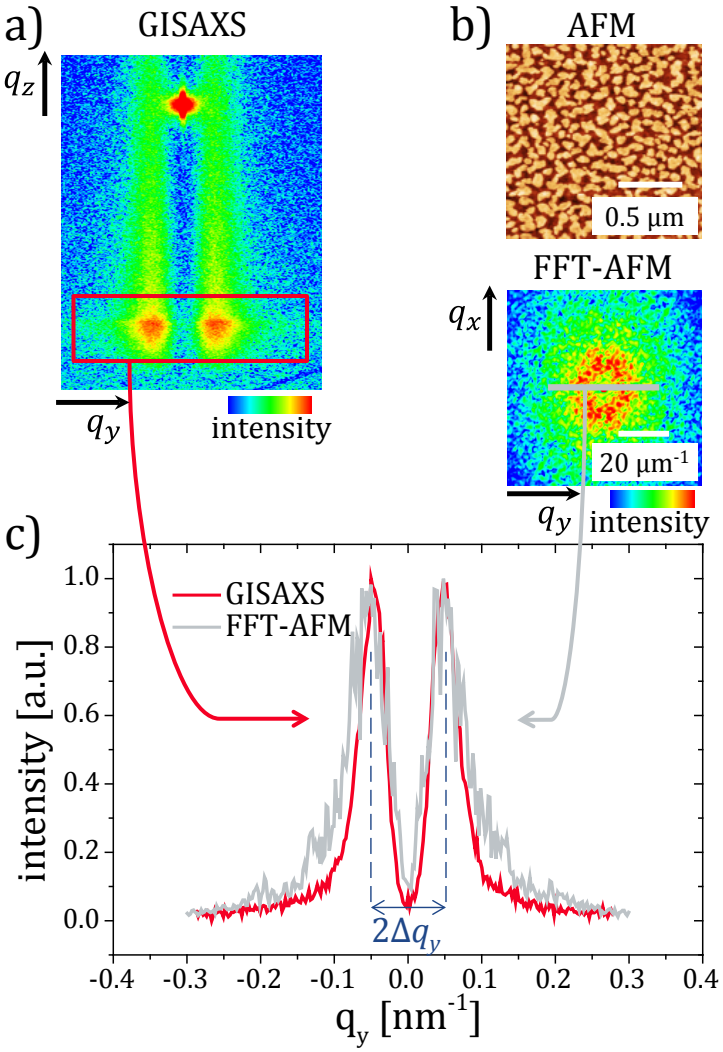

Figure 4.5: Determination of the mean island-distance $L = 2\pi/\Delta q_y$ of a 0.5 ML thick PTCDI−C_8 film deposited at 70 °C from independent a) GISAXS and b) AFM measurements. The integrated intensity (along q_z) in the GISAXS region of interest (red rectangle) is plotted as a red line in c). The characteristic real-space length scales of the AFM image in b), appear as rings in the reciprocal space of the FFT-AFM image. A line scan through the ring yields the gray intensity distribution curve in c). Good agreement of GISAXS and FFT-AFM intensity distributions is achieved c), showing the same peak spacing $2\Delta q_y$ and hence the same mean island distance L.

By using $N = \frac{2}{\sqrt{3}} \cdot \frac{1}{L^2}$ we can calculate the island density N from the GISAXS peak spacing assuming a hexagonal packing. The so obtained island density as a function of the molecular exposure is plotted in Fig. 4.6 b) for a variation of the substrate temperature (GR=0.1 nm/min) and in Fig. 4.6 c) for a variation of GR (T=80 °C). Note, that the island density of PTCDI−C_8 can be tuned by around two orders of magnitude via increasing the substrate temperature by 60 °C. The values of N in the beginning or end of a ML growth are deduced from weak scattering signals of very small islands (or holes in the film). Therefore the accuracy can be influenced by other weak scattering contributions around q_y=0 nm^{-1} originating from the substrate, as well as weak GISAXS intensity due to the small roughness of a lower lying complete ML. We indicated the corresponding regions in Figs. 4.6 b) and c) as dashed lines as a guide to the eye.

For comparison, the island densities from FFT-AFM images are plotted as half-filled squares in Fig. 4.6 b). Qualitatively a good agreement of both datasets is achieved with the island densities deduced from FFT-AFM showing the same trend of larger islands at higher temperatures and in the higher MLs. Quantitatively the values obtained by the two different methods deviate on average by about 50 %. One of the reasons for such deviations is a different statistical average. GISAXS samples an X-ray footprint of 10 mm × 30 µm and provides thus a better statistical average compared to the AFM, where the image size is in the range of 100 µm^2. As a result fluctuations in the AFM are observed from image to image. This statistical error may be estimated to be in the order of $\sqrt{N \cdot \text{area}}$. Another aspect, which should be taken into account when analyzing the deviations of the island densities, is the dependency of N on the mean island distance L. Due to $N \propto \frac{1}{L^2}$ even small differences in the determination of L by AFM and GISAXS are more pronounced in N, since L enters quadratically. Furthermore the deviations in N may also result from post-growth transformations of the film morphology. While with GISAXS we probe the film *in situ*, the AFM images are taken *ex situ*. As a result, the contact with ambient air, but also effects like wetting or partial desorption may influence the morphology and, thus, may affect the island density measured by AFM. Finally, we emphasize that at the moment few studies are published, which quantitatively compare GISAXS and AFM data for small organic molecules at a comparable level of detail.

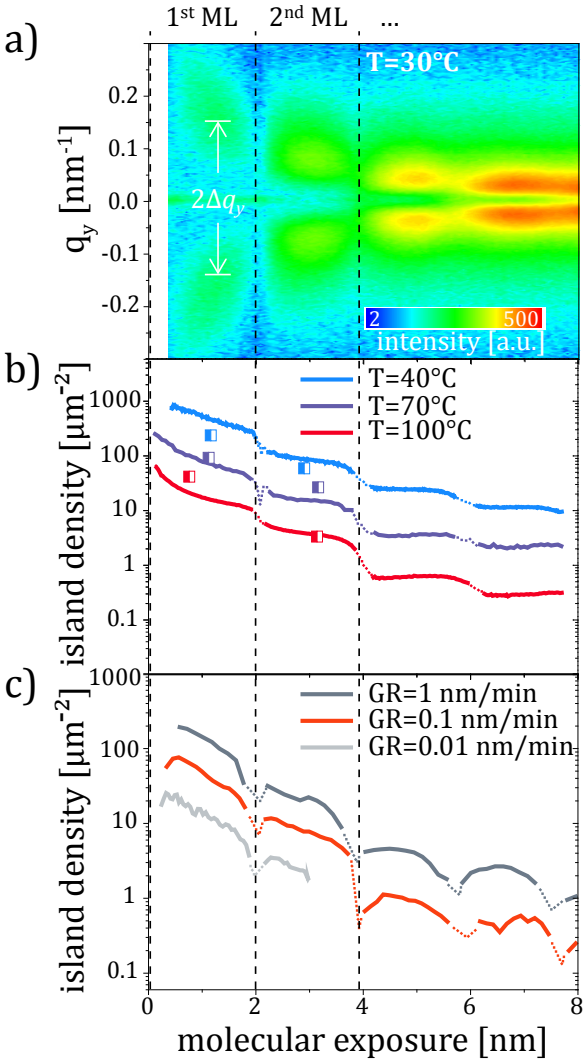

Figure 4.6: a) Time evolution of the diffuse scattering (GISAXS) during the PTCDI−C_8 growth (T=30 °C, GR=0.1 nm/min). Two separate peaks, whose intensity oscillates with a period of 1 ML, are observed. The peak spacing is related to the mean island distance L via $L = 2\pi/\Delta q_y$ and, therefore, to the island density. From GISAXS datasets similar to a), the evolution of the island density for b) different temperatures and c) growth rates is obtained. The half-filled squares in b) correspond to island densities obtained from FFT transformed AFM images as discussed in the text.

4.1.6 Quantification of nanoscale processes governing the nucleation.

We will now analyze the obtained experimental results on the growth of the first MLs of PTCDI−C_8 in the framework of mean field nucleation theory, which will allow us to determine important quantities like the nucleation energy and the critical nucleus size. In section 2.1.1 we briefly introduced the concept of mean-field nucleation theory. A central result is a power-law for the island density in the steady-state regime. Thus, the island density is at its maximum, which we denoted as N_{max}. In agreement with the arguments given in section 2.1.1 and in accordance with ref. [22] we can formulate a dependency of N_{max} on the growth rate GR and the substrate temperature T:

$$N_{\max} = \eta \cdot N_0 \cdot \left(\frac{4 \cdot GR}{N_0 \cdot \nu_0}\right)^p \cdot \exp\left(\frac{E_{nuc}}{kT}\right). \tag{4.1}$$

The exponent p is a function of the critical nucleus size i, which is defined as the number of monomers required to form the largest non-stable cluster. Islands containing i+1 monomers are hence more likely to stay stable than to decay. The nucleation energy E_{nuc} contains a dependency on i as well as on various energy barriers for different molecular processes. The pre-factor η is a weakly varying function of the coverage and i being typically 0.2-0.3,[11] while ν_0 is the attempt frequency. The number of surface sites per unit area, N_0, equals $2.27 \cdot 10^{14}$ molecules/cm^2 in the PTCDI−C_8 [001] plane based on the thin film unit cell parameters determined by Krauss *et al.*[119] Various publications have implemented equation (4.1) to describe nucleation and growth of both organic and inorganic materials.[22–24,132]

To evaluate and compare p and E_{nuc} in both MLs we plot the logarithm of the maximum island density as obtained from GISAXS in a $\ln(N_{max})$ vs. $\ln(GR)$ and a $\ln(N_{max})$ vs. $1/kT$ plot as shown in Figs. 4.7 a) and b). According to equation (4.1) we expect a linear relationship in each case with the slopes being p and E_{nuc}, respectively. Note, that we use the effective growth rates of the 1st and 2nd ML as deduced from the anti-Bragg fits for the plot of Fig. 4.7 b), so that we correct for the slower growth in the 1st ML. As demonstrated, we obtain the predicted linear relation for the nucleation of 1st and 2nd PTCDI−C_8 ML, which points towards homogenous nucleation for both MLs. The fits yield values of E_{nuc1}=532±52 meV and p_1=0.50±0.05 for the 1st ML and E_{nuc2}=460±28 meV and p_2=0.53±0.05 for the 2nd ML. Importantly, we find that the nucleation energy E_{nuc} is about 70 meV smaller in the 2nd ML while the parameter p is essentially identical within the error bars

in both MLs. We will use these finding later to discuss the diffusivity of the molecules.

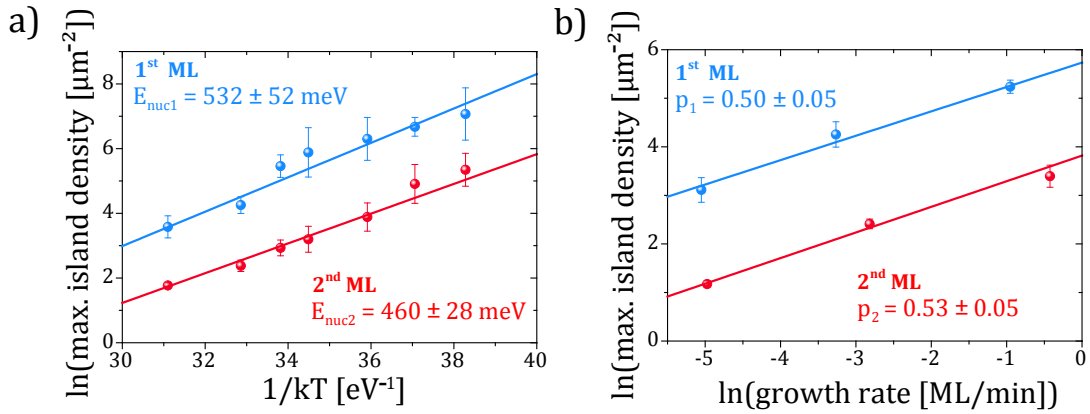

Figure 4.7: a) Determination of the nucleation energy in the 1st and 2nd ML on the basis of the maximum island densities obtained from GISAXS data. A decrease of the nucleation energy is observed in the 2nd ML. b) Illustration of the linear behavior of the logarithm of the maximum island density as obtained by GISAXS in the 1st and 2nd ML under a variation of the effective ML growth rate (as obtained from the anti-Bragg fits). The slope p, which is related to the critical nucleus size, essentially does not change within the first two MLs.

Additionally to E_{nuc} and p we can also determine the attempt frequency ν_0 from the linear fits shown in Figs. 4.7 a) and b). To do so, we evaluate the intersections of the linear curves with the y-axis, which are given as:

$$y_{0R} = \ln(\eta \cdot N_0) + p \cdot \ln\left(\frac{4}{N_0 \cdot \nu_0}\right) + E_{nuc} \cdot \frac{1}{kT} \tag{4.2}$$

$$y_{0T} = \ln(\eta \cdot N_0) + p \cdot \ln\left(\frac{4}{N_0 \cdot \nu_0}\right) + p \cdot \ln(GR), \tag{4.3}$$

with y_{0R} and y_{0T} being the intercepts of the linear fits in the $\ln(N_{max})$ vs. $\ln(GR)$ and $\ln(N_{max})$ vs. $1/kT$ plots respectively. By inserting p and E_{nuc} we calculate the attempt frequency ν_0 in both MLs, since all the other quantities are known. Importantly, essentially the same frequencies are deduced from the fits to the temperature and rate variation, which proves the consistency of the model and the data. We derive attempt frequencies of $\nu_{0,1} \approx 10^{20\pm3}\,\mathrm{s}^{-1}$ in the 1st ML and $\nu_{0,1} \approx 10^{19\pm3}\,\mathrm{s}^{-1}$ in the 2nd ML. Note, that small changes in p induce comparatively large changes in ν_0. Thus, within the errors introduced by the uncertainty in p, $\nu_{0,1}$ and $\nu_{0,2}$ may assumed to be equal. It is noteworthy, for atomic systems typical attempt frequencies in the range of $10^{13}\,\mathrm{s}^{-1}$ are reported. For small organic molecules, however, few published

data is available. In one study an attempt frequency of $10^{17}\,s^{-1}$ has been found for the organic molecule sexiphenyl on amorphous mica.[22] As reported in ref. [22], due to the increased number of rotational and vibrational modes that can be excited in organic molecules in comparison to atomic systems, larger attempt frequencies are expected. Our findings clearly confirm this trend.

4.1.6.1 Differences of 1st and 2nd ML nucleation discussed beyond the DLA model

In what follows we will compare the PTCDI−C_8 nucleation in the 1st and 2nd ML in order to rationalize the observed decrease of the island density in the 2nd ML by quantifying the differences in the molecular diffusivity. For this purpose we will combine the evaluated values of p, E_{nuc} and ν_0 of both MLs. Depending on the examined parameter space of T and GR different energetic barriers may govern the nucleation, so that various nucleation regimes can be formulated, which is summarized in Fig. 4.8 b).

A fundamental difference between the regimes is, whether they describe complete or incomplete condensation. If a significant fraction of already adsorbed molecules desorbs from the surface before attaching to a cluster, the condensation is regarded as incomplete. Such behavior was e.g. observed by Ribic *et al.*[23] for pentacene films grown on polymeric substrates at substrate temperatures above 50 °C. The authors observed a shrinking monolayer growth rate by approximately 35 % per 10 °C increase in the substrate temperature and applied the initially incomplete condensation (IIC) model for fitting. In contrast, in the case of PTCDI−C_8 the fits of the anti-Bragg growth oscillations show the same effective GR for the growth at 40 °C and 100 °C. Thus, we conclude that molecular desorption is not the dominating process in the investigated parameter range and the condensation can be regarded as complete. Crucially, complete condensation does not imply that every incoming molecule will actually be adsorbed and will stick to the surface. Different sticking coefficients (in contrast to different desorption rates) may thus explain our finding of different effective 1st and 2nd ML growth rates.

For the case of complete condensation the most frequently used nucleation regime is diffusion limited aggregation (DLA) with $p = i/(i-2)$ and $E_{nuc} = (iE_d + E_i)/(i+2)$. The binding energy of a critical nucleus E_i is included in E_{nuc}. However, since in complete condensation a detachment of already adsorbed molecules from the surface is zero or insignificant, the nucleation energy does not depend on the desorption

energy E_a, but on the energy barrier for diffusion E_d.

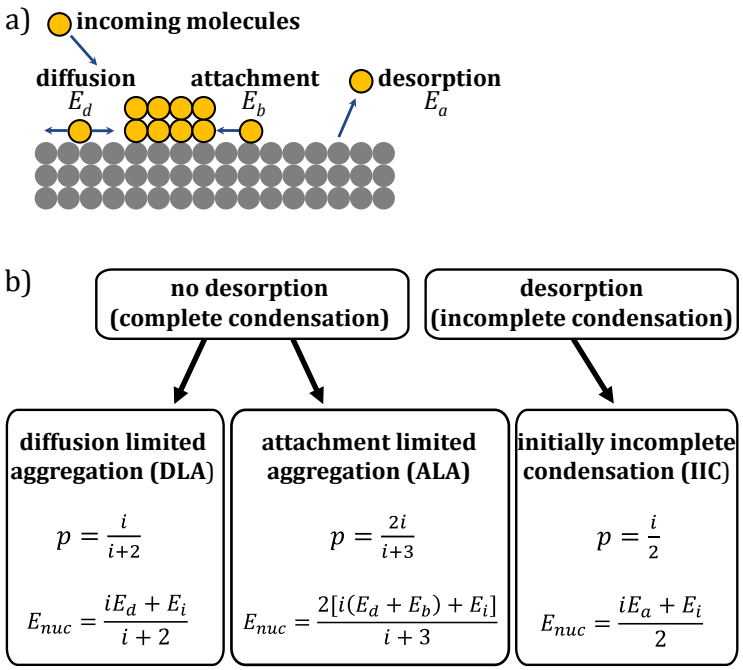

Figure 4.8: a) Illustration of relevant molecular processes and energy barriers involved in organic thin film growth. b) Summary of the exponents p and E_{nuc} from equation (4.1) as defined for two different nucleation regimes. Depending on the particular regime, diffusion energy E_d, binding energy of a critical nucleus E_i, and desorption energy E_a can contribute to the effective nucleation energy E_{nuc}. The scaling exponent p is always a function of the critical nucleus size i.

By applying DLA and using the determined quantities of p and E_{nuc}, we can evaluate the critical nucleus size and discuss the evolution of the energy barrier for surface diffusion E_d in the 1st and 2nd ML. As shown in Fig. 4.7 b), the exponential factor p is similar in both MLs. According to the definition of p in the DLA regime, this implies that the critical nucleus size also has to be equal in both MLs and it has to be i=2 if inserting the values of p_1 and p_2. To our knowledge no data on the size of critical PTCDI−C_8 clusters is available in literature. Looking at the critical cluster sizes of other rod-like molecules, values of i=2-3 for *para*-sexiphenyl,[22,133] i=5±2 for pentacene[31,33,134,135] and i=2 of diindenoperylene[33] have been published. Interestingly, for the related, but heavier PTCDI−C_{13} molecule grown on various organic self-assembled monolayers, a cluster size of i=1 was reported recently.[25] We note, however, that i is also known to depend on exact growth parameters such as the substrate temperature.[27,136]

Further, to evaluate E_d we use the definition of $E_{nuc} = (iE_d + E_i)/(i+2)$ as given in the DLA model and insert this in the relation E_{nuc1}-E_{nuc2}=70 meV as determined from Fig. 4.7 a). Since the critical nucleus size is identical (i=2), the binding energy of the critical nucleus E_i has also to be equal $E_{i,1}$=$E_{i,2}$=E_i in both MLs. Combining this, we find:

$$E_{d1} - E_{d2} = 140\,\text{meV}. \tag{4.4}$$

The result of equation (4.4) is that the energetic barrier for diffusion in the 2nd ML is 140 meV lower. This may indicate a higher diffusivity D in the 2nd ML, but according to the definition of $D = \nu_0 \cdot \exp(-E_d/kT)$ the attempt frequency also plays an important role. A decreased attempt frequency in the 2nd ML may outbalance the effect of a decreased diffusion barrier. This is, however, not the case for PTCDI−C_8. Although we found a slightly decreased ν_0 in the 2nd ML ($\nu_{0,2} = 0.1 \cdot \nu_{0,1}$), comparing the diffusivities in both MLs, there is still an increased molecular mobility in the 2nd ML accounting for the decreased island density in the evaluated T range:

$$D_2 = D_1 \cdot \left[\frac{\nu_{0,2}}{\nu_{0,1}} \cdot \exp\left(\frac{-(E_{d2} - E_{d1})}{kT}\right)\right] \approx (25...250) \cdot D_1|_{T=293\text{K}}. \tag{4.5}$$

Assuming $\nu_{0,1} \approx 10^{20}\,\text{s}^{-1}$ and $\nu_{0,2} \approx 10^{19}\,\text{s}^{-1}$ we find a 25 times larger diffusivity in the 2nd ML, while the assumption of the same ν_0 in both MLs yields a 250 times increased diffusivity at room temperature. In literature decreased island densities in the 2nd ML have been reported e.g. for diindenoperylene on silicon oxide.[83] The study also found a decrease of E_{nuc} in the 2nd ML of 100 meV, which is comparable in size with the present case of PTCDI−C_8. However, neither E_d and ν_0, nor the diffusivity have been evaluated directly. The effect of a decreasing diffusion barrier and decreasing island densities in higher MLs has however been found for the case of inorganic Co films grown of Fe(001).[30]

While in the past most nucleation studies of organic molecules have been relying on the DLA model, over the last years this model has been refined by taking additional and new effects into account, in particular so-called attachment barriers[47] (ALA regime) and hot precursor states.[48,137] Contrary to DLA, in the case of the ALA regime the probability of a molecule to attach to a molecular island is different than unity and the molecule has to overcome the attachment barrier energy E_b. E_b can be regarded as the energy needed to reorient the molecule from the flat lying state when

freely diffusing to an almost upright standing state when attaching to an island.[29,47] In the case of ALA, E_b enters E_{nuc} and furthermore the definition of p changes as summarized in Fig. 4.8 b). Applying ALA in both MLs for the case of PTCDI−C_8, we find a critical nucleus size of i=1, since $p_1 \approx p_2 \approx 0.5$. Additionally, we can use the ALA definition of E_{nuc} and E_{nuc1}-E_{nuc2}=70 meV from Fig. 4.7 a) in order to arrive at the following equation:

$$(E_{d1} + E_{b1}) - (E_{d2} + E_{b2}) = 140\,\text{meV}. \tag{4.6}$$

Since the nucleation is homogeneous, the attachment barrier E_b originates from a direct in-plane interaction of the organic molecules. Consequently, we can expect a small dependence of E_b on the underlying layer. As a result of this assumption $E_{b1} \approx E_{b2}$, and equation (4.6) transforms into equation (4.4), with the same consequences concerning the increased molecular diffusivity in the 2nd ML.

A third model that has recently been applied in the context of organic nucleation, includes so-called hot precursor states.[48,137] Commonly, hot molecules from the crucible, which impinge on a surface, are assumed to transfer their whole kinetic energy to the substrate material and adopt its temperature. However, if this thermalization process is slow, individual molecules may still possess some additional, remaining kinetic energy, resulting in a higher diffusivity than expected for a given substrate temperature. The effective temperature T_{eff} of the molecules can then be denoted as $T_{eff} = T_i - \kappa \cdot (T_i - T_s)$, with T_i being the temperature of evaporation, T_s the substrate temperature and κ the so-called energy dissipation coefficient. According to reference[48] in the case of hot precursor states the maximum island density can be described as follows:

$$N_{\max} = 10^{-8} \cdot N_0 \cdot \left(\frac{4 \cdot GR}{N_0 \cdot \nu_0}\right)^p \cdot \exp\left(\frac{E_{nuc}}{k \cdot (T_i - \kappa \cdot (T_i - T_s))}\right). \tag{4.7}$$

As given by the ALA model $p = 2i/(i+3)$ and $E_{nuc} = 2[i(E_d + E_b) + E_i]/(i+3)$. Equation (4.7) can in principle be applied to fit the datasets of $\ln(N_{max})$ vs T_s and $\ln(N_{max})$ vs $\ln(GR)$, although the fit is clearly overparametrized with ν_0, E_{nuc} and κ being unknown (the exponent p is still the slope in the $\ln(N_{max})$ vs $\ln(GR)$ plot in equivalence to the DLA/ALA model). However, we can investigate E_{nuc} and κ in both MLs by probing various ν_0.

The fits for the 1st ML are shown in Fig. 4.9 a), b), while in c) and d) data for

the 2nd ML is presented. Assuming perfect consistency of the $\ln(N_{max})$ vs. $1/T_s$ and vs. $\ln(GR)$ datasets, the same fit parameters have to result in good fits of both datasets. Since different batches of silicon oxide substrates have been used for the temperature and rate variation experiments, the fit in Fig. 4.9 b) slightly deviates. In contrast, in the 2nd ML, where differences of the silicon oxide substrate do not play a role, perfect fits are achieved for both datasets.

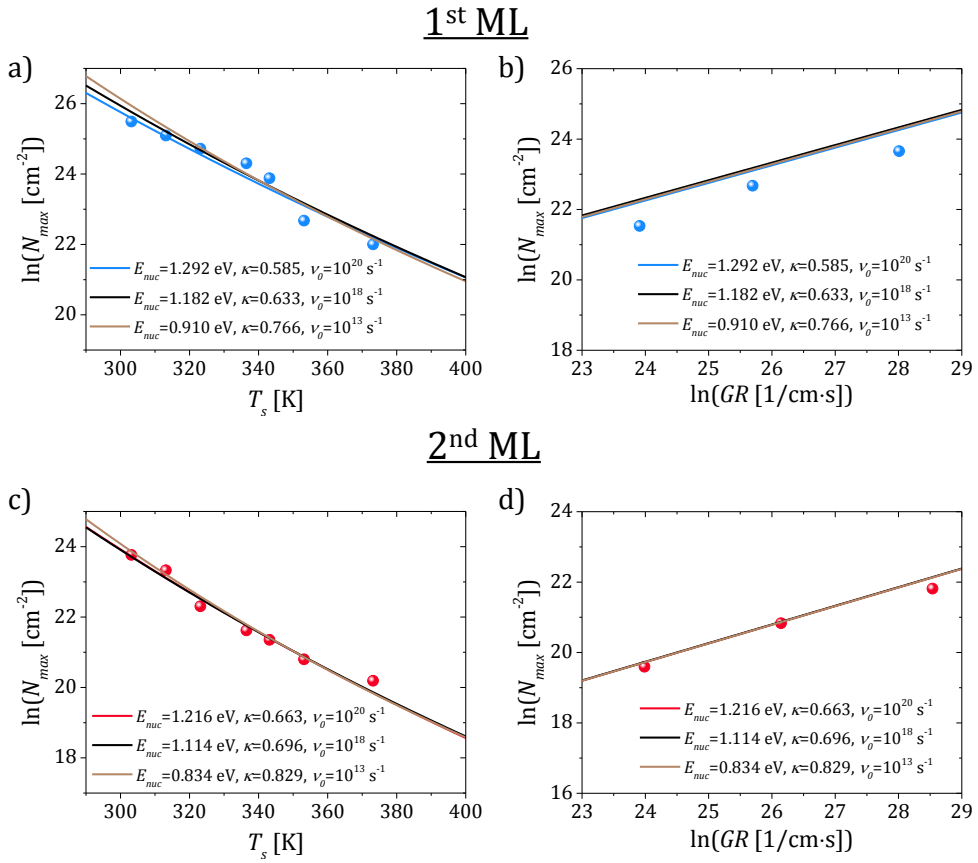

Figure 4.9: a) and b) Fits of the hot-precursor model to the scaling of the maximum island density N_{max} in the 1st PTCDI−C_8 monolayer. c) and d) Fits of the same model to the scaling of N_{max} in the 2nd ML. Independent of the assumed attempt frequency ν_0, the fits yield higher values of E_{nuc} and the energy dissipation factor κ in the 2nd ML as compared to the 1st ML.

We note that the fits are overparametrized, which inhibits a distinct fit of the energy dissipation coefficient or the nucleation energy. Nevertheless, we observe the following trend, independent of ν_0. The fits show a decreasing E_{nuc} by about 70-80 meV in the 2nd ML and a slightly higher energy dissipation coefficient. While the first result is in accordance with the DLA/ALA evaluation (see above), the latter is an interesting phenomenon. A higher κ points towards a decreased effective

temperature of the molecules in the higher ML, in which the impinging molecules hit material of the same mass. The soft organic monolayer absorbs more of the initial kinetic energy than the hard silicon surface. The difference in the energy dissipation may hence also influence the nucleation and growth behavior in different MLs, which is a new and yet largely unstudied phenomenon.

4.1.7 Summary

We have examined the ML-dependent nucleation and growth of the organic semiconductor PTCDI−C_8 deposited on silicon oxide substrates. For our study we combined *ex situ* AFM and *in situ* real-time X-ray scattering, where we simultaneously monitored the temporal evolution of the in-plane (GISAXS) and the out-of-plane (XRR) thin film morphology in individual MLs beyond submonolayer nucleation.

We identified important differences in the nucleation and growth behavior of the 1st and the subsequent MLs of PTCDI−C_8, such as a transformation of the island shapes, as well as an increase of the molecular adsorption probabilities. Of particular interest is the observed decrease of the molecular island density in higher layers. Such a trend indicates an enhancement of the molecular diffusivity. To verify this, we examined the scaling of the maximum island densities N_{max} in each individual ML as a function of the substrate temperature and the growth rate. We fitted the observed N_{max} scaling by applying the classical diffusion-limited aggregation (DLA) as well as more recent models such as attachment-limited aggregation (ALA) within the mean-field nucleation theory. From the models we determined the same critical nucleus size i in both MLs (i=2 in DLA and i=1 in ALA) and a slight decrease of the attempt frequency ν_0 from 10^{20} to $10^{19}\,s^{-1}$. Furthermore we determined a 70 meV decrease of the nucleation energy E_{nuc} in the 2nd ML. Combining the data, we evaluated a significant decrease of 140 meV of the energy barrier for diffusion E_d, which correlates with an at least 25 times larger molecular diffusivity in the 2nd ML at room temperature. This finding explains the observation of a decreased island density in upper MLs. Applying a hot precursor model hints additionally at a different thermalization in the 2nd ML as compared to the 1st ML.

Compared to inorganic material systems, the nucleation and growth of organic molecules is more intricate due to the complexity of the molecular shapes that influence the self-assembly. One of the most challenging tasks remains the determination of energetic barriers and nanoscale processes like molecular diffusion. Our approach of expanding the analysis of organic semiconductor nucleation beyond the first (sub-)

monolayer regime to subsequent MLs allows us to identify and quantify important changes of structure defining processes as demanded for an enhanced comprehension of the thin film formation.

5 Results: Controlling the growth-mode of organic semiconductors via chemical tuning

In the previous chapter we discussed the results of mainly X-ray scattering experiments leading to an enhancement of the understanding of nucleation and growth of small organic semiconductors. As a next step, we explore strategies to rationally manipulate the growth processes. This will be the topic of the present chapter, where we will present and discuss in detail the impact of chemical tuning on the growth-mode of *para*-sexiphenyl molecules. This chapter is organized as follows: first, we will briefly introduce one of the most studied and, thus, prototypical organic molecular semiconductors *para*-sexiphenyl and we will describe how we chemically tuned this molecule. We further discuss our experimental results on systematic growth manipulation by chemical tuning.

5.1 The organic semiconductor *para*-sexiphenyl (6P)

Para-sexiphenyl (6P), which is also known as *para*-hexaphenyl, belongs to the class of linear, rod-like oligophenyls, which are made up of conjugated phenyl rings connected by single bonds. As indicated by the name, 6P ($C_{36}H_{26}$) consists of six connected rings and is stable upon heating up to temperatures below 500 °C.[138] The chemical structure and a schematic sketch of 6P is given in Figs. 5.1 a) and b). The individual phenyl rings are not rigid chain links, but can rotate around the long symmetry axis of the molecule, which is called the long molecular axis. Calculations show that for isolated 6P molecules in vacuum a twisted conformation is energetically more favorable than the planar.[40] The van-der-Waals length of 6P is given as 2.72 nm.[139]

Over the last years, 6P has been subject of many growth studies on various surfaces such as mica[22,39,140], ZnO[20,141], Ti_2O[43,142,143], graphene[144], Cu[145] or

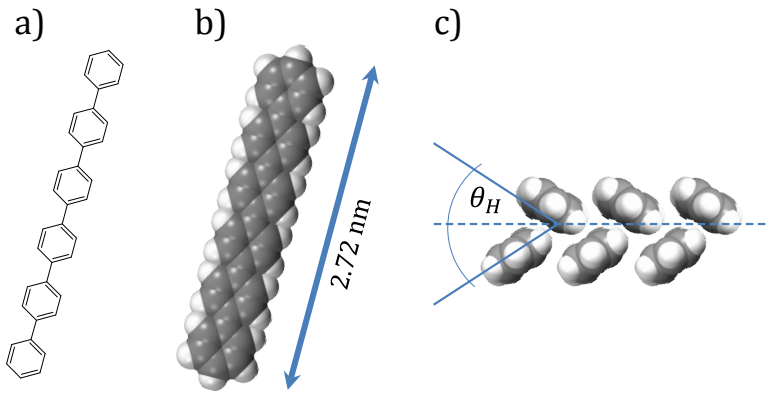

Figure 5.1: a) Chemical structure of *para*-sexiphenyl (6P). b) Sketch of the 6P molecule with the approximate van-der-Waals dimensions. c) Top-view of the herringbone packing of 6P molecules in a crystal with the herringbone angle θ_H=66 °.

silicon oxide[132,133]. One of the reasons for this extensive research activity is the strong blue fluorescence emission, which makes 6P an interesting candidate for the application as an active layer material in organic LED's or lasers.[146–153] Additionally, 6P films are stable under ambient conditions, which is also important for applications. Furthermore, the possibility to grow 6P films with large grain sizes has a beneficial effect on the performance of organic thin film transistors, due to the improved charge carrier mobility.[154]

When forming well-organized, crystalline films, 6P arranges in a herringbone structure as displayed in Fig. 5.1 c) as confirmed by experiment and simulations.[155,156] This packing motif is a common feature for rod-like molecules[157] and has indeed been found for such molecules like e.g. diindenoperylene,[158] pentacene,[159] or α-sexithiophene.[160] As recent calculations confirmed, in the case of 6P, the quadrupole moments, present in every single 6P molecule, play a key role in the formation of the herringbone arrangement, with a herringbone angle of θ_H=66 °.[161] Focusing on crystallization, it is important to mention the 6P bulk crystal phase, which is known as the β- or Baker-phase.[155] Apart from the herringbone packing, this phase is characterized by two molecules in a monoclinic unit cell. Furthermore, within the crystals, the long molecular axes of 6P molecules are arranged in parallel and exhibit a tilt angle of 17 ° with regard to the layer normal. Although initially discovered in single crystals experiments, the β-phase is also found in thin films of 6P, as demonstrated e.g. in ref. [162]. However, as later studies revealed, when growing 6P thin films on silicon substrates at elevated substrate temperatures of $T \geq 160$ °C the γ-phase appears.[139] While being very similar, the most striking difference of

Table 5.1: Unit cell parameters of two 6P polymorphs as taken from ref. [139].

	a [nm]	b [nm]	c [nm]	α [°]	β [°]	γ [°]
6P β-phase	0.809	0.557	2.624	90	98.2	90
6P γ-phase	0.798	0.553	2.764	90	99.8	90

the γ-phase is the decreased tilt angle of the 6P molecules with respect to the layer normal. In fact, the molecules arrange perpendicular, i.e. the tilt angle equals 0 ° instead of 17 ° in the β-phase. A complete set of the unit cell parameters of the 6P polymorphs is given in table 5.1.

5.2 Chemical tuning

A purposeful manipulation of growth processes would enable us to design structures with a desired morphology as demanded and optimized for specific opto-electronic devices. In reality, however, growth is a complex process with manifold interactions, energetic pathways and degrees of freedom. A predictive manipulation is thus difficult. When discussing the study of PTCDI$-C_8$ growth in the last chapter, we already presented the classical and probably most direct and facile way to control growth by varying the substrate temperature and growth rate. In a wider sense, using different substrates can also be regarded as a method to control growth. Molecules are known to self-assemble differently on different substrates, as exemplarily shown for pentacene films or oligo-thiophenes and oligo-phenylenes.[163–165] The disadvantage of this approach is that it is not always feasible to use a different substrate for a specific application. A loophole would be to use a different crystal surface of one and the same material, which has been shown to significantly influence the growth mode of e.g. 6P, diindenoperylene and PTCDA (3,4,9,10-perylene-tetracarboxylic-dianhydride).[20,166–169] In particular, for ionic crystals one can utilize the different electrostatics the surfaces to impact the growth. Exemplarily, for the ZnO (10**1**0) surface, which consists of parallel Zn and O rows of opposite charge, it has been shown that the electrostatic field influences the orientational ordering and the diffusion of 6P molecules.[161,170,171] Further, a pre-treatment of the substrate, e.g., via sputtering can be used as an approach to steer the growth. The resulting increased substrate roughness and the loss of the substrate symmetries were shown to have an effect on the molecular self-assembly.[21,172,173] An interesting and yet rather unexplored approach for growth control consists in exposing the growing molecular film to light of a resonant frequency. As a result of the molecule-light interaction the crystal phase purity of sexithiophene films has been enhanced.[9]

Within this thesis we have chosen to study chemical tuning as a growth-control mechanism. This approach makes use of the chemical flexibility of the organic semiconductors, which enables us to substitute functional groups or just single atoms. In a wider sense, the attachment of alkyl chains of different lengths to PTCDI molecules, which we discussed in the last chapter, can be regarded as an example of this process. Another example would be the chemical tuning of the phthalocyanines (PC), where chemical tuning is used to attach different substitutions like e.g. copper, tin, chloraluminum, chlorogallium, vanadyl, lead and others to the PC core molecule.[174–178] In contrast to PTCDI and 6P, the PC derivatives are often non-planar molecules, where the different substitutes represent the "head" of the otherwise planar PC. Amongst other features, the substitutes induce different dipole moments in the molecule. Growing such molecules on a substrate can be used to induce a tunable work function shift of the molecule-substrate system.[179–181] Focusing on the growth process, studies revealed an influence of chemical tuning of PC on the molecular orientation and the intermixing behavior of head-up/head-down configurations.[177,182]

Chemical tuning plays also a role for pentacene-based molecules. An example are pentacene quinones.[183–185] Miao *et al.* have fabricated organic field effect transistors on its basis. They demonstrated that the chemical tuning of pentacene towards pentacene quinone has an effect on the molecular stacking, which they found to be unusually dense for the quinone crystals. Up to now, pentacene quinones stay in the focus of research and are exploited e.g. as sensors or as catalysts for hydrogen production.[186–188] Another important representative of chemically tuned pentacene is perfluoropentacene, where all hydrogen atoms of the pentacene are substituted by fluorine atoms.[189] While the dimensions of the molecule itself and also of its unit cell remain essentially unchanged, the chemical manipulation converts the p-type pentacene into an n-type material.[190] This in turn opens promising perspectives for the application of bipolar pentacene-perfluoropentacene blends, with the individual parts playing the respective donor and acceptor role.[191] Studies have investigated the growth behavior of the chemically tuned perfluoropentacene.[192–195] Interestingly, in the case of perfluoropentacene growth on oxidized silicon wafers a non desired film roughening was observed, which sets in faster when compared with unsubstituted pentacene films.[196]

The above examples demonstrate that chemical tuning can influence various properties of the thin film and, in particular, the molecular self-assembly. Important questions are: which substitutes will affect the growth? How many of these substi-

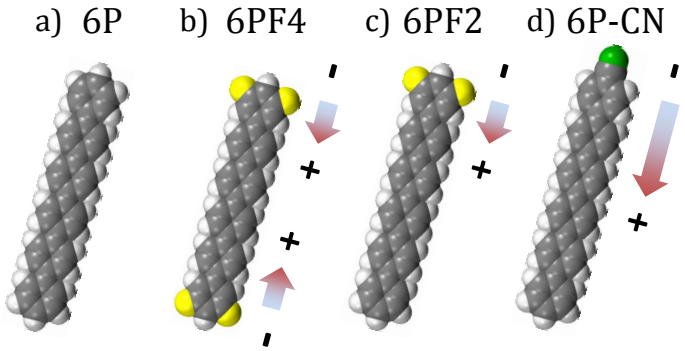

Figure 5.2: Sketches of the structure of a) 6P and its synthesized, chemically tuned derivatives with four and respectively two hydrogen atoms exchanged by fluorine, b) 6PF4 and c) 6PF2. Further, one hydrogen atom at the terminus of 6P was substituted by a cyano group, d) 6P-CN. The arrows are meant to visualize and compare the strength and orientation of the local dipole moments induced by the substitutions but must not reflect the exact relationships.

tutes are needed to induce changes in the process of self-assembly? What kind of changes can be induced?

In the following we will tackle these and other questions on the example of the chemical tuning of 6P. Yves Garmshausen from the HechtLab at the chemistry department of the Humboldt university developed a synthesis route, which enables to interchange singular 6P hydrogen atoms at different positions by fluorine atoms.[197] In doing so, one not only changes the chemical environment, but also induces local dipole moments. Further, the substitution can break the symmetry of a molecule, if applied just at one terminus of the molecule, as in the case of 6PF2, see Fig. 5.2 c). The effect of this manipulation on the self-assembly can then be compared to the symmetrically tuned counterpart 6PF4 with two fluorine atoms at each terminus, see Fig. 5.2 b). Further, when going beyond fluorination, one can also investigate the effect of the strength of the local molecular dipole moment on the growth, if tuning 6P with, e.g., the cyano group (6PCN). In Figs. 5.2 b)-d) sketches of the synthesized molecules on the basis of 6P are displayed.

The brief synthesis route of 6PF4 can be found in the supplemental material of ref. [104], while a more detailed overview on the synthesis of dipolar 6P derivatives is given in ref. [197]. An important aspect of the fluorinated 6P derivatives is that in this case the chemical tuning does not affect the molecular functionality. The relevant optical properties of 6P are kept virtually unchanged. We demonstrate this by comparing the excitation and fluorescence spectra of 6PF4 and 6P in Fig. 5.3,

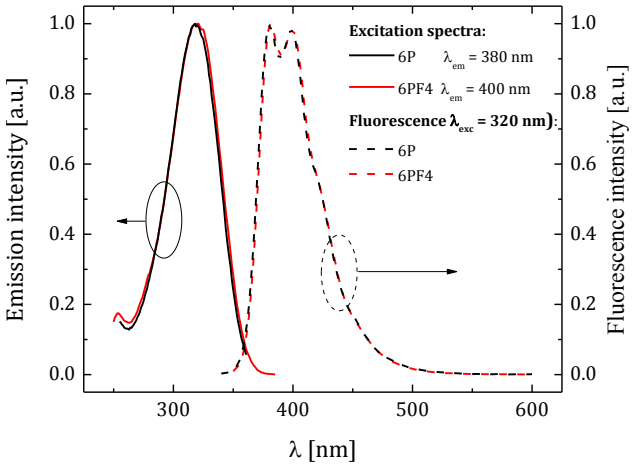

Figure 5.3: Excitation (solid line) and corresponding fluorescence (dashed line) spectra of 6P and 6PF4 in $CHCl_3$ at 25 °C with the spectra normalized to 1. The agreement of the spectra proofs the unchanged optical properties of the fluorinated 6P derivative.

which nearly perfectly agree. Consequently, fluorinated derivatives could become excellent alternatives to the unsubstituted 6P in light emitting applications.

5.3 Symmetrical fluorination of *para*-sexiphenyl to induce film smoothing and crystal phase purification

In the following study, we compare the growth of the organic semiconductor *para*-sexiphenyl (6P, $C_{36}H_{26}$) with its symmetrically fluorinated derivative 6PF4 ($C_{36}H_{22}F_4$) (Fig. 5.4) by applying *in situ* X-ray reflectivity (XRR). We derive the structural properties of multilayer films and examine the real-time growth dynamics of both, 6P and 6PF4 on the non-polar (10**1**0) surface of ZnO. With regard to the molecular growth-mode, we demonstrate a significant effect of fluorination, which causes an alteration from a rough, three-dimensional growth, in the case of 6P, to comparatively smooth, two-dimensional layer-by-layer growth for 6PF4. Moreover, we show that fluorination suppresses the parallel growth of two different crystal phases, as observed for 6P films on ZnO, and enhances phase purity in the case of 6PF4 growth. Further, we observe a surface induced structure of 6PF4, which manifests itself in a change of the molecular orientation from more upright to more inclined in upper monolayers. As has been shown in ref. [39], a larger molecular tilt angle is correlated with a smaller energy barrier for step-down motion (Ehrlich-Schwoebel barrier), and therefore enhances the interlayer transport and decreases film roughening.

The present study was published in ref. [104] and was performed in close cooperation with M. Sparenberg, S. Blumstengel and F. Henneberger, who contributed an *in situ* AFM analysis of the 6P and 6PF4 growth, which will not be in the focus here.

5.3.1 Experimental procedures

6P and 6PF4 molecules were deposited via organic molecular beam deposition (OMBD) in a vacuum chamber at ultra-high vacuum conditions below $1.0 \cdot 10^{-9}$ mbar on ZnO (10**1**0) wafers (*CrysTec GmbH*, Germany). *Para*-sexiphenyl was obtained from TCI Deutschland GmbH. The deposition was performed at constant growth rates of approximately 0.1 nm/min and at room temperature. Details on the deposition and the pre-deposition cleaning procedure of the substrates are given in section 2.2.1 and 2.2.2, respectively.

All X-ray scattering experiments were performed at the ID03 beamline of the European Synchrotron Radiation Facility (ESRF Grenoble, France) at a wavelength of $\lambda = 0.1305$ nm. For details we refer to section 3.2.5.4. During the thin film growth

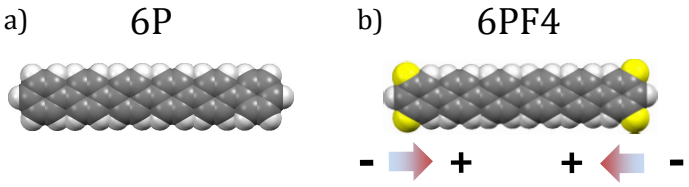

Figure 5.4: Sketch of a a) 6P and b) 6PF4 molecule.

the intensity of the specular reflected X-ray beam (XRR) was monitored in real-time in a reciprocal wave vector range from $q_z = 4\pi/\lambda \cdot \sin(\alpha_i) = 0.025\,\text{Å}^{-1}$ up to $q_z = 0.34\,\text{Å}^{-1}$ to investigate the evolution of the out-of-plane structure. The time per scan of <2 min enables sub-monolayer time-resolution as it is fast compared to the deposition time of ca. 26 min per ML at the chosen growth rate of ca. 0.1 nm/min. Complementary post-growth XRR measurements over a broad q_z-range, which commonly is referred to as $\theta/2\theta$-X-ray diffraction (XRD), were performed to study the out-of-plane structures of several ML thick films. All presented XRR and XRD data contain a geometrical footprint correction, as described in section 3.2.1.1, and the diffuse background scattering is subtracted to obtain the true specular reflectivity.

5.3.2 Crystal structure of post-growth films studied *in situ*

In Figs. 5.5 a) and b) we display XRD θ-2θ-scans yielding the out-of-plane structure of ≈18 nm or 7 ML thick 6P and 6PF4 films grown on ZnO (10$\bar{1}$0) substrates. In both measurements we observe (00l) Bragg reflections at least up to the 5th order. This indicates an almost upright standing orientation of the molecules and the high crystalline order of the 6P and 6PF4 thin films in the out-of-plane direction. We notice that in both cases the 1st and 2nd order Bragg reflections are less pronounced compared to the peaks assigned to higher orders. This can be rationalized by interferences between the comparatively strong ZnO substrate reflectivity and the molecular Bragg reflection, whose phase changes by π in the vicinity of the Bragg reflection. At higher q_z values, the substrate reflectivity decreases rapidly, so the molecular Bragg reflections become more pronounced. This allows us to determine a striking difference in the crystal structure of the films. For 6P films we observe a clear splitting of higher order Bragg reflections into two parts each corresponding to different average lattice spacings of $d_{6P,\beta}$=2.59 nm and $d_{6P,\gamma}$=2.72 nm. These can be correlated with the β- and γ-polymorphs of 6P.[139,155] The essentially equal intensities of the β- and γ-reflections suggest the simultaneous and parallel growth of both structures. Interestingly, this is different for 6P growth on glass structures, where the growth of the phases depends on the substrate temperature and exclusive β-phase growth

was found at room-temperature, while at T >160 °C the molecule exhibits exclusive γ-phase growth.[139] We gave the unit cell parameters of the polymorphs in table 5.1. One of the most prominent differences is the molecular tilt angle with respect to the surface normal, being 17 ° in the β-phase and 0 ° in the γ-phase.

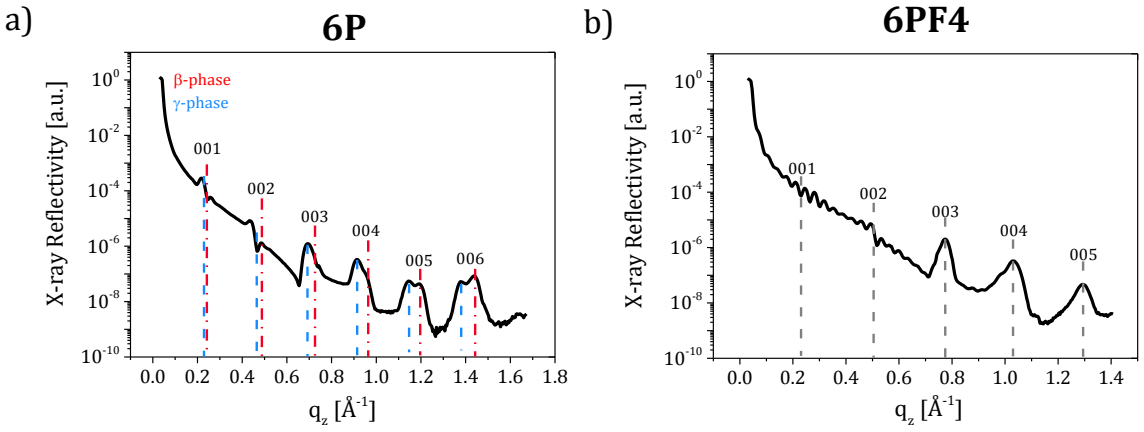

Figure 5.5: XRR scans of ≈18 nm or 7 ML-thick a) 6P and b) 6PF4 films show Bragg reflections at least up to the 7th order, which indicates high crystallinity. While we observe phase pure growth for 6PF4, films of 6P exhibit both β- and γ- phase Bragg reflections as indicated by the blue and red lines.

A different crystal structure is found for the fluorinated 6PF4. Here, we observe the growth of a singular phase with a corresponding average lattice spacing of 2.42±0.03 nm as derived from the q_z values of the Bragg reflections shown in Fig. 5.5 b). Note, we attribute the small shoulder apparent at higher order Bragg reflections to the surface induced phase, which we will discuss below. Still assuming a second phase growth for the sake of argument, we would find that the intensity of the Bragg reflection corresponding to this hypothetical second phase is significantly lower compared to the dominant first phase, as becomes evident from the inspection of the (005) Bragg reflection. Thus, our findings demonstrate that fluorination of 6P induces crystal-phase purity. By assuming an identical 6P and 6PF4 van-der-Waals length of 2.72 nm[139] (measured between the terminal H-atoms), we can estimate a tilt angle of 27 ° for the 6PF4 molecules. Thus, the molecular 6PF4 tilt is larger compared to that of 6P in either crystal phase. A further difference is the occurrence of almost undamped Laue oscillations around the 1st and 2nd order Bragg reflections of 6PF4. These oscillations are evidence of a laterally homogeneous coherent thickness, i.e., a well-defined number of ordered 6PF4 layers. 6P, on the other hand, does not show Laue oscillations indicating a rough surface.

5.3.3 *In situ* real-time X-ray investigations of the molecular growth mode

We now aim to analyze differences in the growth kinetics of 6P and 6PF4 films. Therefore, we performed real-time X-ray reflectivity (XRR) measurements as shown in Figs. 5.6 a) and b), which allow us to directly follow the structural evolution during a continuous growth run as a function of molecular exposure = exposure time × molecular flux. In contrast to common AFM experiments, which usually require growth interruptions, real-time measurements allow excluding effects like dewetting that might in principle not be observable by AFM. Real-time observation furthermore facilitates efficient data collection for both 6P and 6PF4 growth for several ML thick films. The q_z dependent reflectivity data in Figs. 5.6 a) and b) contain rich information about the growth mode. In particular, the layer thickness and layer coverage as well as the growth speed of each ML can be extracted.

In the range of q_z=0.2 Å^{-1} and 0.3 Å^{-1}, we observe the increasing intensity of the (001) Bragg reflection of 6P and 6PF4 with ongoing film growth. As discussed before, the intensity oscillations in the vicinity of the Bragg reflection are referred to as Laue oscillations and their damping in the case of 6P can be correlated to a rougher growth. For both molecules, we observe a shift of the (001) reflection to higher q_z values (corresponding to a lower lattice spacing d). This finding can be indicative of a surface induced phase. However, as mentioned before, interference effects at small q_z values also lead to changes in Bragg reflection shape and position. Therefore we analyzed higher order reflections, such as the (004) reflection shown in Fig. 5.7. The (004) Bragg reflection of 6PF4 is significantly stronger than the substrate reflectivity and is not distorted by interference effects. We observe the clear shift of the (004) reflection to larger q_z values. The corresponding decreasing lattice spacing d of 6PF4 can be correlated to stronger tilted molecules in higher layers. The determined lattice spacings are given in Fig. 5.7 and confirm a surface induced structure with 6PF4 molecules standing more upright in the first layers. Similar findings, i.e., a larger molecular tilt with increasing film thickness, have been reported for pentacene and diindenoperylene, dioctyl-terthiophene and sexithiophene.[79,198,199] For the parent, unsubstituted 6P molecule, the phase coexistence and interference with the substrate reflection make it impossible to infer details about a surface induced structure, since the shifting Bragg reflection is influenced by overlapping β- and γ-phase as well as substrate reflections. However, surface induced phases are also known for 6P. On ion-bombarded mica, for example, the molecules are more tilted at the interface,[39] which is the reverse trend compared to 6PF4.

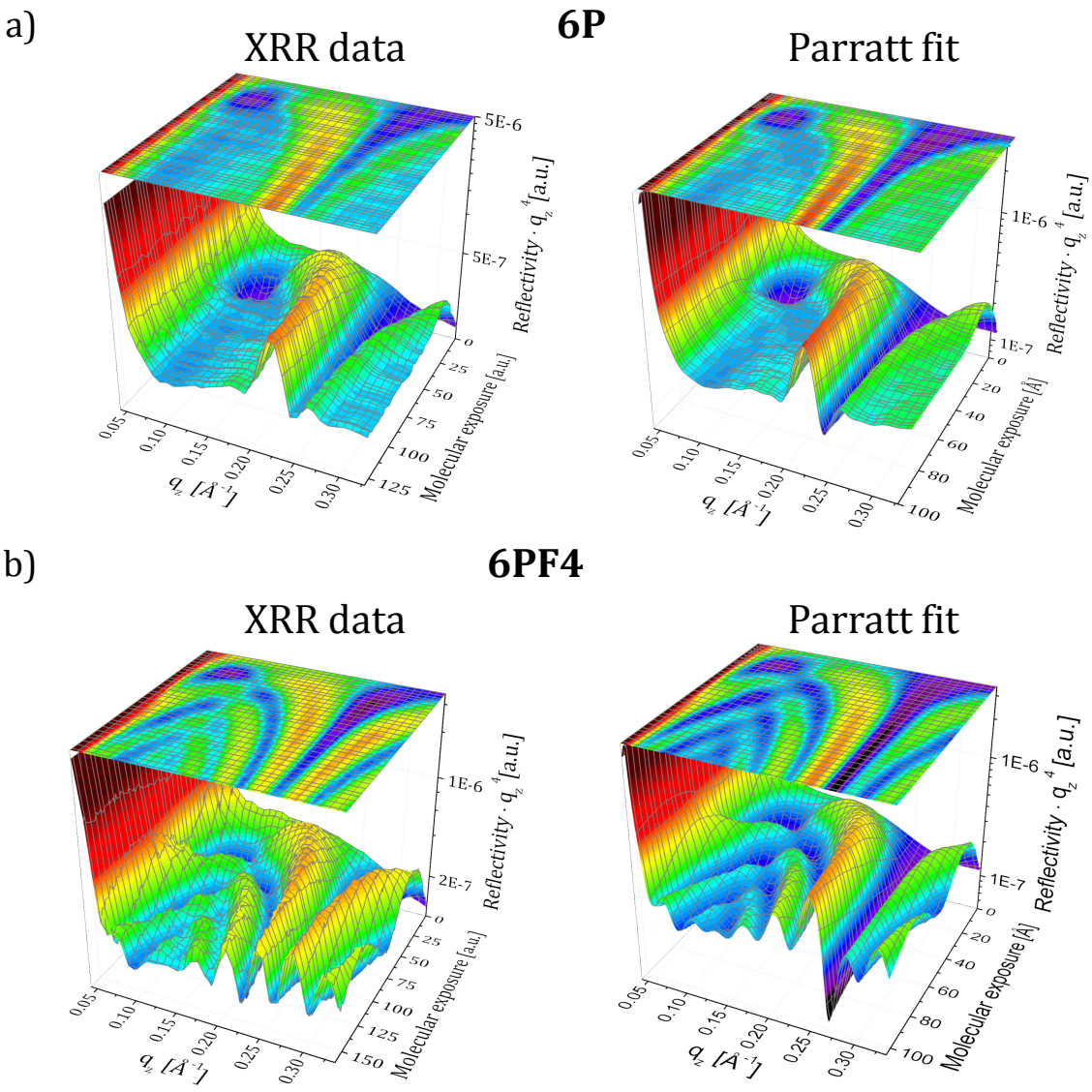

Figure 5.6: Evolution of the X-ray reflectivity (multiplied by q_z^4 for better visibility) during the growth of 6P and 6PF4 films on ZnO(10$\bar{1}$0). With increasing molecular exposure (i.e. rate × deposition time) the first order Bragg reflection gets more pronounced. During the growth of 6P we observe only weak Laue oscillations in the vicinity of the Bragg reflection. In contrast, 6PF4 exhibits nearly undamped oscillations, which is an indicator for its smoother growth-mode. On the right side of a) and b) the simulated morphology evolution based on Parratt fits of each individual XRR curve are shown. Comparing the data and the fits we conclude the very good agreement.

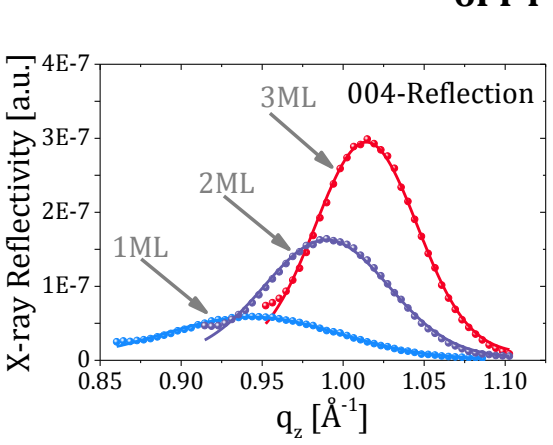

	d [nm]
1 ML	2.64 ± 0.12
2 ML	2.46 ± 0.06
3 ML	2.42 ± 0.03

Figure 5.7: Left side: (004) out-of-plane Bragg reflection for 6PF4 films for the first three MLs. A surface induced structure that differs from the bulk is responsible for the shifting reflection. Right side: surface induced changes in the lattice spacing d of 6PF4 for the 1st, 2nd and 3rd ML as deduced from (003), (004), and (005) Bragg reflections.

In the following we quantitatively analyze the 3d data in Fig. 5.6. To do so, we use two different methods. On the one hand, we take cuts through the 3d data at fixed times t, which yields XRR curves as introduced in detail in section 3.2.1. We apply the Parratt formalism[97] to fit the XRR curves and determine the electron density distribution of the films at each point in time. As an independent second method, we take cuts at fixed q_z values of $\frac{1}{2}$, $\frac{2}{3}$ and $\frac{3}{4}$ $\cdot\, q_{Bragg}$ and analyze the resulting, time-dependent growth oscillations. This method is frequently used in growth of inorganic[99,200–203] and organic materials[76–78,80], although often the analysis is restricted to oscillations at just one fixed q_z point instead of multiple q_z points as done here.

5.3.4 Morphology evolution studied from real-time XRR measurements and Parratt fits

Our first analysis uses the Parratt formalism[97] and results in good agreement with the experimental data as demonstrated in in Fig. 5.6. In the following we describe the approach, which at the end will allow us to evaluate the time evolution of the layer coverages. In the Parratt approach, the real-space structure at a fixed time during growth is divided into stratified layers, corresponding to the substrate and each molecular ML. For this layered structure, the X-ray reflectivity is then calculated

using the optical transfer matrix method with the thickness and the scattering length density (electron density × Thomson scattering length) of each layer as fit parameters. All fits have been performed with the software *Parratt32*, whose algorithm is based on the Parratt formalism.

Two exemplary XRR curves as acquired *in situ* during the growth of 6P and 6PF4 are shown with the corresponding best fits (red lines) in Fig. 5.8 a) and b). The scattering length density ρ_j of the ML j is a measure for the coverage of ML j. Hence, the temporal evolution of ρ_j allows us to investigate the temporal evolution of the layer coverages. Exemplary XRR curves are given in Fig. 5.8 for a) 6P and b) 6PF4 thin films. The scattering length density curves, corresponding to the red fit curves are given in Figs. 5.8 c) and d). We depicted XRR curves of a moment in time, where the scattering length densities (and therefore the coverages) of the 1st and 2nd ML of both films are essentially equal and the 2nd ML is almost closed.

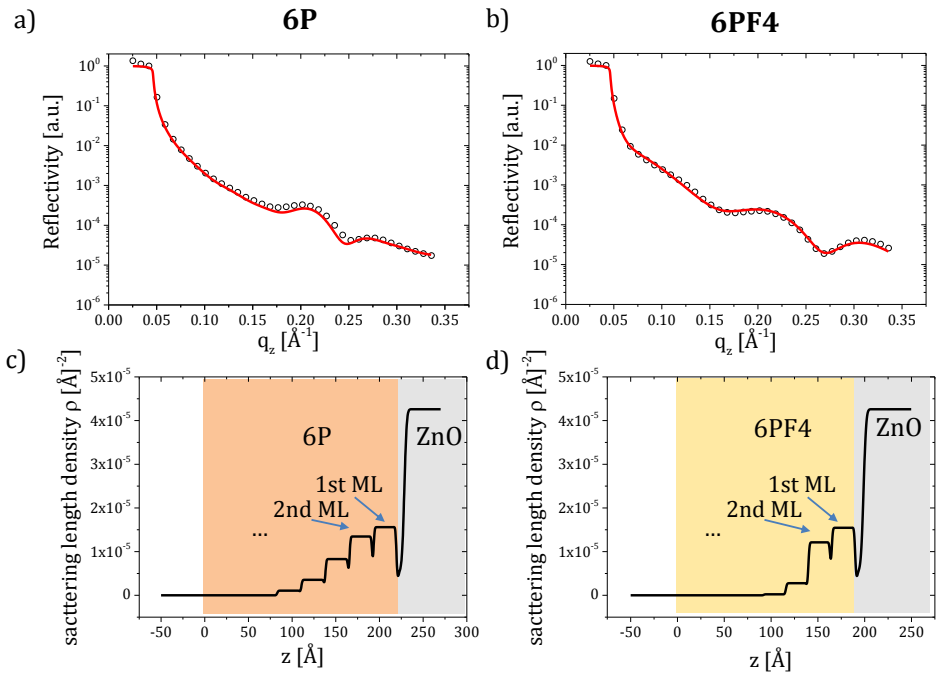

Figure 5.8: Comparison of 6P and 6PF4 films with similar coverages of the 1st and 2nd monolayer. XRR curves of a) 6P and b) 6PF4 films (dots) with the corresponding Parratt fits (red lines). Scattering length density curves of c) 6P and d) 6PF4. 6P films need to be grown much thicker than 6PF4 until the scattering length density (corresponding to the coverage) in the first two monolayers is the same. This implies that 6P grows much rougher and multiple layers grow before the second monolayer is filled.

We now compare for both molecular films, how many consecutive layers already started to grow on top of the 2nd ML at this chosen moment in time. In the case of 6P, we observe substantial scattering length densities, i.e. coverages, in the 3rd, 4th and even 5th ML, Fig. 5.8 c). This implies that the growth of these consecutive layers is initiated prior to the completion of the 2nd ML, which is characteristic for a rough 3d growth-mode and "wedding cake" structures. In contrast, in the corresponding case of 6PF4, only the 3rd ML grows in parallel with the 2nd ML. This indicates an almost perfect, smooth layer-by-layer growth mode. The exact fit parameters for the two exemplary curves are listed in Table 5.2.

a) **6P**

	d [nm]	ρ [Å^{-2}]	σ[nm]
spacer layer	0.05	0	0.05
5th ML	2.65	$1.07 \cdot 10^{-6}$	0.10
spacer layer	0.10	0	0.10
4th ML	2.65	$3.54 \cdot 10^{-6}$	0.10
spacer layer	0.10	0	0.10
3rd ML	2.65	$8.30 \cdot 10^{-6}$	0.10
spacer layer	0.10	0	0.10
2nd ML	2.65	$1.35 \cdot 10^{-5}$	0.10
spacer layer	0.10	0	0.10
1st ML	2.65	$1.56 \cdot 10^{-5}$	0.10
spacer layer	0.10	0	0.10
initial adsorbants	0.79	$5.59 \cdot 10^{-6}$	0.16
ZnO	-	$2.77 \cdot 10^{-5}$	0.22

b) **6PF4**

	d [nm]	ρ [Å^{-2}]	σ [nm]
spacer layer	0.05	0	0.05
3rd ML	2.30	$2.77 \cdot 10^{-6}$	0.10
spacer layer	0.10	0	0.10
2nd ML	2.38	$1.21 \cdot 10^{-5}$	0.10
spacer layer	0.10	0	0.10
1th ML	2.54	$1.56 \cdot 10^{-5}$	0.10
spacer layer	0.10	0	0.10
initial adsorbants	0.79	$5.59 \cdot 10^{-6}$	0.16
ZnO	-	$2.77 \cdot 10^{-5}$	0.22

Table 5.2: Parameters used to obtain Parratt fits for a) 6P and b) 6PF4 of the exemplary XRR curves acquired shown in Fig. 5.8.

As can be seen from these fit parameters, we had to include in both cases an initial layer on the ZnO substrate. This initial layer accounts for residual adsorbents like H_2O, OH-groups etc. which are present on the reactive ZnO surface prior to the thin film deposition despite the cleaning routine. The thickness d, roughness σ and scattering length density ρ of this initial molecular coverage was obtained from Parratt fits of respective XRR curves acquired before film deposition. These parameters were then kept constant for the fits of the XRR curves acquired during thin film growth. For the scattering length density of ZnO itself tabulated values from the database of the National Institute of Standards and Technology (NIST) were inserted into the fit model.[204] To simulate a stratified structure with the molecular monolayers, and therefore a scattering length density modulation, we included a spacer layer into the fit models for the *in situ* XRR curves of both molecules each ML with a total thickness of 0.1 nm (0.05 nm on top and 0.05 nm from the bottom ML) and a fixed scattering length density of ρ=0.0 Å^{-2}. Thus, to obtain the real lattice spacing of each ML one has to add 0.1 nm to the thickness of each ML shown in the Tables 5.2 a) and b).

The 1st ML of 6PF4 has hence a d value of 2.64 nm, the 2nd ML a d value of 2.48 nm and the 3rd one a d of 2.40 nm. This is in very good agreement with the values obtained from the positions of the higher order Bragg reflections, shown in the inset of Fig. 5.7 and confirms the increasing tilt angle of the 6PF4 molecules at higher MLs.

Performing such fits as demonstrated for the above example for each single XRR curve, acquired *in situ* and in real-time, we achieve the aforementioned very good agreement with the experimental data shown in the 3d plot in Fig. 5.6. The temporal evolution of the scattering length densities and, therefore, the evolution of the coverages can be studied. As shown in Figs. 5.9 a) and b), the coverages of the 6P and 6PF4 layers follow s-shaped curves, when normalizing the scattering length densities to the corresponding values of a filled layer.

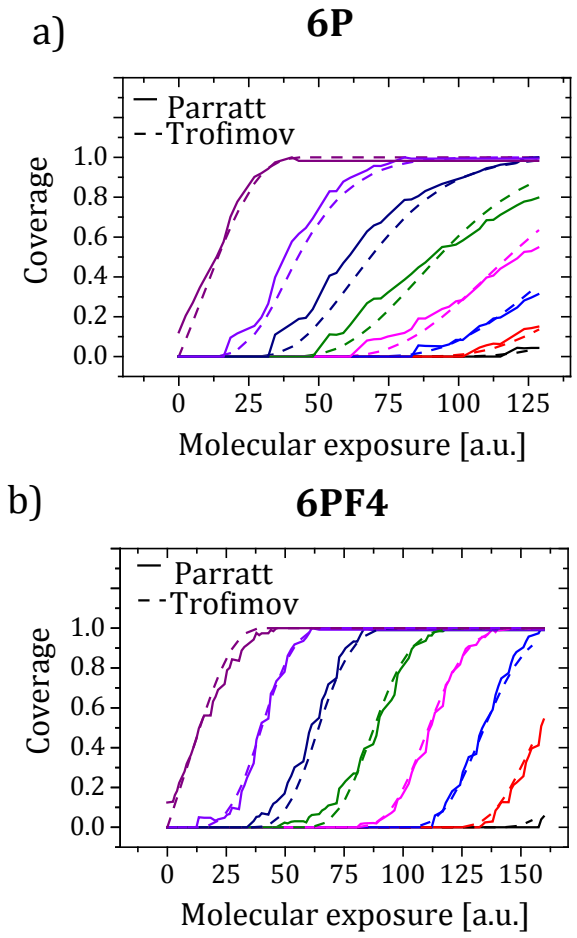

Figure 5.9: Comparison of the calculated layer coverages by using the Trofimov model and fits of the *in situ* XRR curves based on the Parratt formalism for a) 6P and b) 6PF4. The parallel growth of several MLs is observed for 6P indicated rough 3d growth, while 6PF4 coverage curves are reminiscent of a layer-by-layer growth.

5.3.5 Morphology evolution studied at multiple Bragg points

In our second approach, we analyze the experimental data from the 3d plots in Fig. 5.6 by focusing on so-called growth oscillations. In Fig. 5.10 the evolution of the intensity of the specular reflected beam during the growth of a) 6P and b) 6PF4 is shown for three different q_z positions as a function of molecular exposure: $\frac{1}{2} \cdot q_{Bragg}$ (Anti-Bragg point), $\frac{2}{3} \cdot q_{Bragg}$ and $\frac{3}{4} \cdot q_{Bragg}$. Growth oscillations originate from alternating constructive and destructive interferences between the scattered beams from the individual molecular MLs. We refer to section 3.2.3 for more details. At the anti-Bragg position successive layers interfere destructively, i.e., the first molecular layer reduces the ZnO reflectivity, the second layer increases the reflectivity, the third layer reduces the reflectivity again and so on.[200] Oscillations of the X-ray reflectivity are also observed at other q_z points, however, the oscillation period changes from being 2 ML at the $\frac{1}{2} \cdot q_{Bragg}$ anti-Bragg point, to 3 ML at $\frac{2}{3} \cdot q_{Bragg}$ and 4 ML at $\frac{3}{4} \cdot q_{Bragg}$.[79,205] As shown in Fig. 5.10 for 6P, the anti-Bragg oscillations are damped out quickly, while for 6PF4 the oscillations are preserved. Qualitatively this is a further indication for the smooth, layer-by-layer growth of 6PF4, compared to the rougher growth of 6P.

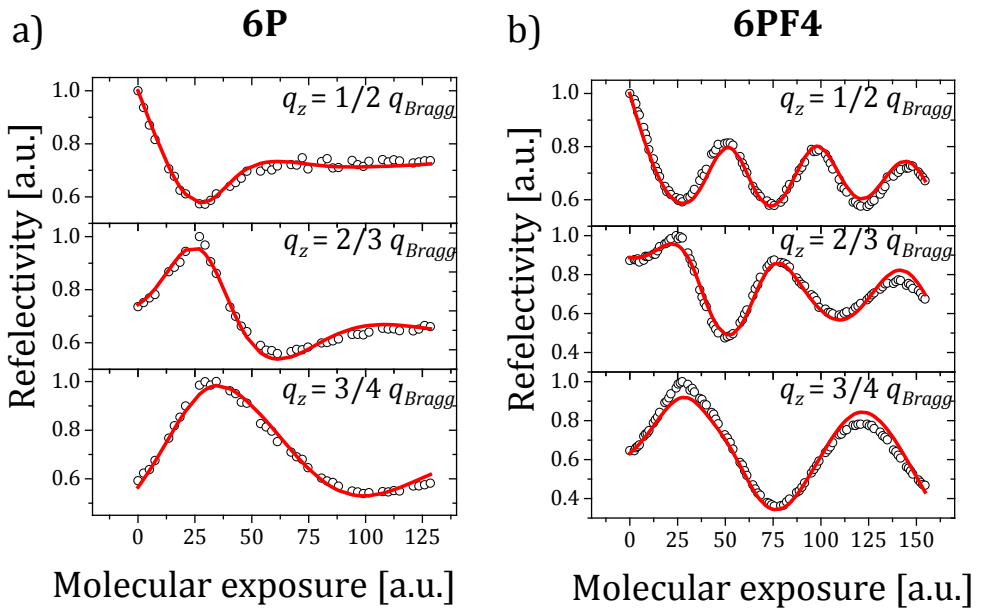

Figure 5.10: Growth-oscillations of a) 6P and b) 6PF4 at three positions of q_z as a function of molecular exposure. The red lines show the best fits using the Trofimov model of the experimental values.

For a quantitative analysis, we fit the growth oscillations at three different q_z points simultaneously to extract the layer coverages for each ML of upright-standing molecules as a function of time. To extract this information, we calculate the X-ray reflectivity using a lattice sum where the substrate scattering as well as the scattering from every layer is added. We take into account the coverage of each layer at a given point in time and, importantly, also the changes in the 6PF4 layer thicknesses for the first MLs. The time dependent layer coverages that enter this lattice sum are simulated using an atomistic, rate-equation model of growth developed by Trofimov *et al.*[107] as previously applied in a simplified form in references[83,101,102] and detailed in chapter 3.2.3. In Fig. 5.10, the best fits as obtained with this model and the software Trofit 0.7.9[21] are given as red lines, while the experimental values are shown as dots. In particular, for the case of the rough 6P growth, with a low number of growth oscillations, the beneficial aspects of combining information from q_z values beyond the anti-Bragg point becomes evident. The additional information allows to constrain the fit parameters of ML thicknesses and critical coverages, i.e., the coverage of monolayer j at which the the $j+1$ layer growth begins. Consequently, the fit accuracy is enhanced. In Figs. 5.9 a) and b) we display the resulting temporal evolution of the ML coverages as inferred from the rate equation model and a good agreement is found with the results from obtained independently from the Parratt fits. Quantitatively, the coverage curves of the Trofimov *et al.* rate-equation model agree with those from the Parratt fits within better than 10 % for 6PF4 and better than 20 % for 6P.

Importantly, the layer coverage curves in Fig. 5.9 a) and b) give a detailed picture of the different growth modes of 6P and the 6PF4. While for both molecules the 1st layer is more than 75 % complete before the 2nd layer reaches a coverage of 5 %, the growth mode starts to differ significantly from the second ML onwards. For 6P, a 3d island growth mode sets in, as the 3rd and even 4th layer start to grow simultaneously with the second layer as evidenced by the shallow coverage curves. In the case of the 6PF4 growth, the coverage curves show a steep slope up to at least the 7th ML, i.e., growth proceeds in a layer-by-layer mode.

With the knowledge of time-dependent coverage Θ_j of layer j, the root-mean-square (RMS) roughness can be calculated to quantify the effect of fluorination of 6P on film smoothing:

$$\sigma(t) = \sqrt{\sum_{j=1}^{Z-1} \left((\Theta_j(t) - \Theta_{j+1}(t)) \cdot \left((j-1) - \sum_{j=1}^{Z-1} \Theta_j(t) \right)^2 \right)}. \tag{5.1}$$

Here, Z is the total number of molecular MLs. The resulting curves are shown in Figs. 5.11 a) and b) for 6P and 6PF4 films, respectively. The roughness evolution of 6P has a minimum, when the smooth surface of the 1st ML is completed, but then a significant increase of the roughness occurs with the beginning of the 2nd ML growth as shown in Fig. 5.9 a). In contrast, the roughness curve for 6PF4 shows slight minima, every time the islands within a ML coalesce and form a smooth, continuous film. Since the roughness at this minimum is non-zero, we can conclude that the layer-by-layer growth is not fully ideal. A comparison of the 6P and 6PF4 roughness curves in Figs. 5.11 a) and b) clearly shows that the 3d growth of 6P results in a surface roughness, which, for a comparable film thickness of about 4-5 ML, is twice as high as in the case of the layer-by-layer growth of 6PF4.

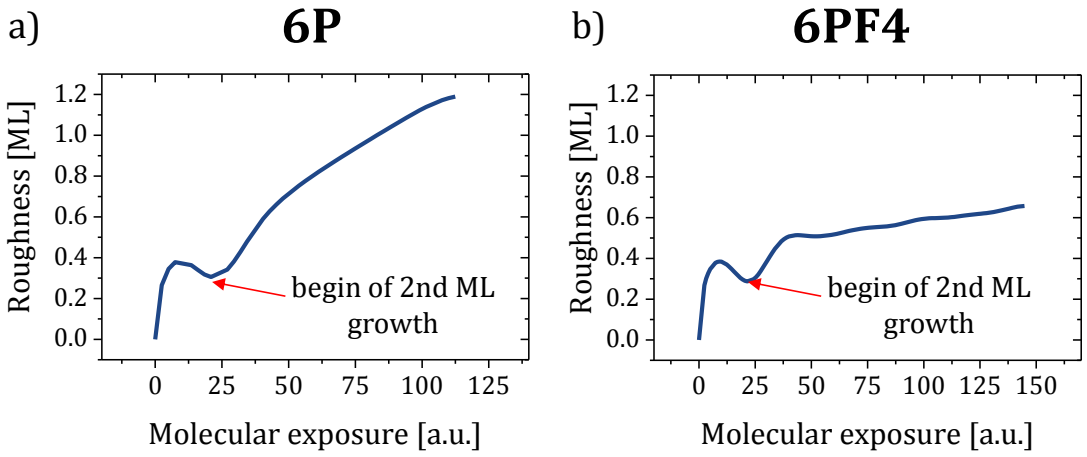

Figure 5.11: Calculated RMS roughness of a) 6P and b) 6PF4 during the film growth is shown.

5.3.6 The impact of substrate induced phases and crystal phase purity on film smoothing

All performed experiments conclusively show that terminal fluorination of 6P causes a transition from a 3d growth for the parent 6P to an almost 2D growth mode for 6PF4 on ZnO(10$\bar{1}$0). In the following we discuss factors, which may contribute to this pronounced change.

The fluorination of 6P in the four "corner" positions changes intermolecular electrostatic interactions through the introduction of two local dipole moments at both molecular termini. The crystal cohesive energy will thus be different for the two molecules. Furthermore, a flat-lying 6PF4 molecule, diffusing on the surface of an island exposing fluorine atoms at its boundary, will experience a substantially altered electrostatic field as compared to 6P, where the islands are presenting hydrogen at their periphery. As a consequence, the activation energy for molecules diffusing on islands as well as the Ehrlich-Schwoebel barrier, both critical parameters in a kinetically controlled growth process, will differ. Indeed, an increase of the Ehrlich-Schwoebel barrier with increasing crystal cohesive and surface binding energies has been predicted.[40] Our result of 6PF4 layer-by-layer growth therefore suggests that both cohesive as well as binding energies are reduced by terminal fluorination. Further theoretical input is required to verify the sign and to assess the magnitude of the change in the energy terms.

The physical size of 6P and 6PF4 molecules is nearly identical. However, changes in the intermolecular electrostatic interactions as well as possibly weak C-H$\cdots$F-H bonding may cause subtle changes in the structure of the bulk phase of the films, entailing the larger molecular tilt angle of 6PF4 than for 6P. The molecular tilt angle has previously been identified to influence the magnitude of the Ehrlich-Schwoebel barrier E_{ES},[39,206] which is the energy barrier for interlayer diffusion. For rod-like molecules, a larger molecular tilt has been related to a smaller step edge barrier, accounting for the lower energy required to bend a molecule around an inclined island boundary during the downward motion. Consequently, the here observed molecular orientation of 6PF4 in the bulk phase implies a lower E_{ES} and contributes to enhanced downward mass transport, facilitating layer-by-layer growth. Inspecting the 6PF4 crystal structure close to the interface, we, however, evaluate a surface induced structure with the molecular tilt angle being smaller compared to the bulk. From our measurements we deduce that the tilt angle changes gradually with film thickness. We therefore observe a change from more upright standing to slightly tilted molecules in the first 3 MLs. With regard to the Ehrlich-Schwoebel barrier one would thus expect that the more upright standing surface induced phase, increases the E_{ES} and hinders layer-by-layer growth at the initial growth stage. However, according to our results nucleation of the second layer starts, when the ZnO surface is almost completely covered by islands. This suggests that the effect of a larger E_{ES} in the first 6PF4 ML might be counterbalanced by a better molecular diffusivity due to a lower surface energy. Its minimisation is the driving force behind the surface

induced structure, so that for more upright standing molecules the surface energy is apparently lower than for tilted molecules as found in the bulk phase of the film. A lower surface energy on top of the first monolayers leads to enhanced diffusivity of admolecules and therefore contributes to better layer-by-layer growth. Similar to the present case, a surface induced phase with more upright standing molecules has been correlated with layer-by-layer growth in the similar molecular system di-indenoperylene.[19,83] Another significant aspect, which may influence the divergent roughness evolution of the thin films, is the difference in the crystal structure of 6P and 6PF4. While in 6P the β- and γ-phases grow in coexistence, crystal-phase purity and, therefore, the growth of only one crystal phase is observed in 6PF4 films. In 6P, the grain boundaries occurring between different phases can act as nucleation sites for succeeding layers and, thus, may contribute to the observed film roughening.

5.3.7 Summary

By applying *in situ* real-time X-ray reflectivity measurements, we demonstrate how terminal fluorination of 6P drastically alters the growth mode and the resulting crystal structure of molecular thin films. In our study, fluorination enhances downward mass transport through a combination of increased surface diffusivity and a lower Ehrlich-Schwoebel barrier, leading to a smooth, almost layer-by-layer thin film growth. Characteristic features of the thin films are summarized in Fig. 5.12.

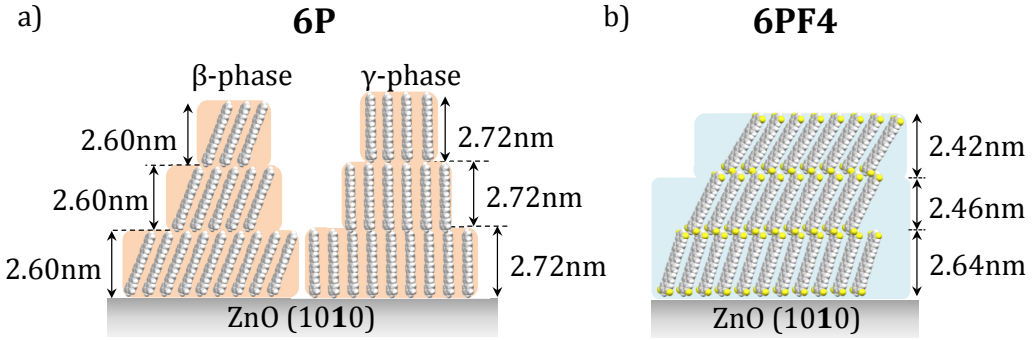

Figure 5.12: Schematic drawing illustrating the rough 6P growth with two different polymorphs in a) and the smooth 6PF4 growth with a surface induced structure in b).

We find that both molecules grow in a highly crystalline fashion with almost upright standing molecules when deposited at room temperature on ZnO(10$\bar{1}$0). We further demonstrate that the fluorinated molecule grows in a phase pure manner with a gradually increasing molecular tilt angle in the first three MLs. In contrast 6P thin films exhibit a simultaneous growth of β- and γ-phases and we find no evidence

for a changing tilt angle. However, the most striking difference is the change from 3d for 6P to an almost 2d morphology for its fluorinated derivative. Our results demonstrate that selective fluorination can decisively alter growth processes and film roughness and therefore presents a viable strategy to produce crystalline organic layers with thin film morphologies as demanded for the use in opto-electronic devices.

5.4 Impact of asymmetrical fluorination of *para*-sexiphenyl on nucleation and film smoothing

In the following study we compare the growth of *para*-sexiphenyl (6P) and its chemically tuned derivative 6PF2 on isotropic silicon oxide substrates. In the case of 6PF2 only two hydrogen atoms at one molecular end are substituted by fluorine atoms. However, this modification breaks the symmetry of the parent 6P molecule and furthermore induces a local dipole moment at one molecular end. An interesting question is, whether such subtle modification will induce any changes in the film growth-mode and if it does influence nanoscale processes governing the molecular self-assembly. By applying *in situ* real-time X-ray reflectivity (XRR) growth oscillations we demonstrate that, compared to the parent 6P molecule, its fluorinated derivative grows in a drastically smoother fashion and reduces the film roughness of 4-5 ML thick films by a factor of two. Comparing the molecular orientations and island shapes by *ex situ* AFM, we find close similarities in the roundish island shapes and the almost upright standing molecular orientation on the surface. However, from a quantitative analysis of the scaling of the island densities with substrate temperature and growth rate in the framework of nucleation theory, we find for 6PF2 an approximately 0.56 eV larger diffusion energy barrier and a surprising increase of the attempt frequency for surface diffusion by seven orders of magnitude. Using these values, we evaluate a decreased in-plane diffusivity D of 6PF2 at the lowest studied temperatures T=60 °C. However, in addition to that, we show that fluorination also impacts the step-down diffusivity S. The comprehensive impact of a comparably small modification on the molecular growth, demonstrates the promising potential of chemical tuning as a control parameter to tailor thin film architectures.

5.4.1 Experimental procedures

The deposition of *Para*-sexiphenyl ($C_{36}H_{26}$, 6P) and its fluorinated derivative 6PF2 ($C_{36}H_{24}F_2$) was performed via organic molecular beam deposition (OMBD) in a UHV chamber at a base pressure of below 3.0 x 10^{-7} mbar. Details on the deposition technique are given in section 2.2.1. Silicon wafers with a native silicon oxide layer were used as substrates. Prior to the deposition, the samples were cleaned in a standardized process described in section 2.2.2. The X-ray measurements were performed using a lab based X-ray diffractometer, as shown in section 3.2.5, at a wavelength of λ= 0.15406 nm from a rotating copper anode source. The AFM images were recorded on a *Bruker MultiMode 8* in *ScanAsyst PeakForce* tapping mode, which is introduced in section 3.1. 6P was purchased from *TCI Deutschland GmbH*

and used as-received without further purification. The fluorinated derivative 6PF2 was synthesized by Yves Garmshausen, HechtLab, Humboldt university of Berlin, as discussed in the introduction to this chapter.

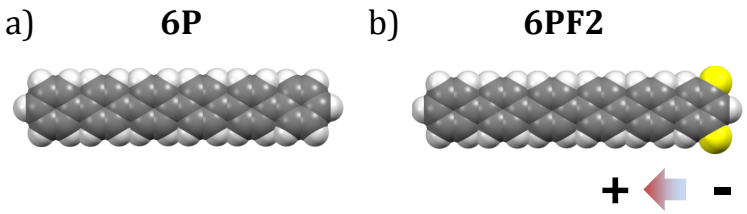

Figure 5.13: Sketch of a) *para*-sexiphenyl (6P), composed of six linked phenyl rings, and b) its asymetrically fluorinated derivative 6PF2.

5.4.2 Comparing 6P and 6PF2 morphologies at a fixed substrate temperature of T=100 °C

For the analysis of the morphology of the 6P and 6PF2 films we used *ex situ* AFM as a well-established technique. However, particularly during the acquisition of images of the 6PF2 films, we observed an increased interaction of the AFM tip with the film material. During the scanning, molecules adhered to the as-received tips. Therefore, a serious decrease of the image quality was noticed as displayed exemplary in Fig. 5.14a).

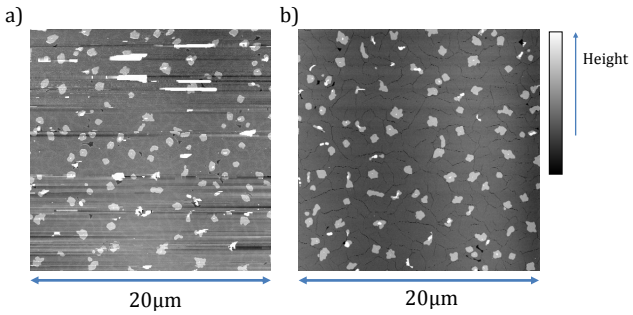

Figure 5.14: a) AFM image of a $\sim$ 1.2 ML thick 6PF2 film on silicon oxide, acquired with an as-received 2 N/m silicon tip. Some 6PF2 molecules interact strongly with the tip, decreasing the image quality. b) The same sample acquired with a silane-coated AFM tip. The image quality is significantly increased.

A strategy to greatly minimize the interaction of 6PF2 with the AFM tip was thus needed and was advanced within this study. It constitutes in the hydrophobic tip-coating by dichloro-dimethyl-silane (DDMS, $Si(CH_3)_2Cl_2$). The coating process,

as described below and as used for AFM image acquisition in the following, has been applied in the group of Prof. Rabe (Institute of Physics, Humboldt university of Berlin) by Philipp Lange and Manuel Gensler. The process comprises two steps. In the first step, the as-received tips are exposed to UV light for approximately 15 min to clean the tip from organic residuals and oxidize their surface. In literature, surface cleaning with UV/ozone is an established and effective approach.[207,208] In the second step, the tip was incubated in an enclosed chamber containing a 1 ml reservoir of liquid DDMS. Due to the low vapor pressure of the liquid, there is immediately a sufficient amount of gaseous DDMS molecules, which chemically bind to the surface of the AFM tip. After approximately 15 mins, the tip is sufficiently covered with the hydrophobic silane. Although, to our knowledge, their application on AFM tips is yet not common, silanes are widely used as hydrophobic surface coatings in other fields.[209,210] As a result of the coating, the interaction of 6PF2 molecules with the tip during the image acquisition is reduced and the image quality is significantly increased as exemplary demonstrated in Fig. 5.14b).

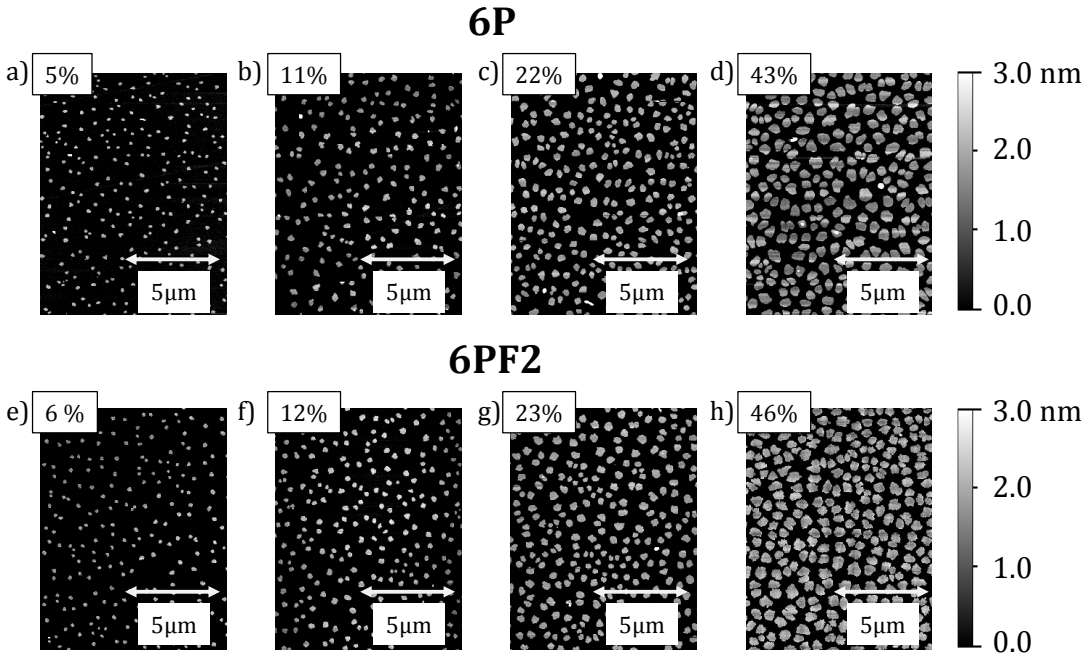

Figure 5.15: Series of AFM images illustrating the morphology evolution at comparable sub-ML coverages of a) 6P and b) 6PF2 films grown at T=100 °C. Qualitatively, the growth of both materials proceeds in a very similar manner through the nucleation of islands of apparently equal size, shape and quantity.

In Figs. 5.15 a) and b) series of characteristic AFM images display the evolution of the formation of the first 6P and 6PF2 monolayer (ML) as a function of coverage.

The films were prepared at a substrate temperature of T=100 °C and an evaporation rate of 0.1 nm/min. The images were acquired at similar film coverages for both molecules allowing for a direct comparison of the growth process. Qualitatively, the early growth stages of both films appear to proceed in a very similar manner. Both molecules form compact, roundish islands and no differences concerning the island shape are visible. Further, the size and density of the islands show no striking differences. For both molecules the islands are uniform in their heights. From height distributions, as exemplary shown in Figs. 5.16 a) and b), we determine an essentially equal island height of 2.46 nm in the case of the unsubstituted 6P and 2.42 nm for 6PF2. These values imply that the islands consist of almost upright standing molecules. Such an arrangement was already observed for 6P growth on different substrates, including silicon oxide.[22,39,132,133] We also note that the number of islands essentially does not change for coverages of about 10 and 20 %. In contrast, at about 40 % coverage we already observe how the borders of some islands touch other and melt to bigger islands. Accordingly, we can estimate that the coalescence period of monolayer formation sets in at about 40-45 % coverage, while the so-called aggregation regime with an essentially constant, maximum island density proceeds between 10-40 % coverage. This maximum island density is approximately reached at coverages between 0 and 10 %, marking the nucleation regime.

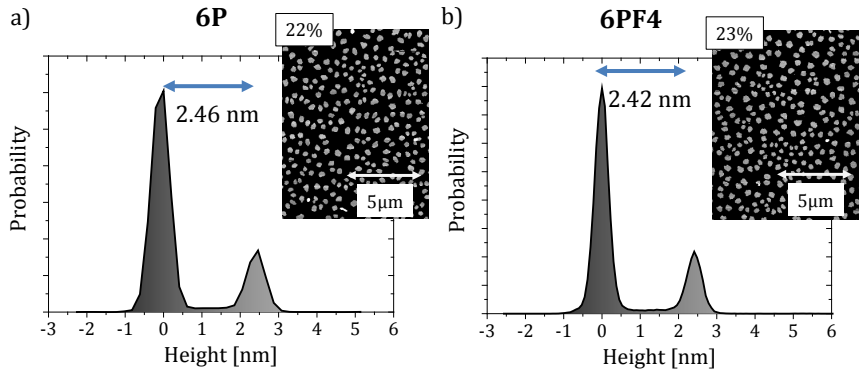

Figure 5.16: Height distributions of a) 6P and b) 6PF2 islands. The values indicate in both cases an almost standing upright orientation of the molecules.

We now compare the 6P and 6PF2 morphologies at higher coverages, focusing on the 2nd ML and 5th-6th ML growth. In Figs. 5.17 a)-b) and c)-d) we display AFM images of multilayer films of 6P and 6PF2, respectively. For both molecules, we find the second ML growth to be similar to the sub-ML regime, see Figs. 5.17 a) and c). At this coverage, we still can identify similar compact island shapes as in the sub-ML regime. However, we observe the nucleation of islands on top of existing

islands, although the second ML is yet not closed. Such behavior indicates that the growth does not proceed in an ideal layer-by-layer fashion. At yet higher coverages, corresponding to the growth of the fifth and sixth ML, the differences in the growth mode of 6P and 6PF2 become drastic, see Figs. 5.17 c)-d). While for 6PF2 the growth is still mainly two-dimensional, for 6P the formation of three-dimensional, terraced mounds can be observed and the individual MLs are not closed. In this aspect, the here observed behavior is reminiscent of 6P growth on mica.[39] Evidently, such terraced mounds or "wedding cake" structures increase the roughness of the film. Furthermore, the separation between the mounds deteriorates the in-plane charge carrier transport, which is the reason why such morphologies are usually non-desired for opto-electronic applications.

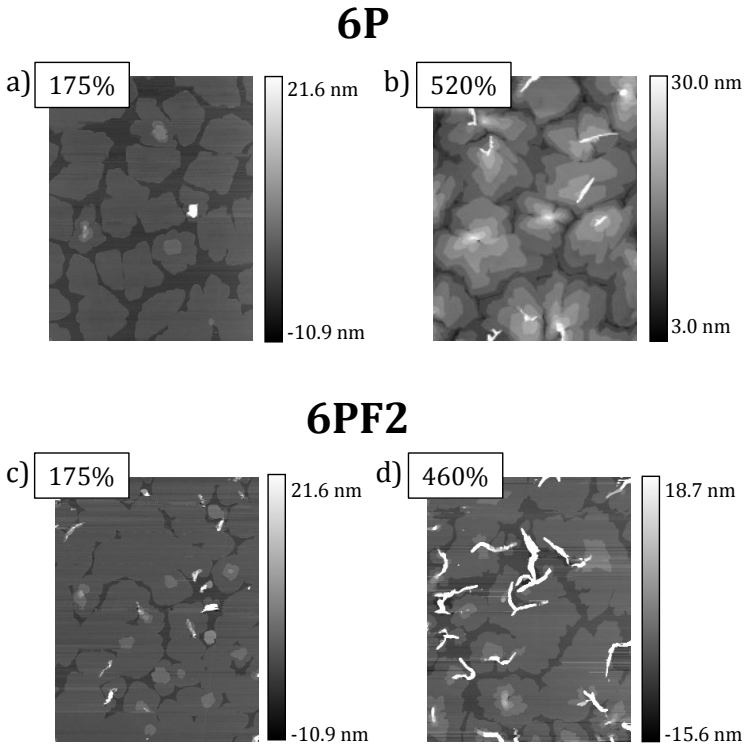

Figure 5.17: Series of AFM images illustrating the morphology evolution of a)-b) 6P and c)-d) 6PF2 at comparable coverages in the multilayer regime. At higher coverages, the growth-mode of the two molecules deviates. In the case of 6P, pronounced wedding-cake structures are visible, which increase the film roughness. In contrast, 6PF2 growths in a smoother, two-dimensional fashion.

In contrast, the morphology of several ML-thick 6PF2 films still exhibits an only slightly distorted layer-by-layer growth-mode. In fact, apart from the island sizes, the 6PF2 film morphologies in the 2nd and the 5th ML are qualitatively very similar,

see Figs. 5.17 c) and d). This indicates that, contrary to 6P, 6PF2 preserves its initial growth mode. At the highest investigated film thickness, we locally find some terraced mounds, but their maximum height is only two MLs compared to the several ML high 6P mounds. We thus conclude that in 6PF2 the main part of the incoming molecules contributes to the lateral island growth. These islands will coalesce to a smooth, closed ML. Additionally, at this later growth stage, elongated objects of several nm heights appear. In literature these are referred to as needles and assigned to lying down molecules. For 6P such structures are known for the growth on ordered substrates and on mica.[39,211,212] Here, we find that 6PF2 molecules can also assemble to needle-like structures.

5.4.3 Evolution of the out-of-plane structure of 6P and 6PF2 as a function of substrate temperature

The AFM micrographs given above provide a good overview of the film morphologies in the real space. However, monitoring the growth *in situ* and in real-time is advantageous when analyzing dynamic processes, such as a steady growth mode transition from smooth layer-by-layer towards rough 3d growth. X-ray reflectivity (XRR) growth oscillations contain rich information on the evolution of the out-of-plane film morphology as we have shown, e.g., in our growth study of PTCDI$-C_8$ in section 4.1 and as demonstrated in a variety of published studies.[34,63,80,83,102] For the present case of 6P and 6PF2 growth, the oscillations were acquired by monitoring the XRR intensity at $q_z \approx 0.11 \text{Å}^{-1}$ as a function of molecular exposure, i.e., deposition time $\times$ growth rate, close to the so-called anti-Bragg point of the (001) Bragg reflection of 6P, defined as $q_z = q_{anti-Bragg} = q_{(001)Bragg}/2 = (4\pi/\lambda \cdot \sin(\alpha_{(001)Bragg}))/2$ in terms of the reciprocal space vector q_z. Here, λ is the wavelength of the incoming X-rays, and $\alpha_{(001)Bragg}$ is the Bragg angle of the (001) reflection.

In Figs. 5.18 a)-f) we display the growth oscillations of 6P and 6PF2 acquired at different substrate temperatures as grey dots. Each local minimum and maximum of the oscillations corresponds to the completion of a single ML. Further, as discussed in more detail in section 3.2.3, the damping of the growth oscillations is directly related to the film roughening. For the case of 6P, we observe a strong dependency of the oscillation damping on the substrate temperature, see Figs. 5.18 a)-c). At low temperatures of T=60 °C, the oscillations are strongly suppressed after the completion of the 3rd ML. In contrast, at the highest studied substrate temperature T=130 °C the growth oscillations are well-pronounced at least up to

the 7th ML. Therefore, we conclude that a significant 6P film smoothing can be achieved by increasing the substrate temperature to 130 °C. In comparison, the effect of an increased substrate temperature on the smoothing of 6PF2 is significantly lower, see Figs. 5.18 d)-f). Although the local minima and maxima become more pronounced by increasing the substrate temperature, we can distinguish oscillations up to the 6th or even 7th ML already at T=60 °C. This shows a strong effect of fluorination on the film roughness, which we want to quantitatively analyze in the following.

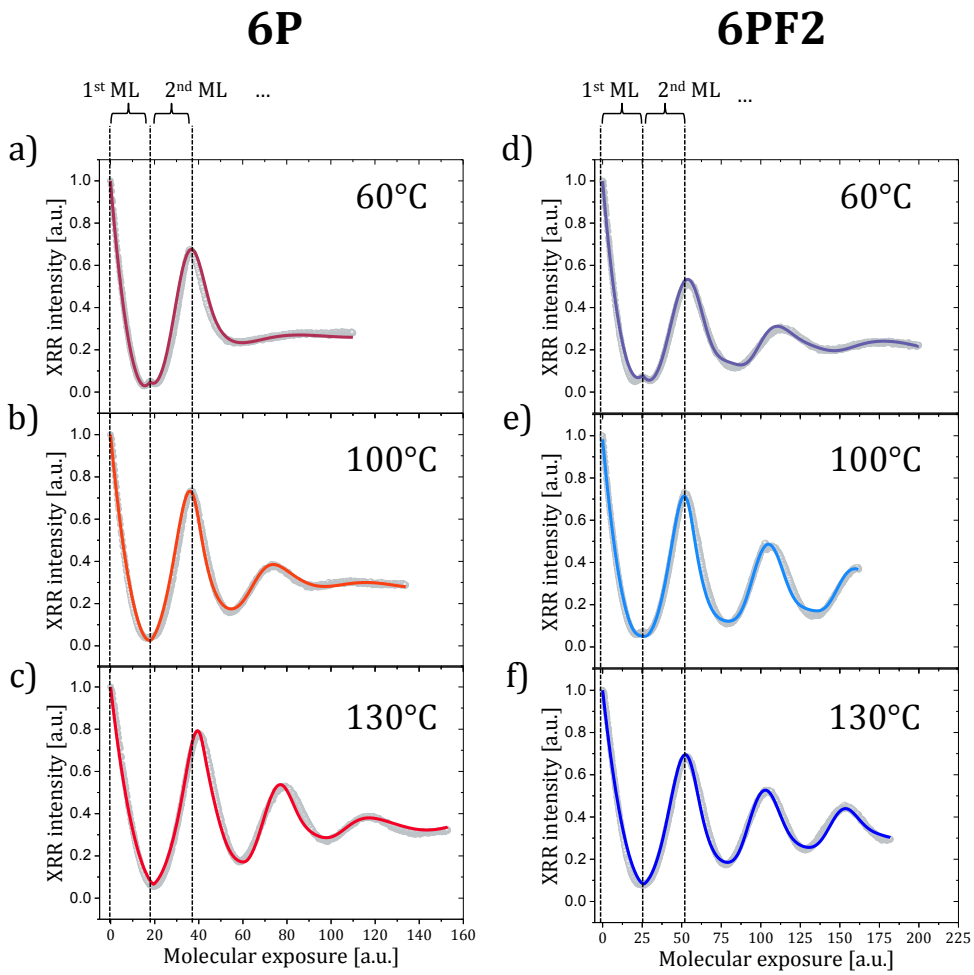

Figure 5.18: Temperature-dependent growth oscillations at the anti-Bragg points of a)-c) 6P and d)-f) 6PF2 acquired *in situ* and in real-time during thin film growth. The grey dots represent the data points and the colored lines show fits to a rate equation model. The lower damping of the oscillations in the case of 6PF2 indicates a smoother film growth.

We fit the growth oscillations by applying a rate-equation model, which describes the evolution of the out-of-plane morphology and film roughness as a function of time and is mainly based on the works of Trofimov and Mokerov[107] and Woll *et al.*.[101] In the following, we refer to this as the Trofimov model, which is described

in more detail in section 3.2.3. Here, we slightly reformulate the rate equation (3.18) as:

$$\frac{d\Theta_j(t)}{dt} = R_j \cdot (\xi_{j-1}(t) - \Theta_j(t)) + \underbrace{R_{j+1} \cdot (\Theta_j(t) - \xi_j(t))}_{\text{downward transport rate } (DTR)}, \tag{5.2}$$

with Θ_j being the coverage of layer j, i.e., a time-dependent quantity giving the portion of the surface covered by layer j. R_j is the effective growth rate of layer j, which accounts for the sticking coefficient and - if present - desorption. ξ_j is the time-depending, so-called feeding zone on top of the growing ML j. The feeding-zone is the central concept of the Trofimov model and states that each molecule arriving within the feeding-zone of layer j will initiate or contribute to the growth of layer $j+1$. All other molecules will be transported downward and contribute to the growth of layer j. For the feeding zone of the substrate, we define ξ_0=1.

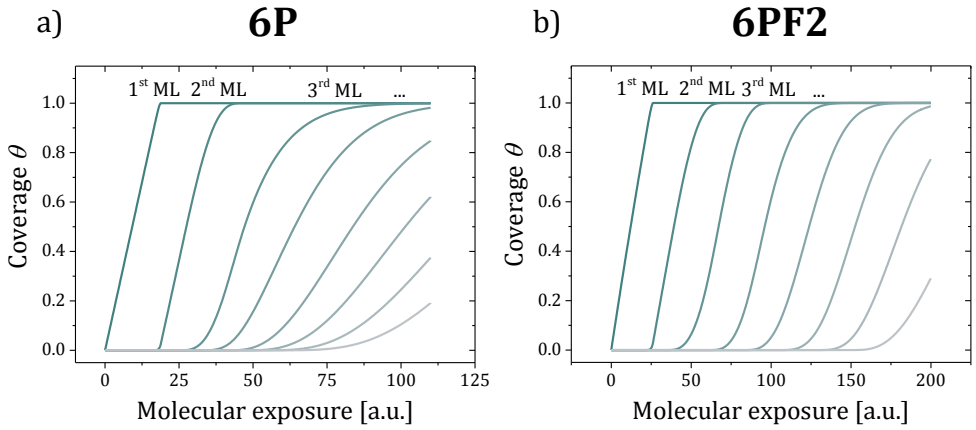

Figure 5.19: Exemplary coverage curves as obtained from the Trofimov model fits to the 6P and 6PF2 growth oscillations at T=60 °C. One observes that with increasing film thickness several MLs start to grow simultaneously, which initiates film roughening.

To fit the growth oscillations we used the software Trofit 0.7.9.,[21] which is based on the Trofimov model. As demonstrated by the continuous lines in Figs. 5.18 a)-f), the fits match the data points very well. In Fig. 5.19 we exemplarily plot the coverage of each ML as yielded from the fits for films grown at T=60 °C. We observe that with increasing deposition thickness, the coverage curves adept an s-like shape and several MLs start to grow simultaneously. This marks the transition towards a rough, layer + islands growth mode and is in full accordance with the findings from the AFM images. Note, that for the 6P film this transition proceeds much faster.

Using the values of the time-dependent coverages Θ_j, the root-mean-square roughness σ can be calculated as a function of molecular exposure by using eq. (5.1) as given in the previous section. The so-calculated roughness evolution of 6P and 6PF2 films grown at different substrate temperatures is presented in Figs. 5.20 a) and b). Each minimum in the curves corresponds to the completion of a ML. In perfect layer-by-layer growth, the roughness at the minima would be zero. Here, the minima are non-zero, and in the best case they are distinguishable only up to the 4th ML before getting smeared out. From this point on, the roughness begins to steadily increase as the film growth-mode is changing. In accordance with our qualitative analysis from the anti-Bragg oscillations, we find a strong correlation of 6P film roughness and substrate temperatures. In numbers, 6P films of approximately equal thickness grown at 60 °C, are at least twice as rough as films at 130 °C. Importantly, from a comparison of Fig. 5.20 a) and b), we find how strongly chemical tuning of 6P can suppress film roughening. For example, 6PF2 films grown at 60 °C have essentially the same roughness as the untuned parent molecule 6P grown at 130 °C. Further, we quantitatively confirm that the substrate temperature has a significantly lower impact on the film roughness in the case of 6PF2, at least in the temperature range probed here.

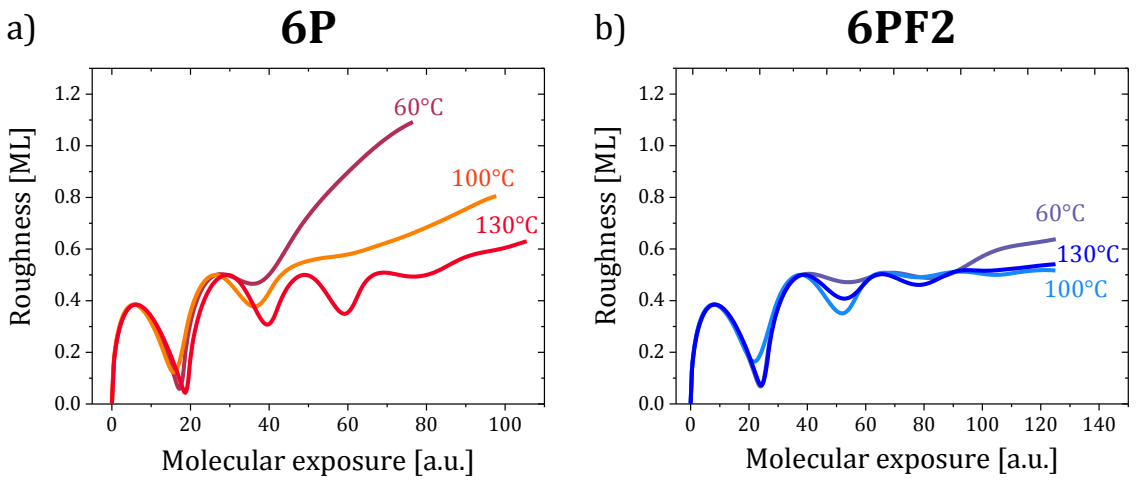

Figure 5.20: Temporal evolution of film roughness as a function of the substrate temperature. With increasing substrate temperature, the roughness of both a) 6P and b) 6PF2 films decreases. Note the almost doubled roughness of 6P films compared to 6PF2 at T=60 °C.

In general, film roughening is a result of a deteriorated downward mass transport, i.e., molecules landing on top of an island are not efficiently enough transported downwards. Thus, the film grows in wedding-cake structures as shown in Fig. 5.17 c). Using the parameters obtained from the Trofimov model fits to the growth

oscillations, we can quantify the downward mass transport. To do so, we focus on equation (5.2), which describes the time-dependent change of the coverage of layer j, i.e. the growth of ML j.

The first term of equation (5.2), $R_j \cdot (\xi_{j-1}(t) - \Theta_j(t))$, accounts for the contribution of non-desorbing and sticking molecules arriving from the molecular beam directly into layer j. However, the ML j grows also due to the downward transported molecules from upper layers, which is referred to as the downward transport rate (DTR) and is described by the second term, $R_{j+1} \cdot (\Theta_j(t) - \xi_j(t))$. In Figs. 5.21 a) and b) we exemplarily plot the DTRs for the first four MLs of 6P and 6PF2 films grown at 60 °C. For clarity, we use as the x-axis the total coverage in terms of ML as obtained from the Trofimov model fits.

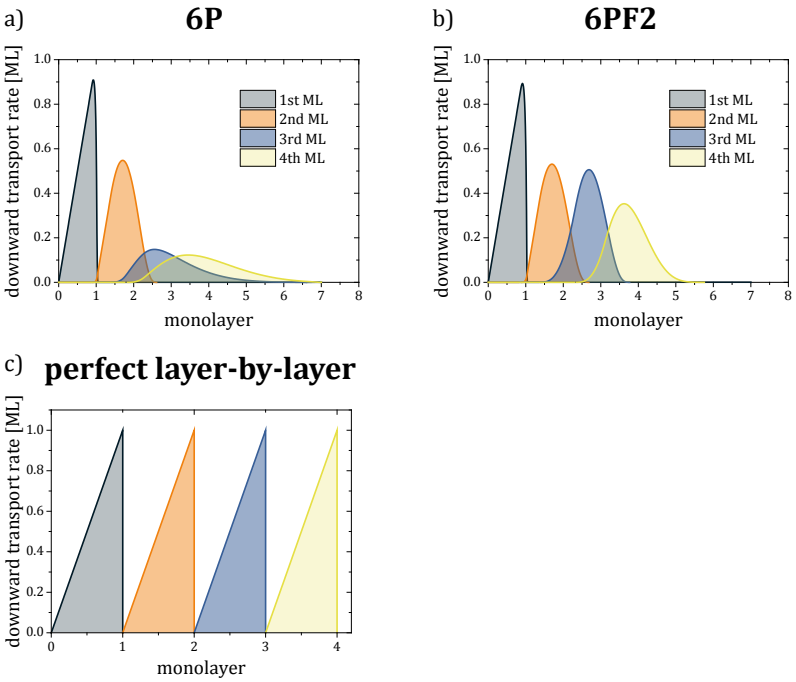

Figure 5.21: Exemplary curves showing the downward transport rates (DTR) of the first four monolayers of a) 6P and b) 6PF2 films grown at 60 °C.

In a perfect layer-by-layer growth, the DTRs for each single ML would be completely identical, as shown in Fig. 5.21 c). One would observe a steady increase of the DTR until the maximum value of 1 is reached, which marks the completion of the j'th ML. At this point the DTR would instantly drop off to zero. As evident, the DTR curves of 6P and 6PF2 resemble the theoretical curve for layer-by-layer growth only in the 1st ML. After that, a significant deviation is observed for both molecules. Interestingly, the DTRs of 6P and of its chemically tuned counterpart are essentially

equal for the first two MLs and begin to strongly differ in the third and higher MLs.

By integrating the *DTR*s over the film thickness (in terms of ML), we can calculate how much material is actually transported downwards from the j+1 layer into the j layer. Thus, we can determine the interlayer transport. We have conducted this integration for the first four 6P and 6PF2 layers grown at three different substrate temperatures as shown in Figs. 5.22 a) and b). From the considerations above we can conclude that in perfect layer-by-layer growth the interlayer transport would be 0.5 ML. This value is almost ideally reached in both molecular films in the first two MLs. For 6PF2 the interlayer transport then stays essentially at this value. Even in higher MLs and at the lowest of the investigated substrate temperatures the interlayer transport reaches about 0.45 ML. In case of the unsubstituted 6P a strong temperature dependency is observed in full accordance with the points discussed above. For 6P grown at 60 °C, less than 0.3 ML is transported from the 5th to the 4th ML. Comparing this with 6PF2 we find that the chemical tuning of the molecule induces an increase of the mass transport by a factor of 1.5 at higher film thicknesses, which accounts for the decreased film roughening.

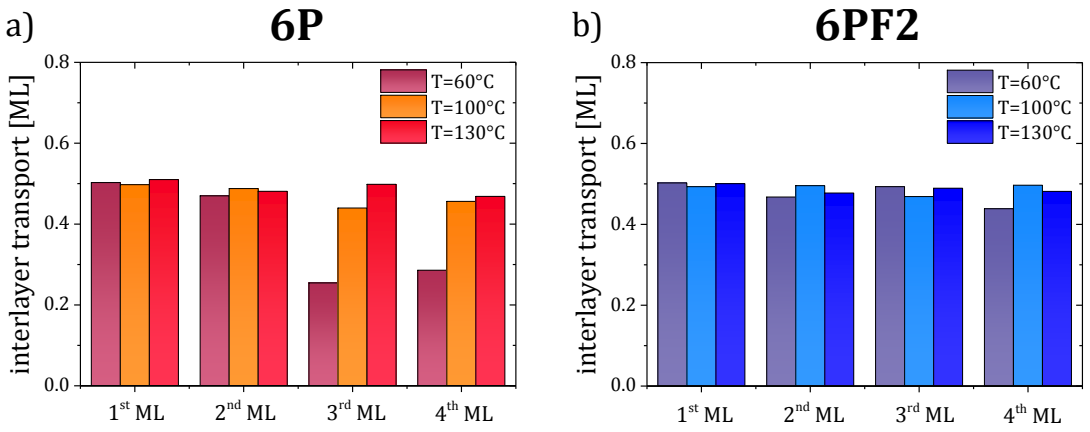

Figure 5.22: Calculated interlayer transport from the j+1'th layer into the j'th layer (j from 1 to 4) for a) 6P and b) 6PF2 films grown at three different substrate temperatures. The interlayer transport is determined as the integral of the DTR over film thickness in ML units.

5.4.4 Quantifying nanoscale in-plane growth parameters of 6P and 6PF2

From the analysis of the X-ray experiments we determined the temperature dependency of the out-of-plane morphology of the 6P and 6PF2 films. In the following we perform a complementary AFM analysis of the in-plane morphology and, specifically, of the island densities. By applying mean-field nucleation theory,[11] we can determine and compare quantities such as nucleation energy E_{nuc} and critical nucleus sizes i of 6P and 6PF2 films, where i defines the number of molecules contained in the largest non-stable island.

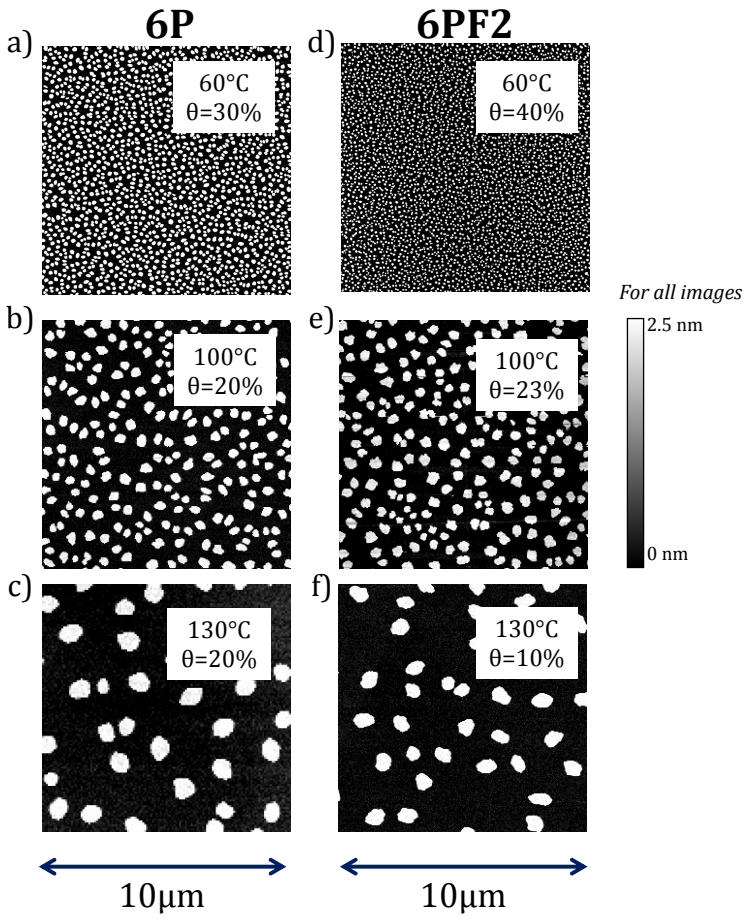

Figure 5.23: Characteristic AFM images of a) 6P and b) 6PF2 films grown at three different substrate temperatures at a deposition rate of 0.1 nm/min.

In Figs. 5.23 a)-f) characteristic AFM images of 6P and 6PF2 films grown at three different substrate temperatures are shown. The images were taken at sub-ML coverages during the lateral growth stage, where the island density is maximum and approximately constant. At each temperature, 6P and 6PF2 form islands of almost

upright standing molecules. The islands are very similar in their shape being compact and roundish and the substrate temperature appears to not alter the shape. This is an interesting finding, since in previous publications on the 6P growth a transition from roundish towards dendritic shapes with increasing substrate temperature was found.[132,133] We attribute this to differences of the surface energies of the silicon oxide, potentially induced by the different cleaning procedures in these studies. As we infer from Figs. 5.23 a)-f), for both molecules the size of the islands, and therefore the island density N_{max}, depends strongly on the substrate temperature. This is in qualitative accordance with nucleation theory, which was discussed in detail in sections 2.1.1 and 4.1.6. Within this theory N_{max} can be described by:

$$N_{\max} = \eta \cdot N_0 \cdot \left(\frac{4 \cdot GR}{N_0 \cdot \nu_0}\right)^p \cdot \exp\left(\frac{E_{nuc}}{kT}\right). \tag{5.3}$$

The exponent p is a function of the critical nucleus size i. The nucleation energy E_{nuc} contains as well a dependency on i, but also on various energy barriers for different nanoscale processes, such as diffusion. The pre-factor η is a weakly varying function of the coverage and i being typically 0.2-0.3,[11] while ν_0 is the attempt frequency for surface diffusion. N_0 is the number of surface sites per unit area. In the case of 6P, N_0 equals $4.4 \cdot 10^{14}$ molecules/cm^2 in the 6P [001] plane.[22]

Equation 5.3 allows us to determine E_{nuc} and p by analyzing the impact of the substrate temperature and the growth rate on the maximum island density $N_{\max}$. To study the temperature influence, we analyze the logarithm of $N_{\max}$ of 6P and 6PF2 in the 1st and 2nd ML as a function of $1/kT$, as plotted in Fig. 5.24 a). For both molecules and MLs, the measured data points lie on straight lines. The slopes of these linear functions equal the corresponding nucleation energies E_{nuc}. We note that for both molecular specimens the nucleation energy slightly increases in the 2nd ML. However, the observed increase of about 20 meV is within the error bars of the linear regression. We thus consider E_{nuc} as essentially independent of the film thickness - at least in the first two MLs. In contrast, E_{nuc} does strongly depend on the molecular material. Comparing the values for 6P and 6PF2, we find that the nucleation energy of the latter is about 100 meV larger, which constitutes an E_{nuc} increase by about 15 % induced by fluorination. We further note that at lower temperatures, the island density of 6PF2 is larger than of 6P. This difference is more pronounced in the second ML. However, at the highest analyzed substrate temperature, i.e. at 130 °C, the island densities of 6P and 6PF2 are almost identical.

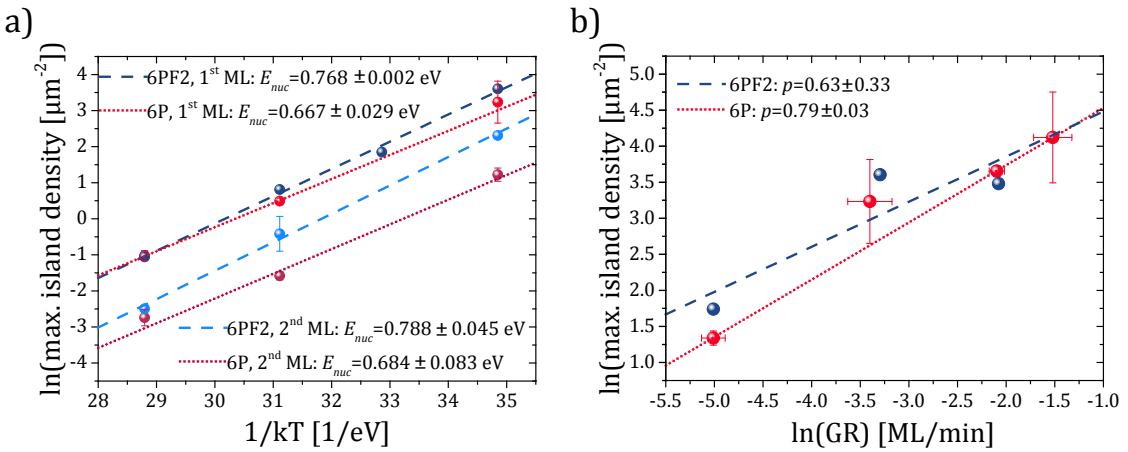

Figure 5.24: Logarithmized maximum island densities as obtained from the AFM images. The temperature variation series were acquired at a fixed growth rate of 0.1 nm/min, while the growth rate variaton was performed at a constant substrate temperature of 60 °C. The data points can be fitted by linear functions in agreement with mean-field nucleation theory. In a) the slopes equal the nucleation energy E_{nuc}. In contrast, the slopes in b) equal the exponent p, which contains information on the critical nucleus size. Additionally, from intersections of the linear functions with the y-axes, the attempt frequency for surface diffusion ν_0 can be determined.

Moreover, we analyze the dependency of the logarithm of N_{max} on the logarithm of the growth rate as plotted in Fig. 5.24 b). The data has been acquired for the first sub-ML regime of 6P and 6PF2 growth at T=60 °C. In analogy to the temperature variation, the data points of the growth rate variation experiments can also be fitted by a linear function. However, we note the larger scattering of the data points for both molecules compared to the temperature series. The slopes of the linear functions of the $\ln(N_{max})$ vs. $\ln(GR)$ plots yield the exponent p as can be easily deduced from equation (5.3). The evolution of the 6P data points in Fig. 5.24 b) can be assigned to a steeper slope of p=0.79 compared to p=0.63 in case of 6PF2. The higher p-value of 6P indicates a larger critical nucleus size i. However, the exact value of i depends on the nucleation regime, in which the growth proceeds. Below, we will discuss this in more detail.

Beside the slopes, we can also analyze the intersections of the linear fits with the y-axes. As a result, the attempt frequencies for surface ν_0 diffusion can then be determined as:

$$y_{0T} = \ln(\eta \cdot N_0) + p \cdot \ln\left(\frac{4}{N_0 \cdot \nu_0}\right) + p \cdot \ln(GR) \tag{5.4}$$

$$y_{0R} = \ln(\eta \cdot N_0) + p \cdot \ln\left(\frac{4}{N_0 \cdot \nu_0}\right) + E_{nuc} \cdot \frac{1}{kT}, \tag{5.5}$$

where y_{0T} is the y-intersection of the fit function of the T variation and y_{0R} is the y-intersection of the fit function of the GR variation. In the 1st ML we determine an attempt frequency for surface diffusion of $\nu_{0,6P}$=$9 \cdot 10^{15\pm0.5}\,\mathrm{s}^{-1}$ for 6P, while for 6PF2 the attempt frequency is about seven orders of magnitude higher, being $\nu_{0,6PF2}$=$9 \cdot 10^{22\pm0.5}\,\mathrm{s}^{-1}$. Importantly, the attempt frequencies determined independently from y_{0T} and y_{0R} match very well for both molecules. This underlines the consistency of the fit model. The evaluated values of ν_0 for both molecules differ strongly from typical values for atoms, which are around $10^{13}\,\mathrm{s}^{-1}$. A larger ν_0 for organic molecules is expected though, because of the increased degrees of freedom of the spatially extended organic molecules. For instance, the evaluated value of $\nu_{0,6P}$ is in good agreement with the published value of $2 \cdot 10^{17\pm0.5}\,\mathrm{s}^{-1}$ from a study of 6P growth on mica.[22] The attempt frequency of 6PF2 is, however, much larger, yet it is in the range of the attempt frequency for surface diffusion of PTCDI$-C_8$, which was determined to be approximately $10^{20\pm3}\,\mathrm{s}^{-1}$ in section 4.1, and it is also close to a ν_0=$10^{25}\mathrm{s}^{-1}$ as determined from desorption experiments for 6P on Au (111).

5.4.5 Discussing the molecular in-plane diffusion

In the following, we combine the results on the in-plane morphology evolution. We apply nucleation theory in different regimes to discuss the critical nucleus sizes, energetic barriers for surface diffusion and the in-plane diffusivities of 6P and 6PF2.

The exponent p and the nucleation energy E_{nuc}, which have been deduced above, contain information of growth quantities such as the critical nucleus size i, the energetic barriers for diffusion E_d, desorption E_a and binding E_i of a growing molecular thin film. The exact mathematical correlations depend, however, on the nucleation regime. In section 4.1.6, we discussed several regimes, which have been so far used in literature to describe the nucleation behavior of various organic molecules. For convenience we show here Fig. 4.8 b) again, which gives a summary of the definitions of p and E_{nuc} in the different regimes. Nevertheless, we refer to section 4.1.6 for detailed definitions of the terms and the concepts behind the regimes.

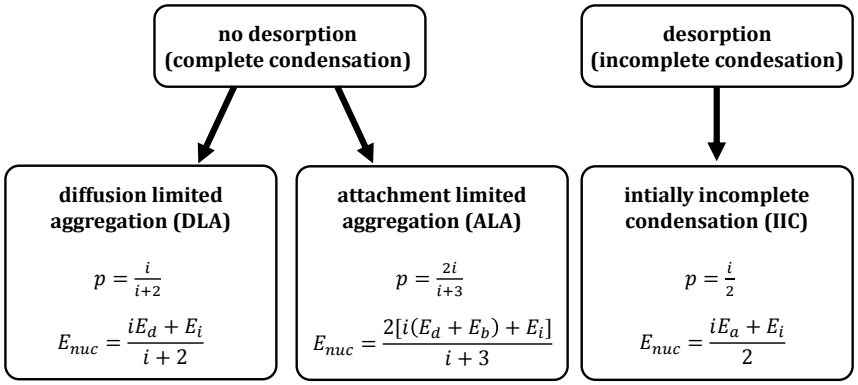

Figure 5.25: Summary of the definitions of E_{nuc} and p in different nucleation regimes.

From the anti-Bragg growth oscillations we can conclude that desorption of molecules does not play a role neither for the growth of 6P nor for 6PF2. We follow this directly from the positions of the minima and maxima of the oscillations, which indicate the completion of a ML growth. Independent of the substrate temperature, the 1st ML is closed after approximately the same molecular exposure, see Fig. 5.18. If desorption played a significant role, we would need a longer molecular exposure to complete the ML at a higher temperature, since desorption is a thermally activated process. This is not the case here, thus we conclude that the nucleation of both molecules proceeds in complete condensation with a zero or insignificantly low desorption.

For complete condensation, the diffusion-limited aggregation (DLA) is the so-far most applied nucleation regime.[22,25,132] As given in Fig. 5.25, in DLA the exponent p equals $i/(i+2)$. Assuming DLA, we find a critical nucleus size of i=8 for 6P and i=3 for 6PF2. For 6PF2 no data on critical nucleus sizes has been published so far. In contrast, for 6P grown on oxidized silicon surfaces at similar substrate temperatures and deposition rates, Lorbek *et al.* determined a substantially lower critical nucleus size of i=1-2.[133] Indeed, the here obtained value of i=8 for 6P is rather high - even in comparison to other organic molecules, where i is typically in the range of 2-5.[25,31,33,135] We note, however, that in the study of Lorbek *et al.* the 6P island density at 100 °C is smaller by a factor of approximately 400 compared to our value and still 50 times smaller than in the study of Yang *et al.*[132], although both studied 6P growth on oxidized silicon surfaces at growth parameters comparable to our study. Apparently, the substrate preparation, which is different in these studies, has a crucial effect on the nucleation. Therefore, simple direct comparisons of the growth-relevant pa-

rameters have always to be performed with regard to the experimental circumstances.

Concerning the nucleation energy, in the DLA regime, E_{nuc} depends on the energetic barrier for surface diffusion E_d, the binding energy E_i of a critical nucleus of size i and the size of the critical nucleus, as summarized in Fig. 5.25. A separation of the contributions of the two energies to the nucleation energy is extremely challenging. However, for the case of 6P, Potocar *et al.* published values of 6P binding energies E_i as a function of the critical island size. The values were obtained as a result of a molecular dynamics simulation.[22] The calculations revealed energetic differences for cluster configurations of lying down molecules and upright standing molecules. Furthermore the 6P (001) surface was used as a substrate, so that the obtained values can only be considered as rough estimations when applied to 6P on silicon oxide. Based on the work of Potocar *et al.*, for a critical nucleus size of i=8, E_i takes a value of 4.9 eV (for the more stable lying down configuration of the molecules). Assuming this, we determine a 6P diffusion barrier E_d=$((i+2) \cdot E_{nuc} - E_i)/i$ of 0.22 eV in the 1st ML. This value is about an order of magnitude higher than the E_d of 0.02 eV given in ref. [39] for the 6P diffusion on mica surfaces. However, compared to E_d's of other organic molecules, the here obtained value for 6P fits very well. Exemplary, an E_d of 0.54 eV has recently been determined for the diffusion of C_{60} on C_{60} and also for disc-like molecules diffusion barriers ranging from 0.57 to 0.74 eV have been reported.[34,213]

We further estimate E_d for 6PF2. From Figs. 5.24 a) and b), we determined a 0.1 eV larger nucleation energy of 6PF2 in comparison to 6P and a critical nucleus size of about 3. Since no data is available for the binding energy of 6PF2, for a first estimation, we can assume the E_i of a 6PF2 trimer to be essentially equal to the binding energy of a 6P trimer due to the close similarity of the molecules. Using the values from ref. [22], the binding energy of a 6P trimer is approximately 1.5 eV. With this assumption we calculate an E_d of 0.78 eV for 6PF2 in the 1st ML, which is about 3.5 times 6P the value. A larger diffusion barrier for 6PF2 is reasonable, since it may account for the observed nucleation of smaller islands and thus higher island densities. Evidently, our assumption of an equal trimer binding energy of 6P and 6PF2 does not necessarily has to be true. Varying the value of E_i, we find larger diffusion barriers for smaller 6PF2 binding energies. In contrast, higher binding energies would yield lower E_d's. In particular, we find that to achieve the same range of E_d for 6PF2 as for 6P, an E_i of about 3 eV would be needed, which is double the value of 6P. Such a value for E_i would be much larger than trimer binding energies reported in the literature for other molecules. For example, the E_i of pentacene is

about 1 eV,[23] which is in the same range as reported for 6P. We therefore consider a trimer binding energy of 3 eV as rather unlikely. Thus, our data analyzed in the framework of DLA indicate that in the 1st ML the diffusion barrier of 6PF2 is higher compared to 6P.

$$\frac{D_{6PF2}}{D_{6P}} \approx \underbrace{\frac{\upsilon_{0,6PF2}}{\upsilon_{0,6P}}}_{\approx 10^7} \cdot \exp\left(\frac{\overbrace{E_{d,6P} - E_{d,6PF2}}^{= -0.56\ \text{eV}}}{kT}\right)$$

T[°C]	D_{6PF2}/D_{6P}
60	0.03
80	0.10
100	0.27
130	1.00

Figure 5.26: Comparing the diffusivity of 6P and 6PF2 at different substrate temperatures by using the above deduced values for ν_0 and E_d.

In addition to E_d we have to consider the attempt frequencies ν_0 for surface diffusion to get a more complete understanding of the in-plane morphology. The molecular diffusivity D, describing the in-plane molecular motion, depends on both quantities:

$$D \propto \nu_0 \cdot \exp\left(\frac{-E_d}{kT}\right).$$

Taking into account the several orders of magnitude larger attempt frequency of 6PF2, the diffusivity of 6P has not necessarily to be larger, as the smaller E_d may suggest. However, comparing D of both molecules, we find that in the studied temperature range, the 6PF2 diffusivity lower than that of 6P apart from the highest temperature T=130 °C, where both values equalize as summarized in Fig. 5.26. The lower 6PF2 diffusivities at lower substrate temperatures are in good qualitative agreement with the higher island densities observed in the 1st ML, see Fig. 5.24. We also note the agreement of the trend of the observed decreasing differences of the island densities with increasing substrate temperature, see Fig. 5.24, with the trend for the calculated diffusivities.

The complex pathways relating the experimental observables E_{nuc}, p and ν_0 with the 1st ML diffusivities in the framework of DLA, are comprehensively summarized in Fig. 5.27.

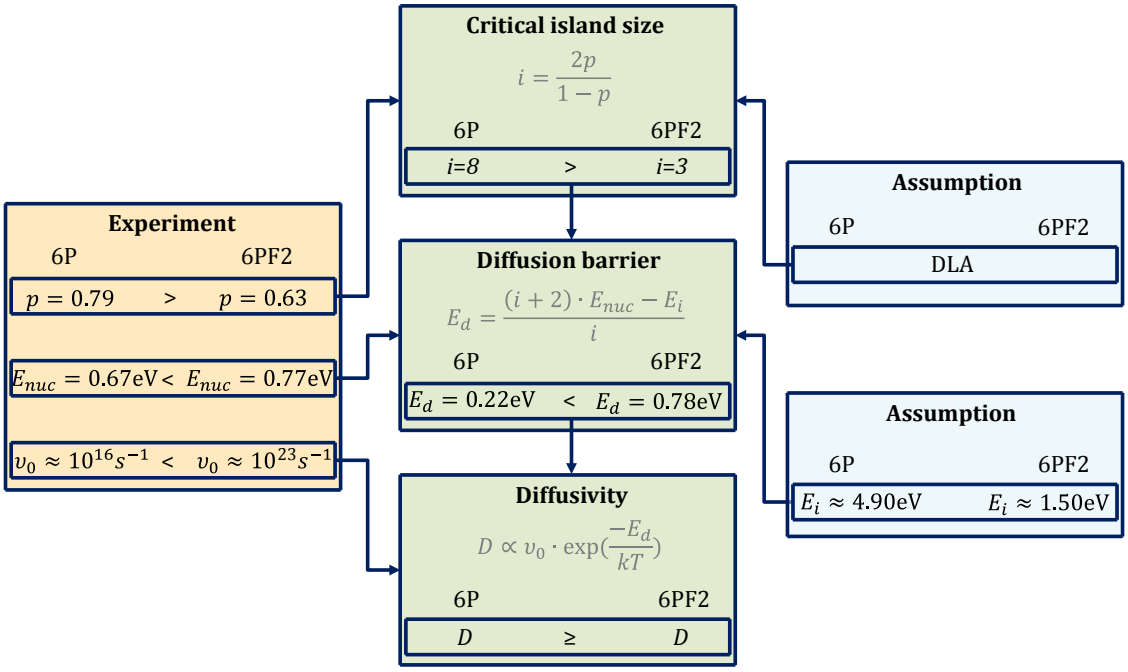

Figure 5.27: Summary of the pathways, which relate the experimental observables with the deduced sub-ML in-plane diffusivities of 6P and 6PF2.

After discussing just the first sub-ML growth, we now turn to the 2nd ML. As evaluated from Fig. 5.24 a), the nucleation energy of both molecules shows only a slight increase in the 2nd ML and is essentially equal to the value in the 1st ML. At the same time, we observe a smaller island density for both molecules in the 2nd ML. This points towards an improved diffusivity in the 2nd ML, which may be connected with a decrease of E_d, as we have shown for the case of PTCDI−C_8. Note, however, that since we observe a different y_{0T}, ν_0 may also change in the 2nd ML and therefore account for an enhancement of the diffusivity. However, the exact values of E_d and ν_0 depend on the unknown critical island sizes in the 2nd ML. Continuing to assume the DLA regime, a decrease of E_d under preservation of the size of E_{nuc} is only possible if the critical nucleus size i and therefore E_i changes. According to the definition $E_{nuc} = (iE_d + E_i)/(i+2)$, we can conclude that i has to increase in such a case.

Although DLA is the established standard model to describe molecular nucleation, recently other, more complex models have been used for a description of organic thin film growth. An example is the attachment limited aggregation (ALA) regime, which was firstly applied to organic molecules in ref. [47]. The corresponding definitions of E_{nuc} and p are given in Fig. 5.25. Basically ALA is very similar to DLA, with the main difference that molecular attachment to islands is hampered in ALA by an additional attachment barrier energy E_b. Although ALA was initially

developed for inorganic atom growth,[214] this additional barrier may account for the increased complexity of organic growth. In particular, diffusing molecules may need to reorient in order to attach to an island, which decreases the attachment probability and is included in the barrier E_b. A further difference is that in DLA the exponent p, i.e., the slope in $\ln(N_{max})$ vs. $\ln(GR)$ plots, is limited to values $1/3< p <1$, as follows from the definition. ALA, however, can describe experiments, where p ranges between 0.5 and 2. Consequently, experiments with $p >1$ can not be described by DLA, and ALA can be a suitable model for such cases. Here, p is about 0.7 or 0.8 and the model choice is therefore not unambiguous. Unfortunately, to our knowledge no values of E_b for organic systems have been reported so far, which makes any estimations difficult. This aspect might therefore be an interesting topic for future investigations. Considering multilayer growth, we assume that the attachment barrier will probably stay constant as a function of the film thickness, since E_b is based on intermolecular interactions. Comparing the 1st and 2nd ML nucleation of 6P and 6PF2 within ALA, we therefore conclude that an additional E_b can not explain the observation of a decreasing island density under a preservation of the nucleation energy in the 2nd ML. Thus, similar arguments as given for the DLA regime, would have to be used to describe the finding. We finally note that by assuming ALA, we would evaluate lower critical nucleus sizes, i.e., i_{6P}=3 and i_{6PF2}=1.

A third nucleation regime, which has recently been developed, is the hot precursor (HP) model. In DLA and ALA the incoming molecules are assumed to completely dissipate their kinetic energy and adopt the substrate temperature when adsorbing at the surface. However, this has not to be the case and the HP regime introduces two further parameters to account for initially hot molecules on the surface that diffuse faster for a short time after adsorption. These parameters are the energy dissipation coefficient κ and the the molecular temperature T_i, which differs from the substrate temperature T_s.[48] The nucleation theory equation is thus slightly modified in the HP regime:

$$N_{\max} \propto \left(\frac{4 \cdot GR}{N_0 \cdot \nu_0}\right)^p \cdot \exp\left(\frac{E_{nuc}}{k \cdot (T_i - \kappa \cdot (T_i - T_s))}\right). \tag{5.6}$$

In ref. [48], where the HP regime was introduced, p and E_{nuc} are given identical to the ALA model. The dissipation coefficient κ has a strong influence on the maximum island density. Briefly discussing the HP model for the case of PTCDI−C_8 growth in section 4.1, we found indications of a changing κ in the 1st and 2nd ML. This may be related to differences between adsorption on a hard substrate material and on

soft molecular islands. This aspect may also play a role here and partially influence the island densities in different MLs. However, due to the increased numbers of parameters, significantly more data are required for an analysis in the framework of the HP regime.

5.4.6 Discussing the molecular interlayer diffusion

We now will use the above findings on the in-plane morphology and diffusivity in the DLA regime, as summarized in Fig. 5.27, to discuss the out-of-plane morphology of 6P and 6PF2 films. In particular, we will focus on the interlayer transport. In accordance with the in-plane diffusivity, the step-down diffusivity S can be defined as[26]:

$$S \propto \nu_s \cdot \exp(-E_{ES}/kT), \tag{5.7}$$

with ν_s being the attempt frequency for step-down diffusion and E_{ES} being the Ehrlich-Schwoebel barrier for step-down motion. Our aim is to analyze differences in E_{ES} and ν_s of 6P and 6PF2. To do so, we introduce the quantity α for 6P and and 6PF2, which is the quotient of the step-down diffusivity S and the in-plane diffusivity D and, in case of 6P, reads as:

$$\alpha_{6P} = \frac{S_{6P}}{D_{6P}} = \frac{\nu_{s,6P}}{\nu_{0,6PF2}} \cdot \exp\left(\frac{-(E_{ES,6P} - E_{d,6P})}{kT}\right). \tag{5.8}$$

Due to the temperature-dependency of S and D, we define α_{LT} for T_{LT}=60 °C and α_{HT} for T_{HT}=130 °C for 6P and 6PF2, respectively. We determine the ratio of these values as follows:

$$\gamma_{LT} = \frac{\alpha_{6PF2,LT}}{\alpha_{6P,LT}} = \frac{S_{6PF2,LT}}{S_{6P,LT}} \cdot \frac{D_{6P,LT}}{D_{6PF2,LT}}, \tag{5.9}$$

$$\gamma_{HT} = \frac{\alpha_{6PF2,HT}}{\alpha_{6P,HT}} = \frac{S_{6PF2,HT}}{S_{6P,HT}} \cdot \frac{D_{6P,HT}}{D_{6PF2,HT}}. \tag{5.10}$$

We can correlate ΔE_{ES}=($E_{ES,6P} - E_{ES,6PF2}$) with γ_{LT}, γ_{HT} and ΔE_d=($E_{d,6PF2} - E_{d,6P}$) by equalizing eqs. (5.9) and (5.10) and inserting the definitions for S and D:

$$\frac{1}{\gamma_{LT}} \cdot \exp\left(\frac{\Delta E_{ES} + \Delta E_d}{kT_{LT}}\right) = \frac{1}{\gamma_{HT}} \cdot \exp\left(\frac{\Delta E_{ES} + \Delta E_d}{kT_{HT}}\right) \tag{5.11}$$

$$\Delta E_{ES} = \frac{\ln(1/\gamma_{LT}) - \ln(1/\gamma_{HT})}{\beta_{HT} - \beta_{LT}} - \Delta E_d, \tag{5.12}$$

with $\beta_{LT} = 1/kT_{LT}$ and $\beta_{HT} = 1/kT_{HT}$. Further, if inserting eq. (5.12) into eq. (5.10), the ratio $\nu_{s,6P}/\nu_{s,6PF2}$ can be written as (we again use the definitions of S and D):

$$\frac{\nu_{s,6P}}{\nu_{s,6PF2}} = \frac{1}{\gamma_{HT}} \cdot \frac{\nu_{0,6P}}{\nu_{0,6PF2}} \cdot \exp((\Delta E_{ES} + \Delta E_d) \cdot \beta_{HT}). \tag{5.13}$$

From the discussion of the in-plane diffusion constants, we have deduced ΔE_d=0.56 eV, $\nu_{0,6P}/\nu_{0,6PF2}$=10^{-7}s^{-1} as well as $D_{6P,LT}/D_{6PF2,LT} \approx$33 and $D_{6P,HT}/D_{6PF2,HT} \approx$1 in the 1st ML. Although each of these values may change in higher MLs, we can use the 1st ML values to understand their general influence on ΔE_{ES} and $\nu_{s,6P}/\nu_{s,6PF2}$. The resulting, relevant equations then read as:

$$\gamma_{LT} = \frac{S_{6PF2,LT}}{S_{6P,LT}} \cdot 33 \tag{5.14}$$

$$\gamma_{HT} = \frac{S_{6PF2,HT}}{S_{6P,HT}} \cdot 1 \tag{5.15}$$

$$\Delta E_{ES} = \frac{\ln(1/\gamma_{LT}) - \ln(1/\gamma_{HT})}{\beta_{HT} - \beta_{LT}} - 0.56\,\text{eV} \tag{5.16}$$

$$\frac{\nu_{s,6P}}{\nu_{s,6PF2}} = 10^{-7} \cdot \exp((\Delta E_{ES} + 0.56\,\text{eV}) \cdot \beta_{HT}). \tag{5.17}$$

As evident from eqns. (5.14)-(5.17) γ_{LT} and γ_{HT} determine the differences in the Ehrlich-Schwoebel barriers and the attempt frequencies for step-down diffusion. Unfortunately, it is not trivial to determine their exact values and theoretical input, e.g. in the form of molecular dynamics or KMC simulations,[34] would be of great advantage. Nevertheless, we can discuss the ratios of the step-down diffusivities S at the two different temperatures.

In the case of γ_{LT}, one may argue that the lower 6PF2 roughness at T_{LT}=60 °C must correspond to an enhanced step-down diffusivity S_{6PF2} and therefore the ratio $S_{6PF2,LT}/S_{6P,LT}$ would be larger than unity. However, this simple argument does not take into account the island size, which plays an important role in the interlayer transport. For instance, Rosenfeld *et al.* showed that layer-by-layer growth of one and the same material can be significantly improved if just the island density is increased at otherwise equal growth parameters (in particular, at the same substrate temperature).[215] On top of smaller islands more molecules can reach the edges of the

island, thereby increasing the total number of attempts to jump down and increasing the downward transport. Thus, a lower S can still be compatible with smoother films if more molecules reach the island edges. However, in a more detailed discussion, given in appendix A.2, we show that at T_{LT} and also at T_{HT} most probable a lower number of 6PF2 molecules will reach the island edges compared to 6P. We derive the relations $S_{6PF2,LT}/S_{6P,LT} > 1$ and $S_{6PF2,HT}/S_{6P,HT} > 1$, corresponding to γ_{LT} >33 and γ_{HT} >1.

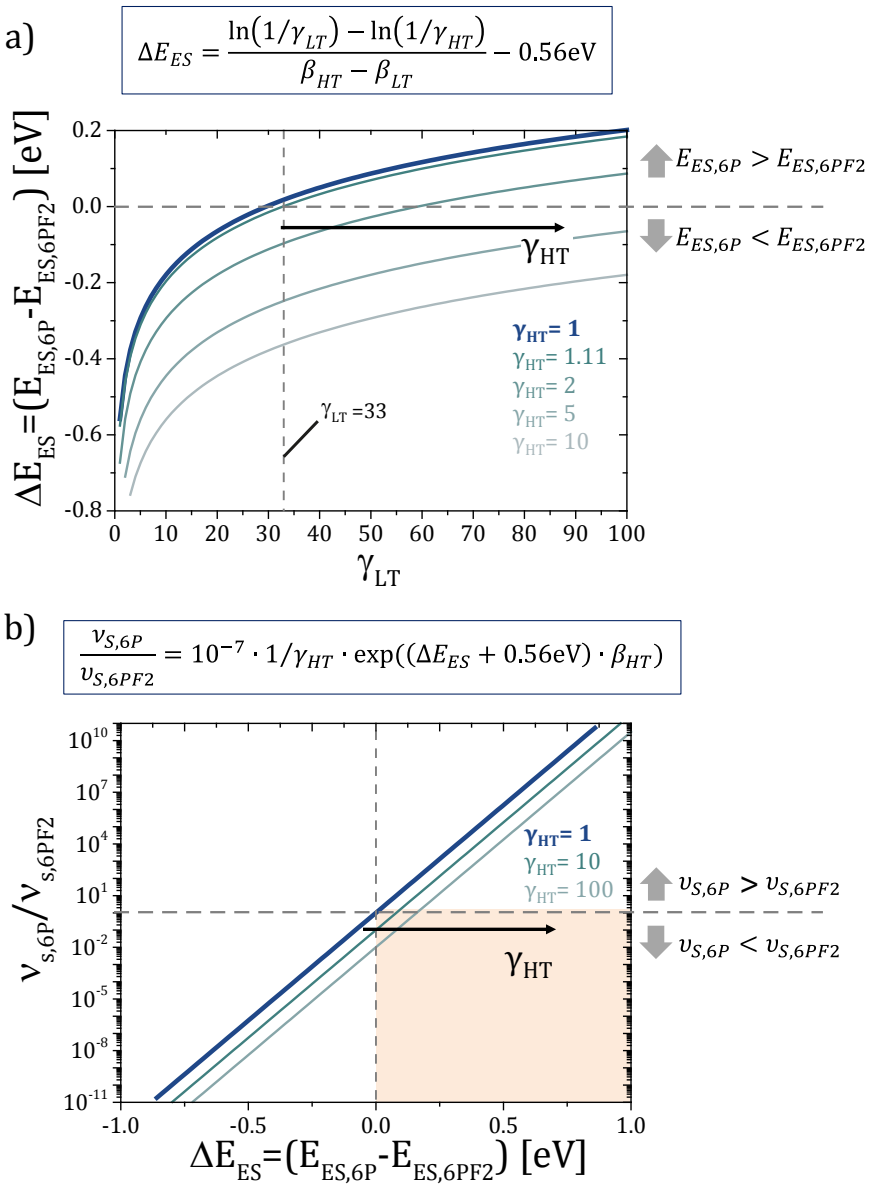

Figure 5.28: a) The dependency of differences of the Ehrlich-Schwoebel energies ΔE_{ES}=$E_{ES,6P} - E_{ES,6PF2}$ on γ_{LT}. b) The dependency of the quotient of the attempt frequencies for step-down diffusion of 6P and 6PF2 as a function of ΔE_{ES}.

With the knowledge of γ_{HT} >1, we can investigate its influence on ΔE_{ES} as a function of γ_{LT} by applying eq. (5.16). The corresponding graphs are plotted in Fig. 5.28 a). We observe that with increasing γ_{HT} the intersection of the curve with ΔE_{ES}=0 shifts to larger γ_{LT} values. If γ_{HT} lies in the range of 1$\leq \gamma_{HT} \leq$1.11, this intersection point is at $\gamma_{LT} \leq$33 as shown in Fig. 5.28 a). Consequently, for this range, we can follow $E_{ES,6P} > E_{ES,6PF2}$ due to our constraint of γ_{LT} >33. This, in turn, would imply that fluorination of 6P decreases the Ehrlich-Schwoebel barrier. For higher γ_{HT} values such statement is not necessarily true and it will depend on the exact quantity of γ_{LT}, as shown in Fig. 5.28 a).

By plotting eq. (5.17) in Fig. 5.28 b), we find that the situation $E_{ES,6P} > E_{ES,6PF2}$ can be described with $\nu_{s,6P} > \nu_{s,6PF2}$ (case 1) and, as labeled by the reddish square, with $\nu_{s,6P} < \nu_{s,6PF2}$ (case 2). For some combinations of γ_{LT} and γ_{HT}, a situation of $E_{ES,6P} < E_{ES,6PF2}$ can occur, which would imply that fluorination raises the Ehrlich-Schwoebel barrier. Applied to our experimental data, a situation of $E_{ES,6P} < E_{ES,6PF2}$ will correspond to $\nu_{s,6P} < \nu_{s,6PF2}$ (case 3). The last case, which would in principle be coherent with our experiments, is $E_{ES,6P} = E_{ES,6PF2}$ and $\nu_{s,6P} < \nu_{s,6PF2}$ (case 4). This case results from the intersection points of the curves in Fig. 5.28 b) with the y-axis at ΔE_{ES}=0. Case 4 would therefore imply that fluorination does not affect Ehrlich-Schwoebel barrier, but only increases the attempt frequency for step-down diffusion. Note, that the case of $E_{ES,6P} = E_{ES,6PF2}$ and $\nu_{s,6P} = \nu_{s,6PF2}$, i.e. a zero effect of fluorination on the step-down diffusivity S, is in contradiction with the constraint of γ_{LT} >33 and can be therefore excluded, as can be followed from Figs. 5.28 a) and b).

Concluding, we have discussed quantities such as island densities, edge arrival rates, in-plane diffusivities, attempt frequencies for step-down diffusion and Ehrlich-Schwoebel barriers, which all influence the interlayer transport in organic films. We have demonstrated the complexity and the interdependency of all involved parameters, which makes a detailed quantification of the effect of fluorination on E_{ES} and ν_s difficult. We derive four cases for the balances of ΔE_{ES}=$E_{ES,6P} - E_{ES,6PF2}$ and $\nu_{s,6P}/\nu_{s,6PF2}$, which would be coherent with the deduced in-plane diffusivities and our experimental observations of the film roughness at different substrate temperatures. The most important result is that all of these cases show that fluorination alters the molecular step-down diffusivity S, which is a quantity combining E_{ES} and ν_s.

5.4.7 Summary

One of the unique features of functional organic molecules is their chemical flexibility which allows to tune the chemical structure of molecules. In our study we analyzed of the effect of chemical tuning on the molecular self-assembly. We compared the growth on silicon oxide of the well-studied, rodlike and symmetric molecule *para*-sexiphenyl (6P) and its chemically tuned derivative 6PF2, which is synthesized through a substitution of two hydrogen atoms by two fluorine atoms at one molecular end of 6P. The fluorine atoms induce asymmetry and a local dipole moment. The changed electrostatics may influence the molecular interactions during self-assembly, so chemical tuning of molecules may become a new steering parameter in thin film growth.

Utilizing a specially developed silane coating of the tips, *ex situ* AFM measurements revealed that 6P and 6PF2 assemble in compact, roundish islands consisting of almost upright standing molecules. The shape of the islands does not change under a variation of the substrate temperature T in the range of 60-130 °C and of the growth rate GR in the range of 0.01 to 0.3 nm/min. Comparing the evolution of the out-of-plane morphology, we find remarkable differences in the growth of the molecules. As deduced from *in situ* real-time XRR growth oscillations, fluorination induces a significant film smoothing. In particular, at the lowest studied substrate temperature of T=60 °C, the roughness of 6PF2 films is about two times lower than for 6P films of comparable film thickness of about 4 ML. In Fig. 5.29 we give a sketch, summarizing the growth modes of 6P and 6PF2.

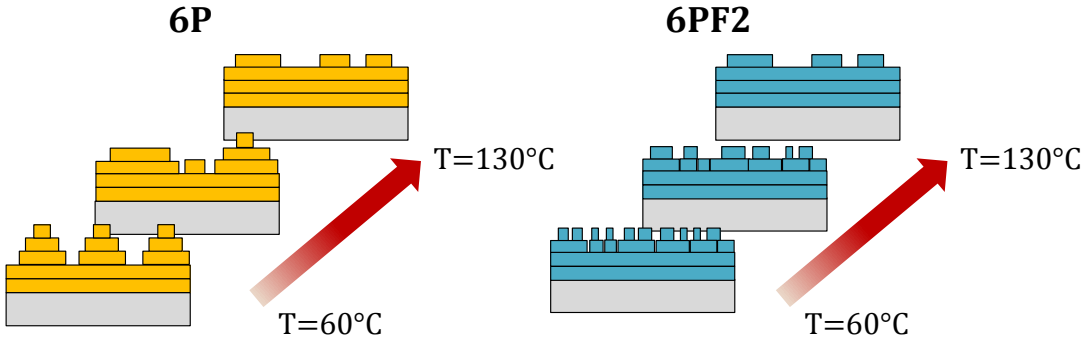

Figure 5.29: Summarizing sketches of the growth modes of 6P and 6PF2 as a function of substrate temperature. At T=60 °C the roughness of 6PF2 films is significantly lower and we observe larger island densities compared to 6P films. The latter show a strong temperature dependency and at T=130 °C almost identical island densities and film roughnesses are found for 6P and 6PF2 films.

The observed smoother 6PF2 growth is a result of an increased interlayer transport, which we quantify from a rate equation model, used to fit the growth oscillations. We further compare decisive energetic barriers describing the nanoscale processes of in-plane and step-down diffusion. For the in-plane diffusion, we evaluated the scaling of the maximum island densities N_{max} as a function of T and GR in the framework of nucleation theory. We determined a 0.1 eV larger nucleation energy E_{nuc} and a remarkable 7 orders of magnitude larger attempt frequency for surface diffusion ν_0 of 6PF2 in the 1st ML compared to 6P. Therefore the evaluated ν_0 $\approx 10^{23} s^{-1}$ for 6PF2 is in the range of the ν_0 for PTCDI$-C_8$, as deduced in the last chapter, while ν_0 6P is in agreement with 6P values reported for the diffusion on mica.[22] The exponent p describing the scaling of N_{max} with GR is smaller for 6PF2, which indicates a smaller critical island size i of 6PF2. Combining these values within the diffusion-limited aggregation (DLA) regime, we estimate a diffusion barrier of $E_{d,6P}$=0.22 eV and $E_{d,6PF2}$=0.78 eV. This entails a lower 6PF2 diffusivity at lower substrate temperatures and explains the larger N_{max} compared to 6P.

Further, we discuss the impact of fluorination on the step-down diffusivity by taking into account the geometrical factor of island sizes, as well as the evaluated E_d, ν_0 and i. We derive the complex influence of these quantities on the Ehrlich-Schwoebel barrier E_{ES} and the attempt frequencies for step-down diffusion ν_s. Although an unambiguous determination of the exact values E_{ES} and ν_s was not possible within the limits of our experiments, we demonstrate that fluorination impacts not only the in-plane, but also the step-down diffusivity S, which comprises the two quantities.

In general, smooth thin films - as achieved here for 6PF2 - are highly desired for technological applications. Our study shows that chemical tuning is an effective tool to meet these demands. From a more fundamental point of view, the induced impact of chemical modification on in- and out-of-plane nanoscale processes comprises a so far poorly studied facet of molecular growth. The rich variety of possible chemical modifications gives reasons to assume that other aspects of growth and structure formation such as the molecular orientation or crystallinity, may be rationally influenced by chemical tuning.

6 Summary

This thesis dealt with analyzing and rationally influencing organic thin film growth. By applying a combination of *ex situ* microscopy and modern real-time *in* and *ex situ* X-ray scattering experiments our aim was to increase the understanding of film formation through unravelling nanoscale kinetics and to examine chemical tuning as a steering mechanism of organic growth. The following will briefly summarize the main results of our work.

6.1 Understanding organic thin film nucleation and growth by using X-ray scattering

The self-assembly of organic molecules into functional materials is decisively influenced by processes at the nanoscale such as nucleation, stable cluster formation and diffusion. The challenging quantification of these processes is a key for an enhanced understanding of the macroscopic thin film structure. Our growth study of the prototypical rod-like organic semiconductor PTCDI$-C_8$ in section 4.1 delivers novel stimuli to this research topic, because we give an overview over several growth models applied beyond the common limits of 1st monolayer (ML) growth and also compare relatively new, advanced X-ray methods with established AFM[1] techniques.

Studying the evolution of PTCDI$-C_8$ nucleation beyond the 1st ML

We examined the remarkable layer-dependent growth behavior of PTCDI$-C_8$ as a function of substrate temperature T and growth rate GR by applying an **innovative combination of simultaneous *in situ* real-time synchrotron XRR and GISAXS [2] measurements**. This allowed us to monitor in parallel the evolution of the in- and out-of-plane morphology of the growing film, see Fig. 6.1. From

[1] AFM - atomic force microscopy
[2] XRR - X-ray reflectivity, GISAXS - grazing incidence small angle X-ray scattering

XRR growth oscillations at the anti-Bragg point we deduced a persistent, quasi layer-by-layer growth of the molecules, comparable to the growth of the related PTCDI−C_{13}. Rate-equation model fits of the growth-oscillations highlighted differences in the growth of the 1st and 2nd ML manifesting themselves in a 1.4 times smaller molecular adsorption probability on the silicon oxide substrate. Further differences in the 1st and upper ML growth constitute in a transition of the island shapes from roundish to rectangular as we uncovered by complementary *ex situ* AFM measurements. These measurements further showed that PTCDI−C_8 assembles in islands of almost standing upright molecules.

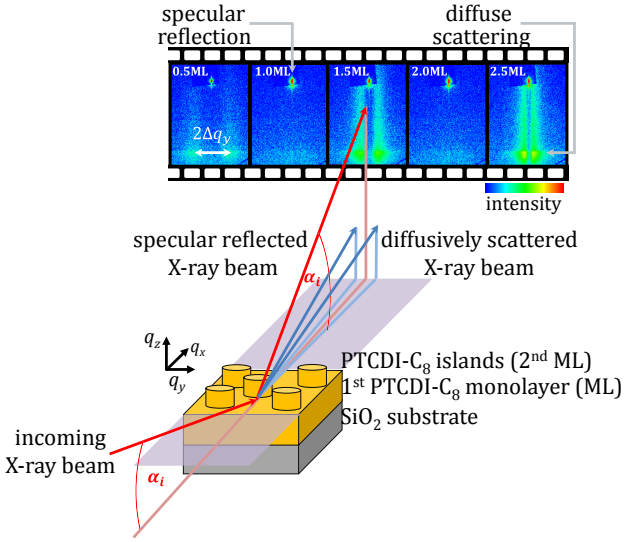

Figure 6.1: Advanced experiment setup at the P03 beamline at PETRAIII, DESY, Hamburg allowing for the simultaneous *in situ* real-time measurement of the in- and out-of-plane morphology by studying the diffuse GISAXS and the specular XRR, respectively.

With regard to the in-plane morphology, from the complementary GISAXS measurements, we evaluated a steadily decreasing molecular island density with film thickness. This result agreed with established AFM measurements. From the data, we precisely determined the maximum island densities N_{max} in each ML and analyzed their T and GR dependency in the framework of nucleation theory. Importantly, while many similar studies restrict their analysis of the nucleation to the 1st (sub-)ML regime and the most frequently used DLA[3] model, we intentionally went beyond the 1st ML and discussed various state-of-the-art models to rationalize multilayer growth behavior. In agreement with nucleation theory, we found a linear dependency of $\ln(N_{max})$ vs. $1/\mathrm{kT}$ and $\ln(N_{max})$ vs. $\ln(GR)$, which allowed us to determine a

[3]DLA - diffusion-limited aggregation

Table 6.1: Summary of the evaluated nucleation energies and critical island sizes in the first two MLs.

	Nucleation energy E_{nuc}	**Scaling factor** p	**critical island size** i	
			DLA	ALA
1st ML	532±52 meV	0.50±0.05	2	1
2nd ML	460±28 meV	0.53±0.05	2	1

nucleation energy E_{nuc} of about 532 meV in the 1st and 460 meV in the 2nd ML. At the same time, the scaling factor p, as deduced from the $\ln(N_{max})$ vs. $\ln(GR)$ behavior, equals 0.5 in both MLs pointing towards an equal critical nucleus size i in both MLs, see Table 6.1. Further, we evaluated an essentially equal attempt frequency for surface diffusion in both MLs of $\nu_0 \approx 10^{19-20}\,\mathrm{s}^{-1}$. Within the DLA and ALA[4] models, the combination of these values permits us to determine a significant decrease of the diffusion barrier energy E_d by 140 meV in the 2nd ML. This goes along with an at least 25 times increased diffusivity in the studied temperature range. However, the size of i differs between the DLA and ALA model, suggesting i=2 in DLA and i=1 in ALA, thus 3 or, respectively, 2 molecules form a stable island. We also discuss our results within the hot precursor model and find indications for a faster thermalization of the molecules in the 2nd ML, which is so far a poorly studied aspect in organic thin film growth.

By extending the standard nucleation analysis beyond the 1st ML we could therefore associate the layer-dependent growth behavior with a significant diffusivity increase in the 2nd ML. Experimentally, we demonstrated good agreement of the XRR-GISAXS data with established AFM techniques. Combined with the *in situ* real-time capability of XRR-GISAXS this showcases the potential of this comparatively new technique for growth studies.

The results of our study on the multilayer growth of PTCDI−C_8 have been published in ref. [118].

[4]ALA - attachment-limited aggregation

6.2 Chemical tuning as a control parameter for tailoring organic growth

In chapter 5 we exploited new steering mechanisms of organic film growth. Our approach is based on the chemical tuneability of organic molecules allowing for substitutions of single atoms or functional groups. In particular, we focused on the comparison of the growth of the well-known *para*-sexiphenyl molecule (6P) and its chemically tuned derivatives 6PF4 and 6PF2. The latter are synthesized by fluorination of either four hydrogen at both termini (6PF4) or two hydrogen atoms at one molecular end (6PF2), see Fig. 6.2. These apparently small changes of the chemical structure of 6P, alter the chemical environment and induce local dipole moments. Further, in the case of 6PF2, the molecular symmetry is reduced. **In our experiments we demonstrate a strong influence on molecular nucleation and diffusion and a desired and significant impact of fluorination on the film roughness and phase purity**. Our results establish selective chemical tuning of functional organic molecules as a viable strategy to design crystalline organic layers with thin film morphologies as demanded for well-defined interfaces in opto-electronic applications.

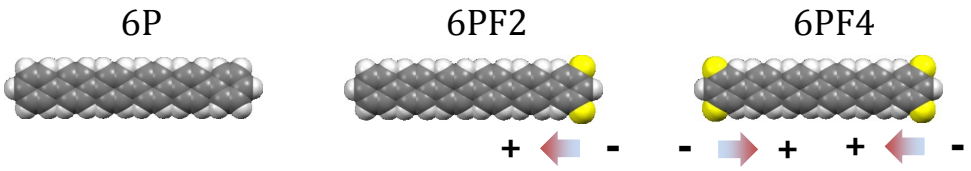

Figure 6.2: Sketch of 6P, composed of six linked phenyl rings, and its fluorinated derivatives, which have been used to study the influence of chemical tuning on molecular thin film growth. The arrows indicate the local dipole moments induced by fluorination.

Symmetrical fluorination of *para*-sexiphenyl to induce film smoothing and crystal phase purification

In section 5.3 we examined the growth of the symmetrical 6P and 6PF4 molecules on the anisotropic ZnO (10$\bar{1}$0) surface, where alternating rows of Zn and O ions create an electrostatic surface field, which is a striking difference to isotropic substrates such as silicon oxide. Both molecules have been deposited by OMBD in ultra-high vacuum conditions at room-temperature and a fixed growth rate of about 0.1 nm/min.

6P and 6PF4 molecules grow in an almost upright standing orientation and in a highly crystalline fashion as evidenced in post-growth XRD[5] measurements by Bragg reflections of at least the 5th order. In the case of 6P, we further clearly distinguish a Bragg peak splitting into two contributions of equal intensity, which we attribute to a simultaneous growth of the known β- and γ-phases. Interestingly, so far, the γ-phase of 6P has been reported only for growth at elevated temperatures on glass, so the ZnO surface induces γ-phase growth at lower temperatures. In contrast, 6PF4 grows in a single crystal phase. Thus, **we conclude that by symmetrical fluorination of 6P we induced phase pure growth**.

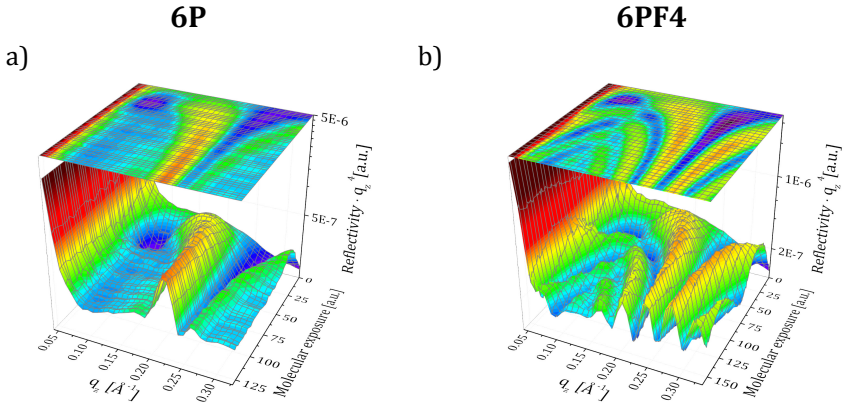

Figure 6.3: *In situ* real-time XRR measurements of growing a) 6P and b) 6PF4 films allow us to evaluate in detail the evolution of the out-of-plane morphologies. In the case of 6PF4, well-distinguishable Kiessig and Laue oscillations indicate a significantly smoother film surface compared to 6P.

The growth dynamics of both films have been evaluated from synchrotron *in situ* real-time XRR measurements. This allowed us to monitor in detail the evolution of film roughness and crystallinity with high precision and over a broad q_z-range, see Fig. 6.3. The data was fitted by independently applying the Parratt formalism and rate-equation models, which were simultaneously appplied to growth oscillations at multiple q_z points beyond a single anti-Bragg point. Both approaches yield very good agreement with the data and quantitative consistency among each other on surface coverages, ML thicknesses and film roughness. We find the 6PF4 growth proceeding via a surface induced phase with a **steadily increasing tilt angle** up to $\sim 27\,^\circ$ within the first three MLs. In contrast, the tilt angle of 6P equals $\sim 17\,^\circ$ and $0\,^\circ$ in the β- and γ-phases, see Fig. 6.4.

[5] XRD - X-ray diffraction

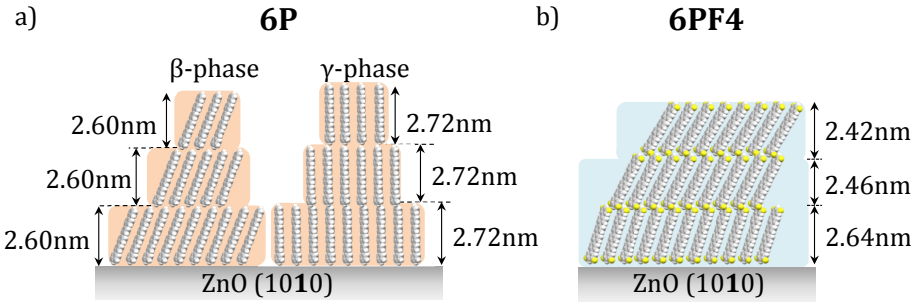

Figure 6.4: Sketch of the evaluated differences in the growth of a) 6P and b) 6PF4 on ZnO (10$\bar{1}$0) surfaces.

Further, we find a **strong impact of fluorination on the film roughening**. We evaluate that 6PF4 growth proceeds in a 2d layer-by-layer mode, while the unsubstituted 6P follows a rough 3d growth mode. We demonstrate that fluorination induces film smoothing by a factor of 2 if comparing 5 ML thick films. The described differences in the molecular tilt angle and the crystal phase purity can be regarded as factors supporting the film smoothing. The larger tilt angle of 6PF4 in the upper MLs can be correlated with a lower Ehrlich-Schwoebel-barrier, which enhances the downward mass transport. Further the increased density of grain boundaries of the polymorphic 6P growth can increase the number of nucleation sites and therefore induces roughening.

Our comparative study on the growth of 6P and 6PF4 has been published in ref. [104].

Impact of asymmetrical fluorination of *para*-sexiphenyl on nucleation and film smoothing

In section 5.4 we investigated the differences in the growth of the asymmetrical 6PF2 and its symmetrical unsubstituted counterpart 6P on silicon oxide substrates at different substrate temperatures and growth rates. In the sub-ML regime, we unravel close similarities in the growth of both films from *ex situ* AFM measurements. The molecules grow in roundish islands and adopt an almost upright standing molecular orientation. In contrast, at higher film thickness the film morphologies differ substantially. For nominally 5 ML thick films we observe **terraced mounds in the case of 6P, while 6PF2 preserves a rather smooth morphology**.

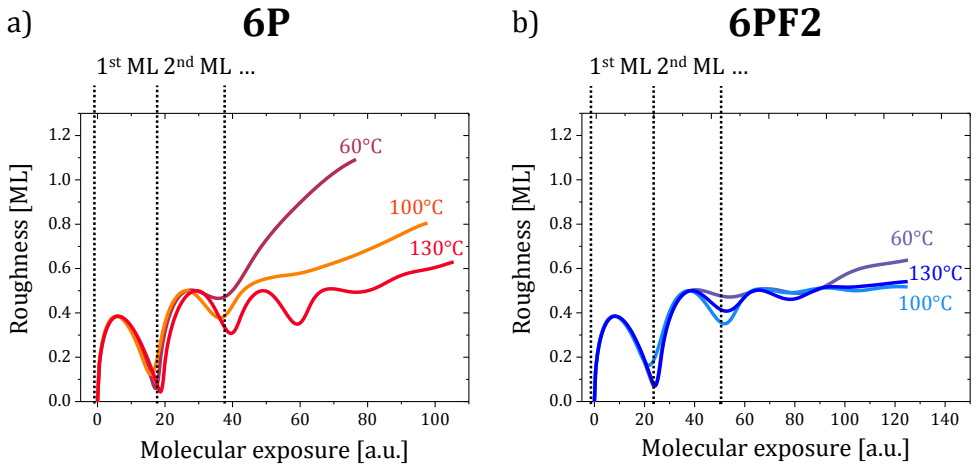

Figure 6.5: The evolution of the film roughnesses of a) 6P and b) 6PF2 illustrates the beneficial effect of fluorination and substrate temperature on film roughness.

Rate equation model fits to XRR growth oscillations at the anti-Bragg point at three different substrate temperatures allow us to quantitatively compare the evolution of 6P and 6PF2 film roughnesses. At the lowest probed substrate temperature of 60 °C **fluorination enhances film smoothness by a factor of 2**, see Fig. 6.5. While for 6PF2 the roughness is almost independent of the substrate temperature, a 70 °C increase halves the roughness of ca. 4 ML thick 6P films. This indicates that the beneficial effect of fluorination on film smoothing can be outbalanced by thermally-induced nucleation processes, such as in-plane and step-down diffusivities. However, achieving film smoothing at lower processing temperatures as realized through fluorination is preferred from an energetic viewpoint.

Studying the dependency of the maximum island densities on substrate temperature and growth rate with AFM, we evaluate nucleation energies, diffusion barriers and critical island sizes. The nucleation energy of 6PF2 is in the first two MLs 100 meV higher than of 6P, while the growth rate scaling factor p is smaller, indicating a smaller critical nucleus size for 6PF2. A significant difference is found from the evaluation of the attempt frequencies for surface diffusion ν_0. For 6P we find a ν_0 of $10^{16}\,\mathrm{s}^{-1}$ (which is in the range of literature values for 6P diffusion on mica), while a remarkable seven orders of magnitude larger value for the attempt frequency is found for 6PF2 (which is in the range, but still larger than our observed ν_0 for PTCDI$-C_8$, yet is in the region of ν_0=$10^{25}\mathrm{s}^{-1}$ as found for 6P on the (111) surface of Au). Assuming the DLA model and equal binding energies for 6P and 6PF2 (per molecule), we find a diffusion barrier E_d of 220 meV for 6P and 780 meV for 6PF2 in the 1st ML. The combination of E_D and ν_0 results in a higher 6P

in-plane diffusivity at lower temperatures and rationalizes the lower island density of 6PF2 at smaller temperatures, see Fig. 6.6. Furthermore, we determine a critical island size i of 8 for 6P, i.e., nine molecules will form a stable island, while i=3 for 6PF2.

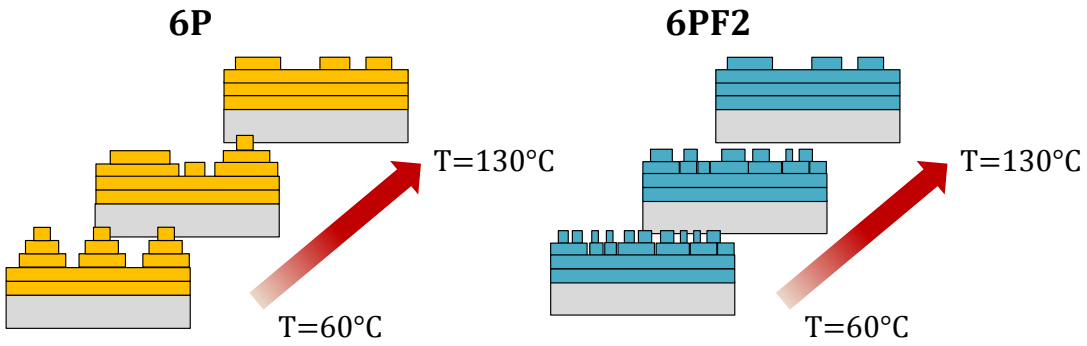

Figure 6.6: Summarizing sketch on the differences in the growth of a) 6P and b) 6PF2 on silicon oxide.

Aiming to understand the molecular interlayer transport, we derived a formalism for the non-trivial interplay of the in-plane diffusivity D, the island densities N, the critical island sizes i and the step-down diffusivity S. The latter comprises the Ehrlich-Schwoebel barrier E_{ES} and the attempt frequency for step-down diffusion ν_s. Based on our derivations of D, i and N, **we demonstrate that the selective chemical substitution of only two atoms has a significant effect on both the in- and out-of-plane growth nanoscale kinetics resulting in an optimization of film roughnesses on the meso- or macroscopical length scale**.

A manuscript on these results is in preparation.

7 List of publications

1. **Diffusion and nucleation in multilayer growth of PTCDI−C_8 studied with *in situ* X-ray growth oscillations and real-time small angle X-ray scattering.** A. Zykov, S. Bommel, C. Wolf, L. Pithan, C. Weber, P. Beyer, G. Santoro, J.P. Rabe, S. Kowarik. The Journal of Chemical Physics, 146, 052803, (2017).

2. **Chemical tuning of *para*-sexiphenyl: The role of fluorination in controlling nanoscale processes during thin-film growth.** A. Zykov, T. Lingenberg, D. Rathke, L. Pithan, C. Weber, Y. Garmshausen, P. Schäfer, S. Hecht, S. Kowarik. In preparation.

3. **Controlling the growth mode of *para*-sexiphenyl (6P) on ZnO by partial fluorination.** M. Sparenberg (*), A. Zykov (*), P. Beyer, L. Pithan, C. Weber, Y. Garmshausen, F. Carlà, S. Hecht, S. Blumstengel, F. Henneberger, and S. Kowarik, Phys. Chem. Chem. Phys. 16, 26084 (2014). **** equal contribution***

4. **Tuning the Work Function of Polar Zinc Oxide Surfaces using Modified Phosphonic Acid Self-Assembled Monolayers.** I. Lange, S. Reiter, M. Pätzel, A. Zykov, A. Nefedov, J. Hildebrandt, S. Hecht, S. Kowarik, C. Wöll, G. Heimel, D. Neher. Advanced Functional Materials, 24, 44, 7014-7024, (2014).

5. **Dynamic substrate temperature modulations for enhanced layer-by-layer growth in organic thin films.** L. Pithan, L. Bogula, G. Duva, A. Zykov, A. Gerlach, F. Schreiber, S. Kowarik. In preparation.

6. **Direct photo-alignment and patterning of molecular semiconductors.** L. Pithan, P. Beyer, L. Bogula, A. Zykov, J. Rawle, C. Nicklin, A. Opitz, S. Kowarik. Submitted, (2016).

7. **Cooperative Switching in Nanofibers of Azobenzene Oligomers.** C. Weber, T. Liebig, M. Gensler, A. Zykov, L. Pithan, J. Rabe, S. Hecht, D. Bléger, S. Kowarik. Nature Scientific Reports, 6, 25605, (2016).

8. **Structure of *p*-sexiphenyl nanocrystallites embedded in ZnO.** H. Kirmse, M. Sparenberg, A. Zykov, S. Sadofev, S. Kowarik and S. Blumstengel. Crystal Growth and Design, 16 (5), pp 2789-2794, (2016).

9. **Thermally driven smoothening of molecular thin films: Structural transitions in n-alkane layers studied in real-time.** L. Pithan, E. Meister, C. Jin, C. Weber, A. Zykov, K. Sauer, W. Brütting, H. Riegler, A. Opitz, S. Kowarik. The Journal of Chemical Physics, 143, 164707, (2015).

10. **Light Controls Polymorphism in Thin Films of Sexithiophene.** L. Pithan, C. Cocchi, H. Zschiesche, C. Weber, A. Zykov, S. Bommel, S.J. Leake, P. Schäfer, C. Draxl, and S. Kowarik, Crystal Growth and Design, 15, 1319 (2015).

11. **Lattice Matching as the Determining Factor for Molecular Tilt and Multilayer Growth Mode of the Nanographene Hexa-peri-hexabenzocoronene.** P. Beyer, T. Breuer, S. Ndiaye, A. Zykov, A. Viertel, M. Gensler, J. P. Rabe, S. Hecht, G. Witte, S. Kowarik. ACS Applied Materials & Interfaces, 6 (23), pp 21484-21493, (2014).

12. **Deposition of very thin uniform indium sulfide layers over metallic nano-rods by the Spray-Ion Layer Gas Reaction method.** G. Genduso, R. Inguanta, C. Sunseri, S. Piazza, C. Kelch, R. Sáez-Araoz, A. Zykov, C.-H. Fischer. Thin Solid Films, 548, 91-97, (2013).

13. **Spray pyrolysis of barrier layers for flexible thin film solar cells on steel.** S. Gledhill, A. Zykov, N. Allsop, T. Rissom, J. Schniebs, C. A. Kaufmann, M. Lux-Steiner, C.-H. Fischer. Solar Energy Materials and Solar Cells, 95, 2, (2011).

14. **The role of the spray pyrolysed Al_2O_3 barrier layer in achieving high efficiency solar cells on flexible steel substrates.** S. Gledhill, A. Zykov, T. Rissom, R. Caballero, C. A. Kaufmann, C.-H. Fischer, M. Lux-Steiner, V. Efimova, V. Hoffmann, S. Oswald. Applied Physics A, 104, 407, (2011).

Contributed conference talks:

1. **Frühjahrstagung der Deutschen Physikalischen Gesellschaft, Regensburg 2016:** Coverage dependent nucleation of PTCDI$-C_8$ studied complementary by AFM and *in situ* real time XRR and GISAXS.

2. **Spring Meeting of the Material Research Society, San Francisco 2015:** *In situ* characterization of Organic-Inorganic Hybrid Structures: Fluorination for the Chemical Tuning of Structure and Morphology in *para*-Sexiphenyl (6P) Growth on ZnO.

3. **Bruker AFM workshop, Berlin 2015:** How to exploit ScanAsyst-based PeakForce Tapping as a complementary imaging mode for the investigation of organic thin-film growth.

4. **Photonics group seminar, Berlin 2015:** Chemical tuning of *para*-sexiphenyl (6P): How functional groups influence the molecular self-assembly of 6P derivatives on SiOx and non-polar ZnO.

5. **Frühjahrstagung der Deutschen Physikalischen Gesellschaft, Berlin 2015:** *In situ* characterization of organic-inorganic hybrid structures: fluorination for the chemical tuning of structure and morphology in *para*-sexiphenyl (6P) growth on ZnO.

6. **Frühjahrstagung der Deutschen Physikalischen Gesellschaft, Dresden 2014:** The role of a molecular dipole in thin-film growth kinetics: *In situ* X-ray studies of 6P and 6P-3,5-F2 on SiO_2.

7. **HIOS Young researcher workshop, Wittensee 2013:** Understanding molecular growth kinetics and designing structures for HIOS.

8. **HIOS Young researcher workshop, Wittensee 2012:** *In-situ* and real-time x-ray scattering for HIOS.

Poster presentations:

1. **HIOS symposium, Berlin 2015:** Chemical tuning as a new parameter to control HIOS thin-film growth.

2. **BESSY user meeting, Berlin 2013:** X-ray spectromicroscopy analysis of organic solar energy materials at the nanoscale: Domain dimensions, in-plane orientation and chemical contrast.

3. **Frühjahrstagung der Deutschen Physikalischen Gesellschaft, Regensburg 2013:** Domain dimensions, in-plane orientation and chemical contrast at the nanoscale: X-ray spectromicroscopy studies of organic molecules and polymers.

8 Acknowledgements

At this point I'd like to express my gratitude to the people who helped and supported me during my time as a PhD student. Without the excellent teamwork and collaboration the whole work with the challenging experiments and the interesting results would have been so much harder and so much less fun.

My primary acknowledgements go to my supervisor Prof. Stefan Kowarik, who is the person who made the whole PhD project possible. Amongst many other things, I wish to thank for his endless support, the always-open doors, the inspiring scientific discussions and for the positive atmosphere in our working group.

Next, I would like to thank Prof. Stefan Hecht and Yves Garmshausen for their invaluable contribution to the chemical tuning project. Without their huge commitment and their incredible skills in organic synthesis, the fluorinated molecules would probably still not exist. In this context, I am more than pleased to thank Dr. Sylke Blumstengel, Mino Sparenberg and Dr. Holm Kirmse, with whom I had the pleasure to cooperate on the chemical tuning project. The fruitful discussions and experimental contributions had a significant positive influence on our common work. This thesis would be incomplete without the extremely rich information yielded from AFM measurements, which were not possible without the kind support of Prof. Jürgen P. Rabe and his working group, from which I want to pick out Dr. Nikolai Severin and in particular Manuel Gensler, who introduced me to the AFM and was inexpressibly helpful and supportive with any kind of problem or question. In the context of experimental methods, I can not be thankful enough to Dr. Peter Schäfer for his support with the lab-based X-ray source and for sharing his detailed knowledge on X-ray crystallography. Further, I am thankful to Dr. Gonzalo Santoro and Prof. Stephan Roth from the P03 beamline at DESY, Hamburg and Dr. Francesco Carlà and Dr. Roberto Felici from the ID03 beamline at the ESRF, Grenoble for their help and stimulating discussions during and after the experiments. I am also very happy and thankful to have had the opportunity to discuss the complexity of organic thin-film growth with Dr. Karol Palczynski and Dr. Nicola Kleppmann, who provided me with many valuable and new insights. I further acknowledge Hans Kirschner, Dirk Rathke and Tina Lingenberg for being

excellent bachelor students.

My huge gratitude goes to my close colleagues Paul Beyer, Dr. Sebastian Bommel, Linus Pithan and Dr. Christopher Weber. I very much appreciate that I always could count on you and I am thankful for all the long tours to the various european synchrotrons and conferences, the everyday support and the fun we had together. You were a great team!

Finally, I am deeply thankful to the very special people whose love, motivation, patience and trust in me brought me here: Lucynka, my parents and my whole family! Thank you very much!

Selbständigkeitserklärung

Ich erkläre, dass ich die Dissertation selbständig und nur unter Verwendung der von mir angegebenen Hilfsmittel gemäß § 7 Abs. 3 der Promotionsordnung der Mathematisch-Naturwissenschaftlichen Fakultät, veröffentlicht im Amtlichen Mitteilungsblatt der Humboldt-Universität zu Berlin Nr. 126/2014 am 18.11.2014, angefertigt habe.

Berlin, den

Hilfsmittel Zusätzlich zu den in Literaturverzeichnis Quellen wurden folgende Softwarepakete verwendet: Origin Pro 9.1, Microsoft Office 2013, ChemSketch, Mercury 3.3, Mendeley, Mathematica 9, Gwyddion 2.35, Python 2.7.3, Adobe Illustrator CC, Gimp 2

A Appendix

A.1 Determining the coverage of ultrathin organic films on polar ZnO by XRR

Here we present the results of a collaboration with Ilja Lange [1] *et al.* on the formation of dipolar self-assembled monolayers (SAMs) on polar ZnO (0001)-Zn surfaces, which tune the work function of ZnO. We used XRR measurements to contribute to the understanding of the homogeneity and ordering of ultra-thin SAM films, which is difficult to access by other techniques. However, this knowledge is essential for both the correct calculation of the work function shift induced by the different SAMs, and for proving the reliability and accuracy of the deposition method. In the presented study, we measured SAM-thicknesses of less than 10 Å on polar ZnO surfaces. The results of this work have been published in ref. [216].

In hybrid opto-electronic devices the inorganic semiconductor usually plays the role of an electrode, while the organic part is commonly the active layer. One of the most prominent transparent inorganic electrode material is indium tin oxide (ITO).[217,218] However, due to the limited supply of indium and therefore high costs, in recent years alternative materials and, in particular, ZnO get a large attention. A disadvantage of ZnO is, however, its workfunction of about 4.3 eV, which lies in the energy gap between the highest occupied molecular orbital (HOMO) and the lowest unoccupied molecular orbital (LUMO) of common organic semiconductors.[219–222] An effective charge injection is thus hindered by an energetic barrier and this fact deteriorates the efficiency of a device. However, the work function can be tuned by the deposition of thin dipolar layers.

In the here presented study benzylphosphonic acid (BPA) and its chemical derivatives, with dipole moments of different strength see Fig. A.1, have been used to tune the ZnO work function.[216] A linear relationship of the dipole moment strength and the ZnO work function shift in a range of 1.5 eV was found. However, since the

[1] Institute of Physics and Astronomy, university of Potsdam

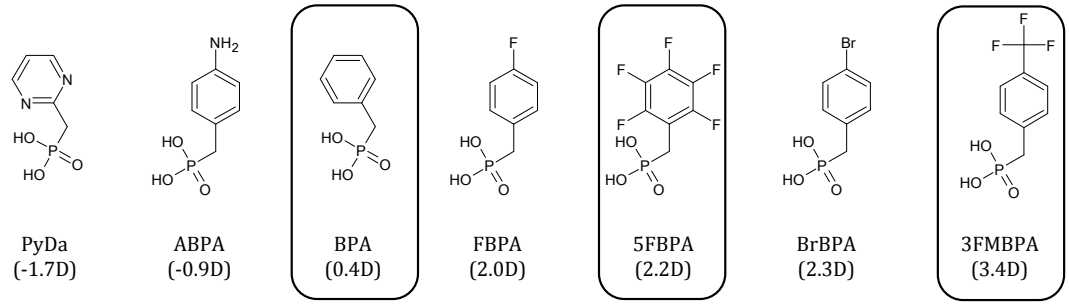

Figure A.1: The chemical structure and the abbreviated names of the benyzlphosphonic acid SAMs used to tune the workfunction of ZnO. In brackets the dipole moment of the head groups is shown, pointing -if negative- towards the phosphonic acid with the negative pole. The here studied SAMs are highlighted by a rectangle.

induced work function shift depends on the density of the SAM layer, knowledge on the film homogeneity is essential. A challenging and non-trivial question is therefore, whether the SAMs anchor as a monolayer or as a multilayer on the ZnO surface. Considering the SAM inclination angle of about 47 ° found by near-edge X-ray absorption fine structure (NEXAFS, for details s. refs.[223,224]) measurements, a SAM monolayer height of below 10 Å is estimated. However, with NEXAFS an unambiguous determination of the coverage and the number of closed MLs was not possible. XRR was therefore used to measure the layer thickness with high precision. The measurements were performed using the *EFG* diffractometer (s. section 3.2.5), under high-vacuum conditions (below 10^{-6} mbar) to avoid damage by ozone and at elevated substrate temperatures (T=100 °C) to minimize water adsorption on the sample.

In Fig. A.2 the X-ray reflectivity curves of three selected SAMs - BPA, 5FBPA and 3FMBPA - are shown. The edge of total reflection at about q_z=0.046 Å^{-1} closely matches the literature value for ZnO. We further observe the expected decaying Fresnel reflectivity curve and for larger q_z a slight oscillation in the reflectivity, the so called Kiessig fringes. As described in the previous sections, these fringes originate from interferences between reflections from the top and bottom interfaces of the SAM. The position of the fringe minimum is a measure for the SAM thickness and shifts towards smaller q_z values for larger layer thicknesses.

From the Parratt fits [2] to the measured XRR curves the values of SAM thickness and electron density are quantified. The fits were performed using an intentionally

[2]The XRR fits have been performed with the software *Parratt32*.

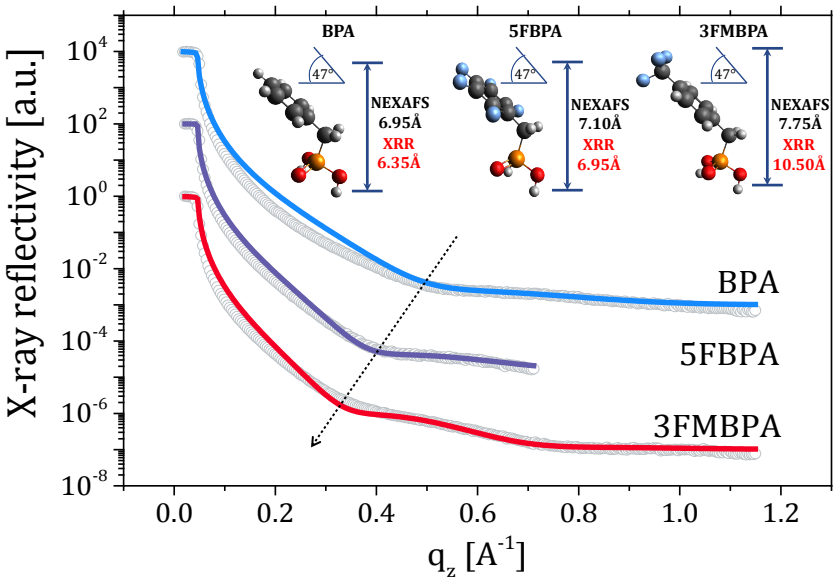

Figure A.2: XRR measurements of BPA, 5FBPBA and 3FMBPA on ZnO with the red lines showing the corresponding Parratt fit curves. The shift of the Kiessig fringe minimum towards smaller values of q_z with increasing SAM thickness is indicated by the arrow. The inset shows the calculated total SAM thickness based on the NEXAFS data and deduced from the XRR fits.

simple one layer model to reduce the number of free fit parameters. For BPA and 5FBPA the best fits were achieved by using the electron densities from the NIST data base[204], i.e. ρ_{BPA}=0.44 Å^{-3} and ρ_{5FBPA}=0.54 Å^{-3}. In the case of 3FMBPA, however, a two layer model was necessary to achieve a good fit. In a two layer model one separates the SAM into the head and the tail group with different electron densities, i.e. $\rho_{\mathrm{3FMBPA-head}}$=0.46 Å^{-3} and $\rho_{\mathrm{3FMBPA-tail}}$=0.36 Å^{-3}. Such a two layer approach is well-known in the literature[225] and is also motivated by the structure as shown in Fig. A.2.

The fit curves reproduce the position of the oscillation minimum well for each SAM. The values deduced for the thicknesses of BPA and 5FBPA are d_{BPA}=6.3 Å and d_{5FBPA}=6.85 Å, while the sum of the heights of the head and tail group of 3FMBPA results in a total thickness d_{3FMBPA}=10.5 Å. Therefore, the trend of BPA being the thinnest and 3FMBPA being the thickest layer is in accordance with the calculations based on the results of the NEXAFS measurements (s. inset of Figure A.2). Although the measured thicknesses do not perfectly match the calculated SAM heights, the XRR measurements confirm that the investigated molecules form homogeneous and closed layers on the ZnO surface with an average height of roughly one monolayer, i.e. no multilayers are observed.

A.2 Discussing the arrival rates of 6PF2 and 6P molecules at the respective island edges

This section is meant to support the analysis of the interlayer diffusion of 6P and 6PF2 molecules in section 5.4.6 of the thesis. We aim to compare the number of 6P and 6PF2 molecules, diffusing on top of a molecular island and arriving at the island edges. For our discussion here, we use various experimental quantities, which we evaluated in section 5.4. For convenience, we give here the set of equations, which are of interest for the below discussion:

$$\gamma_{LT} = \frac{S_{6PF2,LT}}{S_{6P,LT}} \cdot 33 \tag{A.1}$$

$$\gamma_{HT} = \frac{S_{6PF2,HT}}{S_{6P,HT}} \cdot 1 \tag{A.2}$$

$$\Delta E_{ES} = \frac{\ln(1/\gamma_{LT}) - \ln(1/\gamma_{HT})}{\beta_{HT} - \beta_{LT}} - 0.56\,\text{eV} \tag{A.3}$$

$$\frac{\nu_{s,6P}}{\nu_{s,6PF2}} = 10^{-7} \cdot \exp((\Delta E_{ES} + 0.56\,\text{eV}) \cdot \beta_{HT}). \tag{A.4}$$

We first want to discuss aspects indicating that at a substrate temperature of T_{LT}=60 °C a lower number of 6PF2 molecules reaches the island edges compared to 6P. For the ratio of the step-down diffusivities S of both molecules, this will imply $S_{6PF2,LT} > S_{6P,LT}$.

The first indication for the lower arrival rate of 6PF2 at step edges is its lower diffusion length, which we deduce to be 0.17 times the diffusion length of 6P by taking the square root of the diffusivities D_{6PF2}/D_{6P} (at T_{LT}). The lower diffusion length indicates that fewer molecules will reach the edges, but this effect may be outbalanced by the smaller 6PF2 island sizes at 60 °C compared to 6P. By using $N_{max} \propto \sqrt{1/r^2}$, with N_{max} being the maximum island density, we find that the mean radius r of 6PF2 islands equals 0.85 times the radius of 6P islands in the 1st ML. Thus, compared to 6P the radius of 6PF2 is reduced by less than the diffusion length. This might indicate that the smaller island size can not outbalance the lower diffusion lengths. Accordingly, less 6PF2 molecules would reach the island edges. However, we can not experimentally quantify the diffusion length and therefore we can not exclude that the lower 6PF2 diffusion length is still large enough, so that

all molecules reach the island edges. Though, referring to the deduced lower critical island size of 6PF2, we have shown that only four 6PF2 molecules are required to form a stable and immobile cluster, compared to nine 6P molecules. Thus, for a 6PF2 molecule diffusing towards the island edges the probability of being captured into an immobile island is higher. Therefore, it seems improbable that more 6PF2 molecules will reach the island edge compared to 6P, which points towards a lower molecular density at the 6PF2 island edges. If fewer molecules arrive at the edges, the observed smoother 6PF2 growth at T_{LT} can only be explained if $S_{6PF2,LT} > S_{6P,LT}$. This implies that the lower number of 6PF2 molecules arriving at the edge are more efficiently transported downward at 60 °C. Consequently, $\gamma_{LT} > 33$ as follows from eq. (A.1). We summarized our arguments in a diagram tree in Fig. A.3 a).

Focusing on the higher temperature, we can directly exclude a higher arrival rate of 6PF2 at the island edges compared to 6P. This follows from the observation of equal island densities, similar diffusivities and film roughnesses at T=130 °C. Further, if the arrival rates were equal, $S_{6PF2,HT}/S_{6P,HT}$ has be unity, otherwise the film roughnesses would differ. However, due to the smaller critical nucleus size, we rather suspect a lower number of 6PF2 molecules at the island edges for the same reasons as given above for the T_{LT} case. Consequently we deduce $\gamma_{HT} = S_{6PF2,HT}/S_{6P,HT} > 1$. In Fig. A.3 b) we summarize our reasoning.

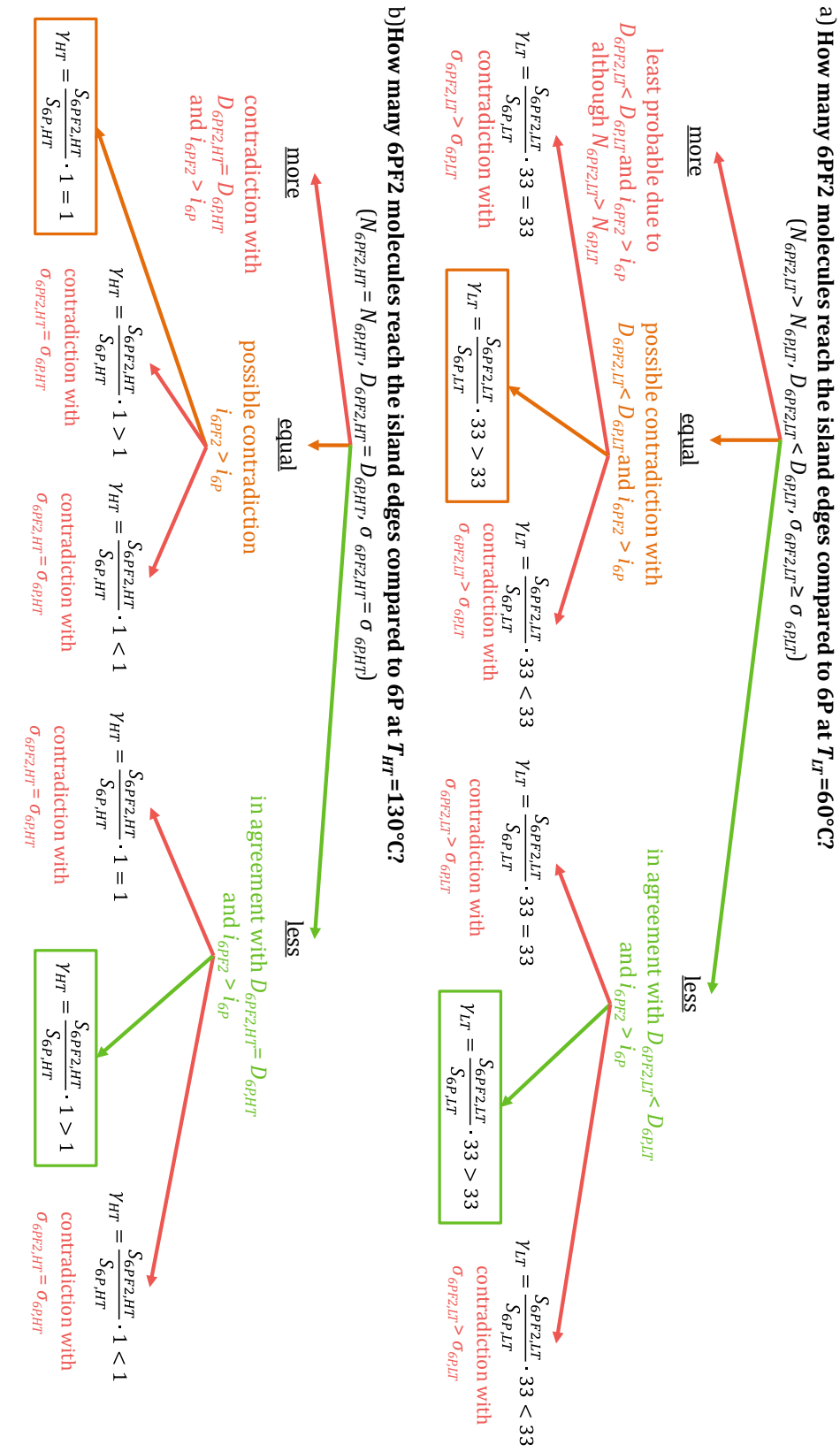

Figure A.3: Discussing the molecular density at island edges of 6P and 6PF2 films at T=60 °C and T=130 °C. D gives the diffusivity, N the island density and σ the film roughness.

List of Figures

Bibliography

[1] D. M. Chapin, C. S. Fuller, and G. L. Pearson. A New Silicon p-n Junction Photocell for Converting Solar Radiation into Electrical Power. *Journal of Applied Physics*, 25(5):676, 1954. doi: 10.1063/1.1721711.

[2] M. A. Green, K. Emery, Y. Hishikawa, W. Warta, and E. D. Dunlop. Solar cell efficiency tables (version 47). *Progress in Photovoltaics: Research and Applications*, 24(1):3–11, jan 2016. doi: 10.1002/pip.2728.

[3] L. S. McDowell. The Fluorescence and Absorption of Anthracene. *Physical Review (Series I)*, 26(2):155–168, feb 1908. doi: 10.1103/PhysRevSeriesI.26.155.

[4] H. Minemawari, T. Yamada, H. Matsui, J. Tsutsumi, S. Haas, R. Chiba, R. Kumai, and T. Hasegawa. Inkjet printing of single-crystal films. *Nature*, 475(7356):364–367, jul 2011. doi: 10.1038/nature10313.

[5] Y. Diao, B. C.-K. Tee, G. Giri, J. Xu, D. H. Kim, H. A. Becerril, R. M. Stoltenberg, T. H. Lee, G. Xue, S. C. B. Mannsfeld, and Z. Bao. Solution coating of large-area organic semiconductor thin films with aligned single-crystalline domains. *Nature Materials*, 12(7):665–671, jun 2013. doi: 10.1038/nmat3650.

[6] U. Heinemeyer, A. Hinderhofer, M. I. Alonso, J. O. Ossó, M. Garriga, M. Kytka, A. Gerlach, and F. Schreiber. Uniaxial anisotropy of organic thin films determined by ellipsometry. *physica status solidi (a)*, 205(4):927–930, apr 2008. doi: 10.1002/pssa.200777765.

[7] G. Hlawacek and C. Teichert. Nucleation and growth of thin films of rod-like conjugated molecules. *Journal of physics. Condensed matter : an Institute of Physics journal*, 25(14): 143202, 2013. doi: 10.1088/0953-8984/25/14/143202.

[8] A. C. Mayer, A. Kazimirov, and G. G. Malliaras. Dynamics of Bimodal Growth in Pentacene Thin Films. *Physical Review Letters*, 97(10):105503, sep 2006. doi: 10.1103/PhysRevLett.97.105503.

[9] L. Pithan, C. Cocchi, H. Zschiesche, C. Weber, A. Zykov, S. Bommel, S. J. Leake, P. Schäfer, C. Draxl, and S. Kowarik. Light Controls Polymorphism in Thin Films of Sexithiophene. *Crystal Growth & Design*, 15(3):1319–1324, 2015. doi: 10.1021/cg501734w.

[10] M. Halik, H. Klauk, U. Zschieschang, G. Schmid, S. Ponomarenko, S. Kirchmeyer, and W. Weber. Relationship Between Molecular Structure and Electrical Performance of Oligothiophene Organic Thin Film Transistors. *Advanced Materials*, 15(11):917–922, jun 2003. doi: 10.1002/adma.200304654.

[11] J. A. Venables, G. D. T. Spiller, and M. Hanbucken. Nucleation and growth of thin films. *Reports on Progress in Physics*, 47(4):399–459, apr 1984. doi: 10.1088/0034-4885/47/4/002.

[12] Z. Zhang and M. G. Lagally. Atomistic Processes in the Early Stages of Thin-Film Growth. *Science*, 276(5311):377–383, apr 1997. doi: 10.1126/science.276.5311.377.

[13] H. Brune. Microscopic view of epitaxial metal growth: nucleation and aggregation. *Surface Science Reports*, 31(4-6):125–229, 1998. doi: 10.1016/S0167-5729(99)80001-6.

[14] T. Michely and J. Krug. *Islands, Mounds and Atoms*, volume 42 of *Springer Series in Surface Sciences*. Springer Berlin Heidelberg, Berlin, Heidelberg, 2004. ISBN 978-3-642-62237-3. doi: 10.1007/978-3-642-18672-1.

[15] H. Brune. Epitaxial Growth of Thin Films. In *Surface and Interface Science*, pages 421–492. Wiley-VCH Verlag GmbH & Co. KGaA, Weinheim, Germany, nov 2014. doi: 10.1002/9783527680566.ch20.

[16] F. Schreiber. Organic molecular beam deposition: Growth studies beyond the first monolayer. *physica status solidi (a)*, 201(6):1037–1054, may 2004. doi: 10.1002/pssa.200404334.

[17] S. Kowarik, A. Gerlach, and F. Schreiber. Organic molecular beam deposition: fundamentals, growth dynamics, and in situ studies. *Journal of Physics: Condensed Matter*, 20(18):184005, may 2008. doi: 10.1088/0953-8984/20/18/184005.

[18] D. Käfer, L. Ruppel, G. Witte, and C. Wöll. Role of Molecular Conformations in Rubrene Thin Film Growth. *Physical Review Letters*, 95(16):166602, oct 2005. doi: 10.1103/PhysRevLett.95.166602.

[19] S. Kowarik, A. Gerlach, S. Sellner, F. Schreiber, L. Cavalcanti, and O. Konovalov. Real-time observation of structural and orientational transitions during growth of organic thin films. *Physical Review Letters*, 96(12):1–4, 2006. doi: 10.1103/PhysRevLett.96.125504.

[20] S. Blumstengel, H. Glowatzki, S. Sadofev, N. Koch, S. Kowarik, J. P. Rabe, and F. Henneberger. Band-offset engineering in organic/inorganic semiconductor hybrid structures. *Physical chemistry chemical physics : PCCP*, 12(37):11642–11646, 2010. doi: 10.1039/c004944c.

[21] P. Beyer, T. Breuer, S. Ndiaye, A. Zykov, A. Viertel, M. Gensler, J. P. Rabe, S. Hecht, G. Witte, and S. Kowarik. Lattice Matching as the Determining Factor for Molecular Tilt and Multilayer Growth Mode of the Nanographene Hexa-peri-hexabenzocoronene. *ACS Applied Materials & Interfaces*, 6(23):21484–21493, 2014. doi: 10.1021/am506465b.

[22] T. Potocar, S. Lorbek, D. Nabok, Q. Shen, L. Tumbek, G. Hlawacek, P. Puschnig, C. Ambrosch-Draxl, C. Teichert, and A. Winkler. Initial stages of a para-hexaphenyl film growth on amorphous mica. *Physical Review B*, 83(7):1–10, 2011. doi: 10.1103/PhysRevB.83.075423.

[23] P. R. Ribič, V. Kalihari, C. D. Frisbie, and G. Bratina. Growth of ultrathin pentacene films on polymeric substrates. *Physical Review B*, 80(11):1–8, 2009. doi: 10.1103/PhysRevB.80.115307.

[24] S. Pratontep, M. Brinkmann, F. Nüesch, and L. Zuppiroli. Correlated growth in ultrathin pentacene films on silicon oxide: Effect of deposition rate. *Physical Review B*, 69(16):1–7, 2004. doi: 10.1103/PhysRevB.69.165201.

[25] T. V. Desai, E. R. Kish, A. R. Woll, and J. R. Engstrom. Hyperthermal growth of N,N'-ditridecylperylene-3,4,9,10-tetracarboxylic diimide on self-assembled monolayers: Adsorption dynamics and sub- and multilayer thin film growth. *Journal of Physical Chemistry C*, 115 (37):18221–18234, 2011. doi: 10.1021/jp204495u.

[26] K. Bromann, H. Brune, H. Röder, and K. Kern. Interlayer Mass Transport in Homoepitaxial and Heteroepitaxial Metal Growth. *Physical Review Letters*, 75(4):677–680, jul 1995. doi: 10.1103/PhysRevLett.75.677.

[27] M. Campione, S. Caprioli, M. Moret, and A. Sassella. Homoepitaxial Growth of α-Hexathiophene. *The Journal of Physical Chemistry C*, 111(34):12741–12746, aug 2007. doi: 10.1021/jp068616j.

[28] M. Einax, W. Dieterich, and P. Maass. Colloquium : Cluster growth on surfaces: Densities, size distributions, and morphologies. *Reviews of Modern Physics*, 85(3):921–939, jul 2013. doi: 10.1103/RevModPhys.85.921.

[29] A. Winkler. On the nucleation and initial film growth of rod-like organic molecules. *Surface Science*, 2016. doi: 10.1016/j.susc.2016.02.015.

[30] A. Picone, M. Riva, G. Fratesi, A. Brambilla, G. Bussetti, M. Finazzi, L. Duò, and F. Ciccacci. Enhanced atom mobility on the surface of a metastable film. *Physical Review Letters*, 113 (July):046102, 2014. doi: 10.1103/PhysRevLett.113.046102.

[31] B. Stadlober, U. Haas, H. Maresch, and A. Haase. Growth model of pentacene on inorganic and organic dielectrics based on scaling and rate-equation theory. *Physical Review B*, 74(16): 165302, oct 2006. doi: 10.1103/PhysRevB.74.165302.

[32] Y. Wu, T. Toccoli, N. Koch, E. Iacob, A. Pallaoro, P. Rudolf, and S. Iannotta. Controlling the Early Stages of Pentacene Growth by Supersonic Molecular Beam Deposition. *Physical Review Letters*, 98(7):076601, feb 2007. doi: 10.1103/PhysRevLett.98.076601.

[33] E. R. Kish, T. V. Desai, D. R. Greer, A. R. Woll, and J. R. Engstrom. Nucleation of diindenoperylene and pentacene at thermal and hyperthermal incident kinetic energies. *Journal of Vacuum Science & Technology A: Vacuum, Surfaces, and Films*, 33(3):031511, may 2015. doi: 10.1116/1.4916885.

[34] S. Bommel, N. Kleppmann, C. Weber, H. Spranger, P. Schäfer, J. Novak, S. Roth, F. Schreiber, S. Klapp, and S. Kowarik. Unravelling the multilayer growth of the fullerene C60 in real time. *Nature Communications*, 5:5388, 2014. doi: 10.1038/ncomms6388.

[35] G. Ehrlich and F. G. Hudda. Atomic View of Surface Self-Diffusion: Tungsten on Tungsten. *The Journal of Chemical Physics*, 44(3):1039, 1966. doi: 10.1063/1.1726787.

[36] R. L. Schwoebel and E. J. Shipsey. Step Motion on Crystal Surfaces. *Journal of Applied Physics*, 37(10):3682, 1966. doi: 10.1063/1.1707904.

[37] J. Krug. Four lectures on the physics of crystal growth. *Physica A: Statistical Mechanics and its Applications*, 313(1-2):47–82, oct 2002. doi: 10.1016/S0378-4371(02)01034-8.

[38] M. Fendrich and J. Krug. Ehrlich-Schwoebel effect for organic molecules: Direct calculation of the step-edge barrier using empirical potentials. *Physical Review B*, 76(12):121302, sep 2007. doi: 10.1103/PhysRevB.76.121302.

[39] G. Hlawacek, P. Puschnig, P. Frank, A. Winkler, C. Ambrosch-Draxl, and C. Teichert. Characterization of step-edge barriers in organic thin-film growth. *Science (New York, N.Y.)*, 321(5885):108–111, 2008. doi: 10.1126/science.1159455.

[40] J. E. Goose, E. L. First, and P. Clancy. Nature of step-edge barriers for small organic molecules. *Physical Review B - Condensed Matter and Materials Physics*, 81(20):10–12, 2010. doi: 10.1103/PhysRevB.81.205310.

[41] S. A. Burke, J. M. Mativetsky, S. Fostner, and P. Grütter. C60 on alkali halides: Epitaxy and morphology studied by noncontact AFM. *Physical Review B*, 76(3):035419, jul 2007. doi: 10.1103/PhysRevB.76.035419.

[42] S. A. Burke, J. M. Topple, and P. Grütter. Molecular dewetting on insulators. *Journal of Physics: Condensed Matter*, 21(42):423101, oct 2009. doi: 10.1088/0953-8984/21/42/423101.

[43] L. Sun, S. Berkebile, G. Weidlinger, G. Koller, M. Hohage, F. P. Netzer, M. G. Ramsey, and P. Zeppenfeld. Revealing the buried interface: para-sexiphenyl thin films grown on TiO2(110). *Physical Chemistry Chemical Physics*, 12(13):3141, 2010. doi: 10.1039/b922285e.

[44] S. Bommel, H. Spranger, C. Weber, N. Kleppmann, S. V. Roth, S. H. L. Klapp, and S. Kowarik. Thermally-activated post-growth dewetting of fullerene C 60 on mica. *physica status solidi (RRL) - Rapid Research Letters*, 9(11):646–651, nov 2015. doi: 10.1002/pssr.201510258.

[45] S. Bommel. *Unravelling nanoscale molecular processes in organic thin films*. PhD thesis, 2015.

[46] D. Walton. Nucleation of Vapor Deposits. *The Journal of Chemical Physics*, 37(10):2182, 1962. doi: 10.1063/1.1732985.

[47] L. Tumbek and A. Winkler. Attachment limited versus diffusion limited nucleation of organic molecules: Hexaphenyl on sputter-modified mica. *Surface Science*, 606(15-16), 2012. doi: 10.1016/j.susc.2012.03.018.

[48] A. Winkler and L. Tumbek. Nucleation of organic molecules via a hot precursor state: Pentacene on amorphous mica. *Journal of Physical Chemistry Letters*, 4(23):4080–4084, 2013. doi: 10.1021/jz402301v.

[49] Y. Lin, A. Böker, J. He, K. Sill, H. Xiang, C. Abetz, X. Li, J. Wang, T. Emrick, S. Long, Q. Wang, A. Balazs, and T. P. Russell. Self-directed self-assembly of nanoparticle/copolymer mixtures. *Nature*, 434(7029):55–59, mar 2005. doi: 10.1038/nature03310.

[50] R. Zhang, B. Li, M. C. Iovu, M. Jeffries-EL, G. Sauvé, J. Cooper, S. Jia, S. Tristram-Nagle, D. M. Smilgies, D. N. Lambeth, R. D. McCullough, and T. Kowalewski. Nanostructure Dependence of Field-Effect Mobility in Regioregular Poly(3-hexylthiophene) Thin Film Field Effect Transistors. *Journal of the American Chemical Society*, 128(11):3480–3481, mar 2006. doi: 10.1021/ja055192i.

[51] M. A. Ruderer, E. Metwalli, W. Wang, G. Kaune, S. V. Roth, and P. Müller-Buschbaum. Thin Films of Photoactive Polymer Blends. *ChemPhysChem*, 10(4):664–671, mar 2009. doi: 10.1002/cphc.200800773.

[52] Z. He, C. Zhong, S. Su, M. Xu, H. Wu, and Y. Cao. Enhanced power-conversion efficiency in polymer solar cells using an inverted device structure. *Nature Photonics*, 6(9):593–597, aug 2012. doi: 10.1038/nphoton.2012.190.

[53] M. Schubert, D. Dolfen, J. Frisch, S. Roland, R. Steyrleuthner, B. Stiller, Z. Chen, U. Scherf, N. Koch, A. Facchetti, and D. Neher. Influence of Aggregation on the Performance of All-Polymer Solar Cells Containing Low-Bandgap Naphthalenediimide Copolymers. *Advanced Energy Materials*, 2(3):369–380, mar 2012. doi: 10.1002/aenm.201100601.

[54] H. Ogawa, M. Takenaka, T. Miyazaki, A. Fujiwara, B. Lee, K. Shimokita, E. Nishibori, and M. Takata. Direct Observation on Spin-Coating Process of PS- b -P2VP Thin Films. *Macromolecules*, 49(9):3471–3477, may 2016. doi: 10.1021/acs.macromol.6b00049.

[55] A. Afzali, C. D. Dimitrakopoulos, and T. L. Breen. High-Performance, Solution-Processed Organic Thin Film Transistors from a Novel Pentacene Precursor. *Journal of the American Chemical Society*, 124(30):8812–8813, jul 2002. doi: 10.1021/ja0266621.

[56] W. Pisula, A. Menon, M. Stepputat, I. Lieberwirth, U. Kolb, A. Tracz, H. Sirringhaus, T. Pakula, and K. Müllen. A Zone-Casting Technique for Device Fabrication of Field-Effect Transistors Based on Discotic Hexa- peri -hexabenzocoronene. *Advanced Materials*, 17(6): 684–689, mar 2005. doi: 10.1002/adma.200401171.

[57] P. Miskiewicz, M. Mas-Torrent, J. Jung, S. Kotarba, I. Glowacki, E. Gomar-Nadal, D. B. Amabilino, J. Veciana, B. Krause, D. Carbone, C. Rovira, and J. Ulanski. Efficient High Area OFETs by Solution Based Processing of a π-Electron Rich Donor. *Chemistry of Materials*, 18(20):4724–4729, oct 2006. doi: 10.1021/cm060675m.

[58] Y. Nantsume, T. Minakata, and T. Aoyagi. Pentacene thin film transistors fabricated by solution process with directional crystal growth. *Organic Electronics*, 10(1):107–114, feb 2009. doi: 10.1016/j.orgel.2008.10.005.

[59] J. Zhou, Y. Zuo, X. Wan, G. Long, Q. Zhang, W. Ni, Y. Liu, Z. Li, G. He, C. Li, B. Kan, M. Li, and Y. Chen. Solution-Processed and High-Performance Organic Solar Cells Using Small Molecules with a Benzodithiophene Unit. *Journal of the American Chemical Society*, 135(23):8484–8487, jun 2013. doi: 10.1021/ja403318y.

[60] L. Casalis, M. F. Danisman, B. Nickel, G. Bracco, T. Toccoli, S. Iannotta, and G. Scoles. Hyperthermal Molecular Beam Deposition of Highly Ordered Organic Thin Films. *Physical Review Letters*, 90(20):206101, may 2003. doi: 10.1103/PhysRevLett.90.206101.

[61] T. Toccoli, A. Pallaoro, N. Coppedè, S. Iannotta, F. De Angelis, L. Mariucci, and G. Fortunato. Controlling field-effect mobility in pentacene-based transistors by molecular-beam deposition. *Applied Physics Letters*, 88(13):132106, 2006. doi: 10.1063/1.2187494.

[62] N. Coppedè, T. Toccoli, A. Pallaoro, F. Siviero, K. Walzer, M. Castriota, E. Cazzanelli, and S. Iannotta. Polymorphism and Phase Control in Titanyl Phthalocyanine Thin Films Grown by Supersonic Molecular Beam Deposition. *The Journal of Physical Chemistry A*, 111(49): 12550–12558, dec 2007. doi: 10.1021/jp075939m.

[63] E. R. Kish, R. K. Nahm, A. R. Woll, and J. R. Engstrom. When the Sequence of Thin Film Deposition Matters: Examination of Organic-on-Organic Heterostructure Formation Using Molecular Beam Techniques and in Situ Real Time X-ray Synchrotron Radiation. *The Journal of Physical Chemistry C*, 2016. doi: 10.1021/acs.jpcc.6b01717.

[64] A. J. Salih, S. P. Lau, J. M. Marshall, J. M. Maud, W. R. Bowen, N. Hilal, R. W. Lovitt, and P. M. Williams. Improved thin films of pentacene via pulsed laser deposition at elevated substrate temperatures. *Applied Physics Letters*, 69(15):2231, 1996. doi: 10.1063/1.117137.

[65] N. Matsumoto, H. Shima, T. Fujii, and F. Kannari. Organic electroluminescence cells based on thin films deposited by ultraviolet laser ablation. *Applied Physics Letters*, 71(17):2469, 1997. doi: 10.1063/1.120114.

[66] S. R. Farrar, A. E. A. Contoret, M. O'Neill, J. E. Nicholls, A. J. Eastwood, and S. M. Kelly. Pulsed-laser deposition for organic electroluminescent device applications. *Applied Physics Letters*, 76(18):2553, 2000. doi: 10.1063/1.126405.

[67] J. Götzen and G. Witte. Rapid preparation of highly ordered ultraflat ZnO surfaces. *Applied Surface Science*, 258(24):10144–10147, 2012. doi: 10.1016/j.apsusc.2012.06.094.

[68] M. Hara, H. Sasabe, A. Yamada, and A. F. Garito. Epitaxial Growth of Organic Thin Films by Organic Molecular Beam Epitaxy. *Japanese Journal of Applied Physics*, 28(Part 2, No. 2):L306–L308, feb 1989. doi: 10.1143/JJAP.28.L306.

[69] S. R. Forrest, P. E. Burrows, E. I. Haskal, and F. F. So. Ultrahigh-vacuum quasiepitaxial growth of model van der Waals thin films. II. Experiment. *Physical Review B*, 49(16): 11309–11321, apr 1994. doi: 10.1103/PhysRevB.49.11309.

[70] G. Yoshikawa, M. Kiguchi, S. Ikeda, and K. Saiki. Molecular orientations and adsorption structures of α-sexithienyl thin films grown on Ag and Ag surfaces. *Surface Science*, 559(2-3): 77–84, jun 2004. doi: 10.1016/j.susc.2004.04.045.

[71] Y. J. Bae, T. K. H. Pham, and T. H. Kim. Temperature-assisted morphological transition in CuPc thin films. *Journal of the Korean Physical Society*, 68(10):1206–1210, may 2016. doi: 10.3938/jkps.68.1206.

[72] G. Hlawacek, F. S. Khokhar, R. van Gastel, B. Poelsema, and C. Teichert. Smooth Growth of Organic Semiconductor Films on Graphene for High-Efficiency Electronics. *Nano Letters*, 11(2):333–337, feb 2011. doi: 10.1021/nl103739n.

[73] D. Schwarz, R. van Gastel, H. J. W. Zandvliet, and B. Poelsema. Size Fluctuations of Near Critical Nuclei and Gibbs Free Energy for Nucleation of BDA on Cu(001). *Physical Review Letters*, 109(1):016101, jul 2012. doi: 10.1103/PhysRevLett.109.016101.

[74] A. Al-Mahboob, Y. Fujikawa, T. Sakurai, and J. T. Sadowski. Real-Time Microscopy of Reorientation Driven Nucleation and Growth in Pentacene Thin Films on Silicon Dioxide. *Advanced Functional Materials*, 23(20):2653–2660, may 2013. doi: 10.1002/adfm.201203427.

[75] D. Schwarz, C. Henneke, and C. Kumpf. Towards functionalization of graphene: in situ study of the nucleation of copper-phtalocyanine on graphene. *New Journal of Physics*, 18(2):023034, feb 2016. doi: 10.1088/1367-2630/18/2/023034.

[76] B. Krause, F. Schreiber, H. Dosch, A. Pimpinelli, and O. H. Seeck. Temperature dependence of the 2D-3D transition in the growth of PTCDA on Ag(111): A real-time X-ray and kinetic Monte Carlo study. *Europhysics Letters (EPL)*, 65(3):372–378, 2004. doi: 10.1209/epl/i2003-10090-6.

[77] A. C. Mayer, R. Ruiz, H. Zhou, R. L. Headrick, A. Kazimirov, and G. G. Malliaras. Growth dynamics of pentacene thin films: Real-time synchrotron x-ray scattering study. *Physical Review B*, 73(20):1–5, 2006. doi: 10.1103/PhysRevB.73.205307.

[78] A. Amassian, T. Desai, S. Kowarik, S. Hong, A. Woll, G. Malliaras, F. Schreiber, and J. Engstrom. Coverage dependent adsorption dynamics in hyperthermal organic thin film growth. *Journal of Chemical Physics*, 130(12):1–9, 2009. doi: 10.1063/1.3088835.

[79] S. Kowarik, A. Gerlach, M. Skoda, S. Sellner, and F. Schreiber. Real-time studies of thin film growth: Measurement and analysis of X-ray growth oscillations beyond the anti-Bragg point. *European Physical Journal: Special Topics*, 167(1):11–18, 2009. doi: 10.1140/epjst/e2009-00930-y.

[80] S. Y. An, K. Ahn, D. Y. Kim, H.-H. Lee, J. H. Cho, and D. R. Lee. Real-time x-ray scattering study of the initial growth of organic crystals on polymer brushes. *The Journal of Chemical Physics*, 140(15):154702, 2014. doi: 10.1063/1.4870927.

[81] G. Renaud, R. Lazzari, C. Revenant, A. Barbier, M. Noblet, O. Ulrich, F. Leroy, J. Jupille, Y. Borensztein, C. R. Henry, J.-P. Deville, F. Scheurer, J. Mane-Mane, and O. Fruchart. Real-time monitoring of growing nanoparticles. *Science (New York, N.Y.)*, 300(5624):1416–1419, 2003. doi: 10.1126/science.1082146.

[82] J. D. Ferguson, G. Arikan, D. S. Dale, A. R. Woll, and J. D. Brock. Measurements of Surface Diffusivity and Coarsening during Pulsed Laser Deposition. *Physical Review Letters*, 103(25):256103, dec 2009. doi: 10.1103/PhysRevLett.103.256103.

[83] C. Frank, J. Novák, R. Banerjee, A. Gerlach, F. Schreiber, A. Vorobiev, and S. Kowarik. Island size evolution and molecular diffusion during growth of organic thin films followed by time-resolved specular and off-specular scattering. *Physical Review B*, 90(4):1–6, 2014. doi: 10.1103/PhysRevB.90.045410.

[84] M. Ruge, F. Golks, J. Zegenhagen, O. M. Magnussen, and J. Stettner. In operando GISAXS studies of mound coarsening in electrochemical homoepitaxy. *Physical Review Letters*, 112 (5):1–5, 2014. doi: 10.1103/PhysRevLett.112.055503.

[85] G. Binnig, C. F. Quate, and C. Gerber. Atomic Force Microscope. *Physical Review Letters*, 56(9):930–933, mar 1986. doi: 10.1103/PhysRevLett.56.930.

[86] J. Zhang, J. P. Rabe, and N. Koch. Grain-Boundary Evolution in a Pentacene Monolayer. *Advanced Materials*, 20(17):3254–3257, sep 2008. doi: 10.1002/adma.200703066.

[87] V. Kalihari, E. B. Tadmor, G. Haugstad, and C. D. Frisbie. Grain Orientation Mapping of Polycrystalline Organic Semiconductor Films by Transverse Shear Microscopy. *Advanced Materials*, 20(21):4033–4039, nov 2008. doi: 10.1002/adma.200801834.

[88] Y. Martin, C. C. Williams, and H. K. Wickramasinghe. Atomic force microscope-force mapping and profiling on a sub 100-Å scale. *Journal of Applied Physics*, 61(10):4723, 1987. doi: 10.1063/1.338807.

[89] P. Trtik, J. Kaufmann, and U. Volz. On the use of peak-force tapping atomic force microscopy for quantification of the local elastic modulus in hardened cement paste. *Cement and Concrete Research*, 42(1):215–221, jan 2012. doi: 10.1016/j.cemconres.2011.08.009.

[90] Á. S. Paulo and R. García. Unifying theory of tapping-mode atomic-force microscopy. *Physical Review B*, 66(4):041406, 2002. doi: 10.1103/PhysRevB.66.041406.

[91] A. J. Katan, M. H. van Es, and T. H. Oosterkamp. Quantitative force versus distance measurements in amplitude modulation AFM: a novel force inversion technique. *Nanotechnology*, 20(16):165703, 2009. doi: 10.1088/0957-4484/20/16/165703.

[92] J. Als-Nielsen and D. McMorrow. *Elements of Modern X-ray Physics: Second Edition*. Wiley, New York, 2011. ISBN 9780470973950. doi: 10.1002/9781119998365.

[93] S. K. Sinha, E. B. Sirota, S. Garoff, and H. B. Stanley. X-ray and neutron scattering from rough surfaces. *Physical Review B*, 38(4):2297–2311, aug 1988. doi: 10.1103/PhysRevB.38.2297.

[94] M. Birkholz. *Thin Film Analysis by X-Ray Scattering*. Wiley-VCH Verlag GmbH & Co. KGaA, Weinheim, FRG, oct 2005. ISBN 9783527607594. doi: 10.1002/3527607595.

[95] H. Kiessig. Interferenz von Röntgenstrahlen an dünnen Schichten. *Annalen der Physik*, 402 (7):769–788, 1931. doi: 10.1002/andp.19314020702.

[96] K. Tsujino, M. Matsumura, and Y. Nishimoto. Texturization of multicrystalline silicon wafers for solar cells by chemical treatment using metallic catalyst. *Solar Energy Materials and Solar Cells*, 90(1):100–110, jan 2006. doi: 10.1016/j.solmat.2005.02.019.

[97] L. Parratt. Surface studies of solids. *Physical Review*, 95(2):359, 1954.

[98] R. Ruiz, D. Choudhary, B. Nickel, T. Toccoli, K.-C. Chang, A. C. Mayer, P. Clancy, J. M. Blakely, R. L. Headrick, S. Iannotta, and G. G. Malliaras. Pentacene Thin Film Growth. *Chemistry of Materials*, 16(23):4497–4508, nov 2004. doi: 10.1021/cm049563q.

[99] C. L. Nicklin, M. J. Everard, C. Norris, and S. L. Bennett. Growth of ultrathin rare-earth films studied by in situ x-ray diffraction. *Physical Review B - Condensed Matter and Materials Physics*, 70(23):1–10, 2004. doi: 10.1103/PhysRevB.70.235413.

[100] S. Kowarik, A. Gerlach, S. Sellner, L. Cavalcanti, O. Konovalov, and F. Schreiber. Real-time X-ray diffraction measurements of structural dynamics and polymorphism in diindenoperylene growth. *Applied Physics A: Materials Science and Processing*, 95(1):233–239, 2009. doi: 10.1007/s00339-008-5012-2.

[101] A. R. Woll, T. V. Desai, and J. R. Engstrom. Quantitative modeling of in situ x-ray reflectivity during organic molecule thin film growth. *Physical Review B*, 84(7):1–14, 2011. doi: 10.1103/PhysRevB.84.075479.

[102] C. Weber, C. Frank, S. Bommel, T. Rukat, W. Leitenberger, P. Schäfer, F. Schreiber, and S. Kowarik. Chain-length dependent growth dynamics of n-alkanes on silica investigated by energy-dispersive x-ray reflectivity in situ and in real-time. *Journal of Chemical Physics*, 136 (20), 2012. doi: 10.1063/1.4719530.

[103] M. M. Soares, M. De Santis, H. C. N. Tolentino, A. Y. Ramos, M. El Jawad, Y. Gauthier, F. Yildiz, and M. Przybylski. Chemically ordered MnPt ultrathin films on Pt(001) substrate: Growth, atomic structure, and magnetic properties. *Physical Review B*, 85(20):205417, may 2012. doi: 10.1103/PhysRevB.85.205417.

[104] M. Sparenberg, A. Zykov, P. Beyer, L. Pithan, C. Weber, Y. Garmshausen, F. Carlà, S. Hecht, S. Blumstengel, F. Henneberger, and S. Kowarik. Controlling the growth mode of para-sexiphenyl (6P) on ZnO by partial fluorination. *Phys. Chem. Chem. Phys.*, 16(47): 26084–26093, 2014. doi: 10.1039/C4CP04048A.

[105] E. Kish. *Real Time In Situ X-Ray Studies Of Organic Heterostructure Formation*. PhD thesis, 2014.

[106] B. Krause, F. Schreiber, H. Dosch, a. Pimpinelli, and O. H. Seeck. Temperature dependence of the 2D-3D transition in the growth of PTCDA on Ag(111): A real-time X-ray and kinetic Monte Carlo study. *Europhysics Letters (EPL)*, 65(3):372–378, 2007. doi: 10.1209/epl/i2003-10090-6.

[107] V. I. Trofimov and V. G. Mokerov. Rate equations model for layer epitaxial growth kinetics. *Thin Solid Films*, 428(1-2):66–71, 2003. doi: 10.1016/S0040-6090(02)01272-5.

[108] M. Kalff, P. Šmilauer, G. Comsa, and T. Michely. No coarsening in Pt(111) homoepitaxy. *Surface Science*, 426(3):L447–L453, may 1999. doi: 10.1016/S0039-6028(99)00351-9.

[109] M. Schwartzkopf, A. Buffet, V. Körstgens, E. Metwalli, K. Schlage, G. Benecke, J. Perlich, M. Rawolle, A. Rothkirch, B. Heidmann, G. Herzog, P. Müller-Buschbaum, R. Röhlsberger, R. Gehrke, N. Stribeck, and S. Roth. From atoms to layers: in situ gold cluster growth kinetics during sputter deposition. *Nanoscale*, 5(11):5053–62, 2013. doi: 10.1039/c3nr34216f.

[110] T. Metzger, I. Kegel, R. Paniago, A. Lorke, J. Peisl, J. Schulze, I. Eisele, P. Schittenhelm, and G. Abstreiter. Shape, size, strain and correlations in quantum dot systems studied by

grazing incidence X-ray scattering methods. *Thin Solid Films*, 336(1-2):1–8, dec 1998. doi: 10.1016/S0040-6090(98)01290-5.

[111] C. Revenant, G. Renaud, R. Lazzari, and J. Jupille. Defect-pinned nucleation, growth, and dynamic coalescence of Ag islands on MgO(001): An in situ grazing-incidence small-angle x-ray scattering study. *Physical Review B*, 79(23):235424, jun 2009. doi: 10.1103/PhysRevB.79.235424.

[112] G. Kaune, M. A. Ruderer, E. Metwalli, W. Wang, S. Couet, K. Schlage, R. Röhlsberger, S. V. Roth, and P. Müller-Buschbaum. In Situ GISAXS Study of Gold Film Growth on Conducting Polymer Films. *ACS Applied Materials & Interfaces*, 1(2):353–360, feb 2009. doi: 10.1021/am8000727.

[113] C. Frank, R. Banerjee, M. Oettel, A. Gerlach, J. Novák, G. Santoro, and F. Schreiber. Analysis of island shape evolution from diffuse x-ray scattering of organic thin films and implications for growth. *Physical Review B*, 90:41–44, 2014. doi: 10.1103/PhysRevB.90.205401.

[114] R. Lazzari. IsGISAXS : a program for grazing-incidence small-angle X-ray scattering analysis of supported islands. *Journal of Applied Crystallography*, 35(4):406–421, aug 2002. doi: 10.1107/S0021889802006088.

[115] C. Durniak, M. Ganeva, G. Pospelov, W. van Herck, and J. Wuttke. BornAgain - Software for simulating and fitting X-ray and neutron small-angle scattering at grazing incidence. *http://www.bornagainproject.org*, 2015.

[116] E. S. R. F. Grenoble. What is a synchrotron? *http://www.esrf.eu/about/synchrotron-science/synchrotron*, 2016.

[117] C. Ponchut, J. M. Rigal, J. Clément, E. Papillon, A. Homs, and S. Petitdemange. MAXIPIX, a fast readout photon-counting X-ray area detector for synchrotron applications. *Journal of Instrumentation*, 6(01):C01069–C01069, jan 2011. doi: 10.1088/1748-0221/6/01/C01069.

[118] A. Zykov, S. Bommel, C. Wolf, L. Pithan, C. Weber, P. Beyer, G. Santoro, J. P. Rabe, and S. Kowarik. Diffusion and nucleation in multilayer growth of PTCDI-C8 studied with in situ X-ray growth oscillations and real-time small angle X-ray scattering. *The Journal of Chemical Physics*, 146(5):052803, feb 2017. doi: 10.1063/1.4961460.

[119] T. N. Krauss, E. Barrena, X. N. Zhang, D. G. de Oteyza, J. Major, V. Dehm, F. Würthner, L. P. Cavalcanti, and H. Dosch. Three-dimensional molecular packing of thin organic films of PTCDI-C8 determined by surface X-ray diffraction. *Langmuir : the ACS journal of surfaces and colloids*, 24(22):12742–12744, 2008. doi: 10.1021/la8030182.

[120] T. N. Krauss, E. Barrena, D. G. de Oteyza, X. N. Zhang, V. Dehm, F. Wu, and H. Dosch. X-ray / Atomic Force Microscopy Study of the Temperature-Dependent Multilayer Structure of PTCDI-C 8 Films on SiO 2. *The Journal of Physical Chemistry C*, 113(11):4502–4506, 2009. doi: 10.1021/jp808037w.

[121] P. R. L. Malenfant, C. D. Dimitrakopoulos, J. D. Gelorme, L. L. Kosbar, T. O. Graham, A. Curioni, and W. Andreoni. N-type organic thin-film transistor with high field-effect

mobility based on a N,N'-dialkyl-3,4,9,10-perylene tetracarboxylic diimide derivative. *Applied Physics Letters*, 80(14):2517–2519, 2002. doi: 10.1063/1.1467706.

[122] R. J. Chesterfield, J. C. McKeen, C. R. Newman, P. C. Ewbank, D. A. da Silva Filho, J. L. Brédas, L. L. Miller, K. R. Mann, and C. D. Frisbie. Organic thin film transistors based on N-alkyl perylene diimides: Charge transport kinetics as a function of gate voltage and temperature. *Journal of Physical Chemistry B*, 108(50):19281–19292, 2004. doi: 10.1021/jp046246y.

[123] A. L. Briseno, S. C. B. Mannsfeld, C. Reese, J. M. Hancock, Y. Xiong, S. A. Jenekhe, Z. Bao, and Y. Xia. Perylenediimide nanowires and their use in fabricating field-effect transistors and complementary inverters. *Nano Letters*, 7(9):2847–2853, 2007. doi: 10.1021/nl071495u.

[124] S. Karak, V. Reddy, S. Ray, and A. Dhar. Organic photovoltaic devices based on pentacene/N,N'-dioctyl-3,4,9,10-perylenedicarboximide heterojunctions. *Organic Electronics*, 10(5):1006–1010, 2009. doi: 10.1016/j.orgel.2009.04.006.

[125] M. Petit, R. Hayakawa, Y. Wakayama, and T. Chikyow. Early Stage of Growth of a Perylene Diimide Derivative Thin Film Growth on Various Si(001) Substrates. *The Journal of Physical Chemistry C*, 111(34):12747–12751, aug 2007. doi: 10.1021/jp071876w.

[126] S. Tatemichi, M. Ichikawa, T. Koyama, and Y. Taniguchi. High mobility n-type thin-film transistors based on N,N'-ditridecyl perylene diimide with thermal treatments. *Applied Physics Letters*, 89(11):13–16, 2006. doi: 10.1063/1.2349290.

[127] A. Buffet, A. Rothkirch, R. Döhrmann, V. Körstgens, M. M. Abul Kashem, J. Perlich, G. Herzog, M. Schwartzkopf, R. Gehrke, P. Müller-Buschbaum, and S. V. Roth. P03, the microfocus and nanofocus X-ray scattering (MiNaXS) beamline of the PETRA III storage ring: the microfocus endstation. *Journal of Synchrotron Radiation*, 19(4):647–653, jul 2012. doi: 10.1107/S0909049512016895.

[128] G. Santoro, A. Buffet, R. Döhrmann, S. Yu, V. Körstgens, P. Müller-Buschbaum, U. Gedde, M. Hedenqvist, and S. Roth. Use of intermediate focus for grazing incidence small and wide angle x-ray scattering experiments at the beamline P03 of PETRA III, DESY. *The Review of scientific instruments*, 85(4):043901, 2014. doi: 10.1063/1.4869784.

[129] T. V. Desai, A. R. Woll, F. Schreiber, and J. R. Engstrom. Nucleation and growth of perfluoropentacene on self-assembled monolayers: Significant changes in island density and shape with surface termination. *Journal of Physical Chemistry C*, 114(47):20120–20129, 2010. doi: 10.1021/jp107518f.

[130] J. Evans, P. Thiel, and M. Bartelt. Morphological evolution during epitaxial thin film growth: Formation of 2D islands and 3D mounds. *Surface Science Reports*, 61(1-2):1–128, 2006. doi: 10.1016/j.surfrep.2005.08.004.

[131] P. Hahn, J. Clabes, and M. Henzler. LEED-investigations and work-function measurements of the first stages of epitaxy of tungsten on tungsten (110). *Journal of Applied Physics*, 51 (4):2079, 1980. doi: 10.1063/1.327877.

[132] J. Yang, T. Wang, H. Wang, F. Zhu, G. Li, and D. Yan. Ultrathin-film growth of para-sexiphenyl (I): Submonolayer thin-film growth as a function of the substrate temperature. *Journal of Physical Chemistry B*, 112(26):7816–7820, 2008. doi: 10.1021/jp711455u.

[133] S. Lorbek, G. Hlawacek, and C. Teichert. Using Capture-Zone Scaling. *The European Physical Journal Applied Physics*, 55(2):23902, 2011. doi: 10.1051/epjap/2011100428.

[134] R. Ruiz, B. Nickel, N. Koch, L. C. Feldman, R. F. Haglund, A. Kahn, F. Family, and G. Scoles. Dynamic Scaling, Island Size Distribution, and Morphology in the Aggregation Regime of Submonolayer Pentacene Films. *Physical Review Letters*, 91(13):136102, sep 2003. doi: 10.1103/PhysRevLett.91.136102.

[135] A. S. Killampalli, T. W. Schroeder, and J. R. Engstrom. Nucleation of pentacene on silicon dioxide at hyperthermal energies. *Applied Physics Letters*, 87(3):033110, 2005. doi: 10.1063/1.1990254.

[136] H. Brune, G. S. Bales, J. Jacobsen, C. Boragno, and K. Kern. Measuring surface diffusion from nucleation island densities. *Physical Review B*, 60(8):5991–6006, aug 1999. doi: 10.1103/PhysRevB.60.5991.

[137] J. R. Morales-Cifuentes, T. Einstein, and A. Pimpinelli. How 'Hot Precursors' Modify Island Nucleation: A Rate-Equation Model. *Physical Review Letters*, 113(24):246101, 2014. doi: 10.1103/PhysRevLett.113.246101.

[138] P. A. Irvine, D. C. Wu, and P. J. Flory. Liquid-crystalline transitions in homologous p-phenylenes and their mixtures. Part 1.-Experimental results. *Journal of the Chemical Society, Faraday Transactions 1: Physical Chemistry in Condensed Phases*, 80(7):1795, 1984. doi: 10.1039/f19848001795.

[139] R. Resel, N. Koch, F. Meghdadi, G. Leising, L. Athouel, G. Froyer, and F. Hofer. A polymorph crystal structure of hexaphenyl observed in thin films. *Crystal Research and Technology*, 36 (1):47–54, 2001. doi: 10.1002/1521-4079(200101)36:1<47::AID-CRAT47>3.0.CO;2-X.

[140] B. Putsche, L. Tumbek, and A. Winkler. The influence of potassium on the growth of ultra-thin films of para-hexaphenyl on muscovite mica(001). *The Journal of Chemical Physics*, 137(13):134701, 2012. doi: 10.1063/1.4754833.

[141] H. Kirmse, M. Sparenberg, A. Zykov, S. Sadofev, S. Kowarik, and S. Blumstengel. Structure of p -Sexiphenyl Nanocrystallites in ZnO Revealed by High-Resolution Transmission Electron Microscopy. *Crystal Growth & Design*, 16(5):2789–2794, may 2016. doi: 10.1021/acs.cgd.6b00109.

[142] M. Kratzer, D. Wrana, K. Szajna, F. Krok, and C. Teichert. Island shape anisotropy in organic thin film growth induced by ion-beam irradiated rippled surfaces. *Phys. Chem. Chem. Phys.*, 16(47):26112–26118, oct 2014. doi: 10.1039/C4CP03356F.

[143] D. Wrana, M. Kratzer, K. Szajna, M. Nikiel, B. R. Jany, M. Korzekwa, C. Teichert, and F. Krok. Growth of para -Hexaphenyl Thin Films on Flat, Atomically Clean versus Air-Passivated TiO 2 (110) Surfaces. *The Journal of Physical Chemistry C*, 119(29):17004–17015, jul 2015. doi: 10.1021/acs.jpcc.5b04384.

[144] M. Kratzer and C. Teichert. Thin film growth of aromatic rod-like molecules on graphene. *Nanotechnology*, 27(29):292001, 2016. doi: 10.1088/0957-4484/27/29/292001.

[145] J. Novák, M. Oehzelt, S. Berkebile, M. Koini, T. Ules, G. Koller, T. Haber, R. Resel, and M. G. Ramsey. Crystal growth of para-sexiphenyl on clean and oxygen reconstructed Cu(110) surfaces. *Physical Chemistry Chemical Physics*, 13(32):14675, 2011. doi: 10.1039/c1cp20413k.

[146] H. Yanagi, K. Tamura, Y. Tanaka, and F. Sasaki. Optically pumped lasing from single-crystal cavity of p -phenylene oligomer. *Advances in Natural Sciences: Nanoscience and Nanotechnology*, 5(4):045013, nov 2014. doi: 10.1088/2043-6262/5/4/045013.

[147] C. Simbrunner. Epitaxial growth of sexi-thiophene and para-hexaphenyl and its implications for the fabrication of self-assembled lasing nano-fibres. *Semiconductor Science and Technology*, 28(5):053001, 2013. doi: 10.1088/0268-1242/28/5/053001.

[148] C. Simbrunner, G. Hernandez-Sosa, E. Baumgartner, G. Hesser, J. Roither, W. Heiss, and H. Sitter. Para-sexiphenyl-CdSe/ZnS nanocrystal hybrid light emitting diodes. *Applied Physics Letters*, 94(7):073505, 2009. doi: 10.1063/1.3086295.

[149] A. Andreev, F. Quochi, F. Cordella, A. Mura, G. Bongiovanni, H. Sitter, G. Hlawacek, C. Teichert, and N. S. Sariciftci. Coherent random lasing in the deep blue from self-assembled organic nanofibers. *Journal of Applied Physics*, 99(3):034305, 2006. doi: 10.1063/1.2161803.

[150] E. Zojer, N. Koch, P. Puschnig, F. Meghdadi, A. Niko, R. Resel, C. Ambrosch-Draxl, M. Knupfer, J. Fink, J. L. Brédas, and G. Leising. Structure, morphology, and optical properties of highly ordered films of para -sexiphenyl. *Physical Review B*, 61(24):16538–16549, jun 2000. doi: 10.1103/PhysRevB.61.16538.

[151] S. Tasch, C. Brandstätter, F. Meghdadi, G. Leising, G. Froyer, and L. Athouel. Red-green-blue light emission from a thin film electroluminescence device based on parahexaphenyl. *Advanced Materials*, 9(1):33, 1997. doi: 10.1002/adma.19970090105.

[152] T. Mikami and H. Yanagi. Epitaxial structuring of blue light-emitting p-phenylene oligomers. *Applied Physics Letters*, 73(5):563, 1998. doi: 10.1063/1.121856.

[153] H. Yanagi and T. Morikawa. Self-waveguided blue light emission in p-sexiphenyl crystals epitaxially grown by mask-shadowing vapor deposition. *Applied Physics Letters*, 75(2):187, 1999. doi: 10.1063/1.124314.

[154] C. Zhang, Z. Cui, H. Wang, D. Yan, Y. Li, Z. Shi, A. Wu, Z. Zhao, and S. Luan. Crystallization of sexiphenyl induced by polyurethane containing terphenyl groups affording high-mobility organic thin-film transistor. *Organic Electronics*, 15(10):2295–2301, oct 2014. doi: 10.1016/j.orgel.2014.04.027.

[155] K. N. Baker, A. V. Fratini, T. Resch, H. C. Knachel, W. Adams, E. Socci, and B. Farmer. Crystal structures, phase transitions and energy calculations of poly(p-phenylene) oligomers. *Polymer*, 34(8):1571–1587, apr 1993. doi: 10.1016/0032-3861(93)90313-Y.

[156] K. Palczynski, G. Heimel, J. Heyda, and J. Dzubiella. Growth and characterization of molecular crystals of Para -sexiphenyl by all-atom computer simulations. *Crystal Growth and Design*, 14(8):3791–3799, 2014. doi: 10.1021/cg500234r.

[157] G. R. Desiraju and A. Gavezzotti. Crystal structures of polynuclear aromatic hydrocarbons. Classification, rationalization and prediction from molecular structure. *Acta Crystallographica Section B Structural Science*, 45(5):473–482, oct 1989. doi: 10.1107/S0108768189003794.

[158] M. A. Heinrich, J. Pflaum, A. K. Tripathi, W. Frey, M. L. Steigerwald, and T. Siegrist. Enantiotropic Polymorphism in Di-indenoperylene. *The Journal of Physical Chemistry C*, 111(51):18878–18881, dec 2007. doi: 10.1021/jp0748967.

[159] D. Nabok, P. Puschnig, C. Ambrosch-Draxl, O. Werzer, R. Resel, and D.-M. Smilgies. Crystal and electronic structures of pentacene thin films from grazing-incidence x-ray diffraction and first-principles calculations. *Physical Review B*, 76(23):235322, dec 2007. doi: 10.1103/PhysRevB.76.235322.

[160] G. Horowitz, B. Bachet, A. Yassar, P. Lang, F. Demanze, J.-L. Fave, and F. Garnier. Growth and Characterization of Sexithiophene Single Crystals. *Chemistry of Materials*, 7(7):1337–1341, jul 1995. doi: 10.1021/cm00055a010.

[161] N. Kleppmann and S. H. L. Klapp. A scale-bridging modeling approach for anisotropic organic molecules at patterned semiconductor surfaces. *The Journal of Chemical Physics*, 142(6):064701, 2015. doi: 10.1063/1.4907037.

[162] L. Athouël, G. Froyer, M. Riou, and M. Schott. Structural studies of parasexiphenyl thin films: Importance of the deposition parameters. *Thin Solid Films*, 274(1-2):35–45, mar 1996. doi: 10.1016/0040-6090(95)07081-8.

[163] S. Zorba, Q. T. Le, N. J. Watkins, L. Yan, and Y. Gao. Morphology and Current-Voltage Characteristics of Nanostructured Pentacene Thin Films Probed by Atomic Force Microscopy. *Journal of Nanoscience and Nanotechnology*, 1(3):317–321, sep 2001. doi: 10.1166/jnn.2001.050.

[164] D. Käfer, L. Ruppel, and G. Witte. Growth of pentacene on clean and modified gold surfaces. *Physical Review B*, 75(8):085309, feb 2007. doi: 10.1103/PhysRevB.75.085309.

[165] C. Simbrunner, D. Nabok, G. Hernandez-Sosa, M. Oehzelt, T. Djuric, R. Resel, L. Romaner, P. Puschnig, C. Ambrosch-Draxl, I. Salzmann, G. Schwabegger, I. Watzinger, and H. Sitter. Epitaxy of Rodlike Organic Molecules on Sheet Silicates-A Growth Model Based on Experiments and Simulations. *Journal of the American Chemical Society*, 133(9):3056–3062, mar 2011. doi: 10.1021/ja109729e.

[166] M. B. Casu, S.-A. Savu, B.-E. Schuster, I. Biswas, C. Raisch, H. Marchetto, T. Schmidt, and T. Chassé. Island shapes and aggregation steered by the geometry of the substrate lattice. *Chemical Communications*, 48(55):6957, 2012. doi: 10.1039/c2cc31339a.

[167] L. Kilian, A. Hauschild, R. Temirov, S. Soubatch, A. Schöll, A. Bendounan, F. Reinert, T.-L. Lee, F. S. Tautz, M. Sokolowski, and E. Umbach. Role of Intermolecular Interactions on the

Electronic and Geometric Structure of a Large π-Conjugated Molecule Adsorbed on a Metal Surface. *Physical Review Letters*, 100(13):136103, apr 2008. doi: 10.1103/PhysRevLett.100.136103.

[168] J. Ikonomov, O. Bauer, and M. Sokolowski. Highly ordered thin films of perylene-3,4,9,10-tetracarboxylic acid dianhydride (PTCDA) on Ag(100). *Surface Science*, 602(12):2061–2068, jun 2008. doi: 10.1016/j.susc.2008.04.009.

[169] J. Ikonomov, C. H. Schmitz, and M. Sokolowski. Diffusion-limited island decay of PTCDA on Ag(100): Determination of the intermolecular interaction. *Physical Review B*, 81(19):195428, may 2010. doi: 10.1103/PhysRevB.81.195428.

[170] F. Della Sala, S. Blumstengel, and F. Henneberger. Electrostatic-field-driven alignment of organic oligomers on ZnO surfaces. *Physical Review Letters*, 107(14):1–5, 2011. doi: 10.1103/PhysRevLett.107.146401.

[171] K. Palczynski and J. Dzubiella. Anisotropic Electrostatic Friction of para -Sexiphenyl on the ZnO (101ÌĚ0) Surface. *The Journal of Physical Chemistry C*, 118(45):26368–26376, nov 2014. doi: 10.1021/jp507776h.

[172] L. Tumbek, C. Gleichweit, K. Zojer, and A. Winkler. Origin of the bimodal island size distribution in ultrathin films of para-hexaphenyl on mica. *Physical Review B - Condensed Matter and Materials Physics*, 86(8):1–11, 2012. doi: 10.1103/PhysRevB.86.085402.

[173] J. Götzen, D. Käfer, C. Wöll, and G. Witte. Growth and structure of pentacene films on graphite: Weak adhesion as a key for epitaxial film growth. *Physical Review B*, 81(8):085440, feb 2010. doi: 10.1103/PhysRevB.81.085440.

[174] C. Stadler, S. Hansen, I. Kröger, C. Kumpf, and E. Umbach. Tuning intermolecular interaction in long-range-ordered submonolayer organic films. *Nature Physics*, 5(2):153–158, 2009. doi: 10.1038/nphys1176.

[175] A. Gerlach, T. Hosokai, S. Duhm, S. Kera, O. T. Hofmann, E. Zojer, J. Zegenhagen, and F. Schreiber. Orientational ordering of nonplanar phthalocyanines on Cu(111): Strength and orientation of the electric dipole moment. *Physical Review Letters*, 106(15):1–4, 2011. doi: 10.1103/PhysRevLett.106.156102.

[176] O. L. A. Monti. Understanding interfacial electronic structure and charge transfer: An electrostatic perspective. *Journal of Physical Chemistry Letters*, 3(17):2342–2351, 2012. doi: 10.1021/jz300850x.

[177] Y. L. Huang, W. Chen, F. Bussolotti, T. C. Niu, A. T. S. Wee, N. Ueno, and S. Kera. Impact of molecule-dipole orientation on energy level alignment at the submolecular scale. *Physical Review B - Condensed Matter and Materials Physics*, 87(8):1–6, 2013. doi: 10.1103/PhysRevB.87.085205.

[178] K. Vasseur, K. Broch, A. L. Ayzner, B. P. Rand, D. Cheyns, C. Frank, F. Schreiber, M. F. Toney, L. Froyen, and P. Heremans. Controlling the Texture and Crystallinity of Evaporated Lead Phthalocyanine Thin Films for Near-Infrared Sensitive Solar Cells. *ACS Applied Materials & Interfaces*, 5(17):8505–8515, sep 2013. doi: 10.1021/am401933d.

[179] S. Kera, Y. Yabuuchi, H. Yamane, H. Setoyama, K. K. Okudaira, A. Kahn, and N. Ueno. Impact of an interface dipole layer on molecular level alignment at an organic-conductor interface studied by ultraviolet photoemission spectroscopy. *Physical Review B*, 70(8):085304, aug 2004. doi: 10.1103/PhysRevB.70.085304.

[180] H. Fukagawa, H. Yamane, S. Kera, K. K. Okudaira, and N. Ueno. Experimental estimation of the electric dipole moment and polarizability of titanyl phthalocyanine using ultraviolet photoelectron spectroscopy. *Physical Review B*, 73(4):041302, jan 2006. doi: 10.1103/PhysRevB.73.041302.

[181] H. Fukagawa, S. Hosoumi, H. Yamane, S. Kera, and N. Ueno. Dielectric properties of polar-phthalocyanine monolayer systems with repulsive dipole interaction. *Physical Review B*, 83(8):085304, feb 2011. doi: 10.1103/PhysRevB.83.085304.

[182] E. Wruss, O. T. Hofmann, D. A. Egger, E. Verwüster, A. Gerlach, F. Schreiber, and E. Zojer. Adsorption Behavior of Nonplanar Phthalocyanines: Competition of Different Adsorption Conformations. *The Journal of Physical Chemistry C*, 120(12):6869–6875, mar 2016. doi: 10.1021/acs.jpcc.6b00312.

[183] O. D. Jurchescu, J. Baas, and T. T. M. Palstra. Effect of impurities on the mobility of single crystal pentacene. *Applied Physics Letters*, 84(16):3061, 2004. doi: 10.1063/1.1704874.

[184] V. Coropceanu, J. Cornil, D. Silva, D. A, Y. Olivier, R. Silbey, J. L. Bredas, D. A. da Silva Filho, and J.-L. Brédas. Charge transport in organic semiconductors. *Chemical reviews*, 107 (4):926–52, 2007. doi: 10.1021/cr050140x.

[185] Q. Miao, M. Lefenfeld, T. Q. Nguyen, T. Siegrist, C. Kloc, and C. Nuckolls. Self-assembly and electronics of dipolar linear acenes. *Advanced Materials*, 17(4):407–412, 2005. doi: 10.1002/adma.200401251.

[186] S. Kaur, A. Gupta, V. Bhalla, and M. Kumar. Pentacenequinone derivatives: aggregation-induced emission enhancement, mechanism and fluorescent aggregates for superamplified detection of nitroaromatic explosives. *Journal of Materials Chemistry C*, 2(35):7356, jul 2014. doi: 10.1039/C4TC01194E.

[187] V. Bhalla, A. Gupta, M. Kumar, D. S. S. Rao, and S. K. Prasad. Self-Assembled Pentacenequinone Derivative for Trace Detection of Picric Acid. *ACS Applied Materials & Interfaces*, 5(3):672–679, feb 2013. doi: 10.1021/am302132h.

[188] V. U. Pandit, S. S. Arbuj, U. P. Mulik, and B. B. Kale. Novel Functionality of Organic 6,13-Pentacenequinone as a Photocatalyst for Hydrogen Production under Solar Light. *Environmental Science & Technology*, 48(7):4178–4183, apr 2014. doi: 10.1021/es405150p.

[189] Y. Sakamoto, T. Suzuki, M. Kobayashi, Y. Gao, Y. Inoue, and S. Tokito. Perfluoropentacene and Perfluorotetracene: Syntheses, Crystal Structures, and FET Characteristics. *Molecular Crystals and Liquid Crystals*, 444(1):225–232, feb 2006. doi: 10.1080/15421400500365011.

[190] B. Milián Medina, D. Beljonne, H.-J. Egelhaaf, and J. Gierschner. Effect of fluorination on the electronic structure and optical excitations of π-conjugated molecules. *The Journal of Chemical Physics*, 126(11):111101, 2007. doi: 10.1063/1.2713096.

[191] Y. Sakamoto, T. Suzuki, M. Kobayashi, Y. Gao, Y. Fukai, Y. Inoue, F. Sato, and S. Tokito. Perfluoropentacene: High-Performance p-n Junctions and Complementary Circuits with Pentacene. *Journal of the American Chemical Society*, 126(26):8138–8140, jul 2004. doi: 10.1021/ja0476258.

[192] I. Salzmann, S. Duhm, G. Heimel, J. P. Rabe, N. Koch, M. Oehzelt, Y. Sakamoto, and T. Suzuki. Structural Order in Perfluoropentacene Thin Films and Heterostructures with Pentacene. *Langmuir*, 24(14):7294–7298, jul 2008. doi: 10.1021/la800606h.

[193] S. Duhm, S. Hosoumi, I. Salzmann, A. Gerlach, M. Oehzelt, B. Wedl, T.-L. Lee, F. Schreiber, N. Koch, N. Ueno, and S. Kera. Influence of intramolecular polar bonds on interface energetics in perfluoro-pentacene on Ag(111). *Physical Review B*, 81(4):045418, jan 2010. doi: 10.1103/PhysRevB.81.045418.

[194] T. Breuer and G. Witte. Epitaxial growth of perfluoropentacene films with predefined molecular orientation: A route for single-crystal optical studies. *Physical Review B*, 83(15): 155428, apr 2011. doi: 10.1103/PhysRevB.83.155428.

[195] X. Wang, K. Broch, F. Schreiber, A. J. Meixner, and D. Zhang. Revealing nanoscale optical properties and morphology in perfluoropentacene films by confocal and tip-enhanced near-field optical microscopy and spectroscopy. *Phys. Chem. Chem. Phys.*, 18(23):15919–15926, 2016. doi: 10.1039/C6CP01153E.

[196] S. Kowarik, A. Gerlach, A. Hinderhofer, S. Milita, F. Borgatti, F. Zontone, T. Suzuki, F. Biscarini, and F. Schreiber. Structure, morphology, and growth dynamics of perfluoropentacene thin films. *physica status solidi (RRL) - Rapid Research Letters*, 2(3):120–122, jun 2008. doi: 10.1002/pssr.200802052.

[197] Y. Garmshausen, J. Schwarz, J. Hildebrandt, B. Kobin, M. Pätzel, and S. Hecht. Making Nonsymmetrical Bricks: Synthesis of Insoluble Dipolar Sexiphenyls. *Organic Letters*, 16(11): 2838–2841, jun 2014. doi: 10.1021/ol5009087.

[198] O. Werzer, N. Boucher, J. P. De Silva, G. Gbabode, Y. H. Geerts, O. Konovalov, A. Moser, J. Novak, R. Resel, and M. Sferrazza. Interface induced crystal structures of dioctylterthiophene thin films. *Langmuir*, 28(22):8530–8536, 2012. doi: 10.1021/la301213d.

[199] J. F. Moulin, F. Dinelli, M. Massi, C. Albonetti, R. Kshirsagar, and F. Biscarini. In situ X-ray synchrotron study of organic semiconductor ultra-thin films growth. *Nuclear Instruments and Methods in Physics Research, Section B: Beam Interactions with Materials and Atoms*, 246(1):122–126, 2006. doi: 10.1016/j.nimb.2005.12.008.

[200] H. A. van der Vegt, H. M. van Pinxteren, M. Lohmeier, E. Vlieg, and J. M. C. Thornton. Surfactant-induced layer-by-layer growth of Ag on Ag(111). *Physical Review Letters*, 68(22): 3335–3338, jun 1992. doi: 10.1103/PhysRevLett.68.3335.

[201] E. Weschke, C. Schüßler-Langeheine, R. Meier, G. Kaindl, C. Sutter, D. Abernathy, and G. Grübel. q Dependence of the Growth-Oscillation Period of X-Ray Reflectivity in Heteroepitaxy: Ho/W(110). *Physical Review Letters*, 79(20):3954–3957, 1997. doi: 10.1103/PhysRevLett.79.3954.

[202] A. Fleet, D. Dale, A. R. Woll, Y. Suzuki, and J. D. Brock. Multiple time scales in diffraction measurements of diffusive surface relaxation. *Physical Review Letters*, 96(5):2–5, 2006. doi: 10.1103/PhysRevLett.96.055508.

[203] M. Hanke, V. M. Kaganer, O. Bierwagen, M. Niehle, and A. Trampert. Delayed crystallization of ultrathin Gd2O3 layers on Si(111) observed by in situ X-ray diffraction. *Nanoscale Research Letters*, 7(1):203, 2012. doi: 10.1186/1556-276X-7-203.

[204] N. N. I. of Standards and Technology. Scattering Length Density Calculator. *http://www.ncnr.nist.gov/resources/sldcalc.html*, 2016.

[205] S. Kowarik, A. Gerlach, W. Leitenberger, J. Hu, G. Witte, C. Wöll, U. Pietsch, and F. Schreiber. Energy-dispersive X-ray reflectivity and GID for real-time growth studies of pentacene thin films. *Thin Solid Films*, 515(14 SPEC. ISS.):5606–5610, 2007. doi: 10.1016/j.tsf.2006.12.020.

[206] X. Zhang, E. Barrena, D. Goswami, D. G. De Oteyza, C. Weis, and H. Dosch. Evidence for a layer-dependent Ehrlich-Schwoebel barrier in organic thin film growth. *Physical Review Letters*, 103(13):1–4, 2009. doi: 10.1103/PhysRevLett.103.136101.

[207] J. R. Vig. UV/ozone cleaning of surfaces, 1985. ISSN 07342101.

[208] E. Cooper and G. J. Leggett. Static Secondary Ion Mass Spectrometry Studies of Self-Assembled Monolayers: Influence of Adsorbate Chain Length and Terminal Functional Group on Rates of Photooxidation of Alkanethiols on Gold. *Langmuir*, 14(22):4795–4801, 1998. doi: 10.1021/la9802567.

[209] W. R. Ashurst, C. Yau, C. Carraro, R. Maboudian, and M. T. Dugger. Dichlorodimethyisilane as an anti-stiction monolayer for MEMS: a comparison to the octadecyltrichlorosilane self-assembled monolayer. *Journal of Microelectromechanical Systems*, 9(1):41–49, 2001. doi: 10.1109/84.911090.

[210] L. Gao and T. J. Mccarthy. A Perfectly Hydrophobic Surface ($\Theta_A/\Theta_R = 180°/180°$). *Journal of the American Chemical Society*, 128(Figure 2):9052–9053, 2006. doi: 10.1021/ja062943n.

[211] F. Balzer, V. G. Bordo, A. C. Simonsen, and H.-G. Rubahn. Optical waveguiding in individual nanometer-scale organic fibers. *Physical Review B*, 67(11):115408, mar 2003. doi: 10.1103/PhysRevB.67.115408.

[212] C. Teichert, G. Hlawacek, A. Andreev, H. Sitter, P. Frank, A. Winkler, and N. Sariciftci. Spontaneous rearrangement of para-sexiphenyl crystallites into nano-fibers. *Applied Physics A*, 82(4):665–669, mar 2006. doi: 10.1007/s00339-005-3450-7.

[213] M. Schunack, T. R. Linderoth, F. Rosei, E. Lægsgaard, I. Stensgaard, and F. Besenbacher. Long Jumps in the Surface Diffusion of Large Molecules. *Physical Review Letters*, 88(15): 156102, mar 2002. doi: 10.1103/PhysRevLett.88.156102.

[214] D. Kandel. Initial stages of thin film growth in the presence of island-edge barriers. *Physical Review Letters*, 78(3):499–502, 1997. doi: 10.1103/PhysRevLett.78.499.

[215] G. Rosenfeld, N. N. Lipkin, W. Wulfhekel, J. Kliewer, K. Morgenstern, B. Poelsema, and G. Comsa. New concepts for controlled homoepitaxy. *Applied Physics A Materials Science & Processing*, 61(5):455–466, nov 1995. doi: 10.1007/BF01540247.

[216] I. Lange, S. Reiter, M. Pätzel, A. Zykov, A. Nefedov, J. Hildebrandt, S. Hecht, S. Kowarik, C. Wöll, G. Heimel, and D. Neher. Tuning the Work Function of Polar Zinc Oxide Surfaces using Modified Phosphonic Acid Self-Assembled Monolayers. *Advanced Functional Materials*, 24(44):7014–7024, nov 2014. doi: 10.1002/adfm.201401493.

[217] M. Riede, C. Uhrich, J. Widmer, R. Timmreck, D. Wynands, G. Schwartz, W.-M. Gnehr, D. Hildebrandt, A. Weiss, J. Hwang, S. Sundarraj, P. Erk, M. Pfeiffer, and K. Leo. Efficient Organic Tandem Solar Cells based on Small Molecules. *Advanced Functional Materials*, 21 (16):3019–3028, aug 2011. doi: 10.1002/adfm.201002760.

[218] Q. Zhang, X. Wan, F. Liu, B. Kan, M. Li, H. Feng, H. Zhang, T. P. Russell, and Y. Chen. Evaluation of Small Molecules as Front Cell Donor Materials for High-Efficiency Tandem Solar Cells. *Advanced Materials*, 28(32):7008–7012, aug 2016. doi: 10.1002/adma.201601435.

[219] V. Bhosle, J. T. Prater, F. Yang, D. Burk, S. R. Forrest, and J. Narayan. Gallium-doped zinc oxide films as transparent electrodes for organic solar cell applications. *Journal of Applied Physics*, 102(2):023501, 2007. doi: 10.1063/1.2750410.

[220] Y. H. Kim, J. S. Kim, W. M. Kim, T.-Y. Seong, J. Lee, L. Müller-Meskamp, and K. Leo. Realizing the Potential of ZnO with Alternative Non-Metallic Co-Dopants as Electrode Materials for Small Molecule Optoelectronic Devices. *Advanced Functional Materials*, 23(29): 3645–3652, aug 2013. doi: 10.1002/adfm.201202799.

[221] J. Bernède, L. Cattin, M. Morsli, and Y. Berredjem. Ultra-thin metal layer passivation of the transparent conductive anode in organic solar cells. *Solar Energy Materials and Solar Cells*, 92(11):1508–1515, nov 2008. doi: 10.1016/j.solmat.2008.06.016.

[222] P. K. Nayak, J. Yang, J. Kim, S. Chung, J. Jeong, C. Lee, and Y. Hong. Spin-coated Ga-doped ZnO transparent conducting thin films for organic light-emitting diodes. *Journal of Physics D: Applied Physics*, 42(3):035102, feb 2009. doi: 10.1088/0022-3727/42/3/035102.

[223] J. Stöhr. *NEXAFS Spectroscopy*, volume 25 of *Springer Series in Surface Sciences*. Springer Berlin Heidelberg, Berlin, Heidelberg, 1992. ISBN 978-3-642-08113-2. doi: 10.1007/978-3-662-02853-7.

[224] A. Nefedov and C. Wöll. *Advanced Applications of NEXAFS Spectroscopy for Functionalized Surfaces*, pages 277–303. Springer Berlin Heidelberg, Berlin, Heidelberg, 2013. ISBN 978-3-642-34243-1. doi: 10.1007/978-3-642-34243-1_10.

[225] I. M. Tidswell, B. M. Ocko, P. S. Pershan, S. R. Wasserman, G. M. Whitesides, and J. D. Axe. X-ray specular reflection studies of silicon coated by organic monolayers (alkylsiloxanes). *Physical Review B*, 41(2):1111–1128, jan 1990. doi: 10.1103/PhysRevB.41.1111.

[226] H. T. Yi, M. M. Payne, J. E. Anthony, and V. Podzorov. Ultra-flexible solution-processed organic field-effect transistors. *Nature communications*, 3(May):1259, 2012. doi: 10.1038/ncomms2263.

[227] B. Schmidt-Hansberg, M. Sanyal, M. F. G. Klein, M. Pfaff, N. Schnabel, S. Jaiser, A. Vorobiev, E. Müller, A. Colsmann, P. Scharfer, D. Gerthsen, U. Lemmer, E. Barrena, and W. Schabel. Moving through the phase diagram: Morphology formation in solution cast polymer-fullerene blend films for organic solar cells. *ACS Nano*, 5(11):8579–8590, 2011. doi: 10.1021/nn2036279.

[228] Z. Li, H. C. Wong, Z. Huang, H. Zhong, C. H. Tan, W. C. Tsoi, J. S. Kim, J. R. Durrant, and J. T. Cabral. Performance enhancement of fullerene-based solar cells by light processing. *Nature Communications*, 4:1–7, 2013. doi: 10.1038/ncomms3227.

[229] S. Blumstengel, S. Sadofev, and F. Henneberger. Electronic coupling of optical excitations in organic/inorganic semiconductor hybrid structures. *New Journal of Physics*, 10, 2008. doi: 10.1088/1367-2630/10/6/065010.

[230] S. Schiefer, M. Huth, A. Dobrinevski, and B. Nickel. Determination of the crystal structure of substrate-induced pentacene polymorphs in fiber structured thin films. *Journal of the American Chemical Society*, 129(34):10316–10317, 2007. doi: 10.1021/ja0730516.

[231] I. Salzmann, D. Nabok, M. Oehzelt, S. Duhm, A. Moser, G. Heimel, P. Puschnig, C. Ambrosch-Draxl, J. P. Rabe, and N. Koch. Structure solution of the 6, 13-pentacenequinone surface-induced polymorph by combining X-ray diffraction reciprocal-space mapping and theoretical structure modeling. *Crystal Growth and Design*, 11(2):600–606, 2011. doi: 10.1021/cg1015143.

[232] M. Schiek, F. Balzer, K. Al-Shamery, A. Lützen, and H.-G. Rubahn. Light-emitting organic nanoaggregates from functionalized p-quaterphenylenes. *Soft Matter*, 4(2):277–285, 2008. doi: 10.1039/B713295F.

[233] D. Kühne, F. Klappenberger, R. Decker, U. Schlickum, H. Brune, S. Klyatskaya, M. Ruben, and J. V. Barth. Self-Assembly of Nanoporous Chiral Networks with Varying Symmetry from Sexiphenyl-dicarbonitrile on Ag(111). *The Journal of Physical Chemistry C*, 113(41): 17851–17859, oct 2009. doi: 10.1021/jp9041217.

[234] F. Quochi, F. Cordella, A. Mura, G. Bongiovanni, F. Balzer, and H.-G. Rubahn. Gain amplification and lasing properties of individual organic nanofibers. *Applied Physics Letters*, 88(4):041106, 2006. doi: 10.1063/1.2167397.

[235] R. Resel. Crystallographic studies on hexaphenyl thin films - a review. *Thin Solid Films*, 433 (1-2):1–11, jun 2003. doi: 10.1016/S0040-6090(03)00312-2.

[236] R. Resel. Surface induced crystallographic order in sexiphenyl thin films. *Journal of Physics: Condensed Matter*, 20(18):184009, may 2008. doi: 10.1088/0953-8984/20/18/184009.

[237] P. Frank, G. Hlawacek, O. Lengyel, A. Satka, C. Teichert, R. Resel, and A. Winkler. Influence of surface temperature and surface modifications on the initial layer growth of para-hexaphenyl on mica (001). *Surface Science*, 601(10):2152–2160, 2007. doi: 10.1016/j.susc.2007.03.018.

[238] S. Sadofev, S. Blumstengel, J. Cui, J. Puls, S. Rogaschewski, P. Schäfer, and F. Henneberger. Visible band-gap ZnCdO heterostructures grown by molecular beam epitaxy. *Applied Physics Letters*, 89(20):201907, 2006. doi: 10.1063/1.2388250.

[239] L. O. Péres, F. Guillet, and G. Froyer. Easy synthesis of phenyl oligomers using a Ni complex. *Organic & biomolecular chemistry*, 2(4):452–454, 2004. doi: 10.1039/b400236a.

[240] D. Nečas and P. Klapetek. Gwyddion: an open-source software for SPM data analysis. *Central European Journal of Physics*, 10(1):181–188, jan 2012. doi: 10.2478/s11534-011-0096-2.

[241] D. Nabok, P. Puschnig, and C. Ambrosch-Draxl. Cohesive and surface energies of π -conjugated organic molecular crystals: A first-principles study. *Physical Review B - Condensed Matter and Materials Physics*, 77(24):1–4, 2008. doi: 10.1103/PhysRevB.77.245316.

[242] B. Scherwitzl, W. Lukesch, A. Hirzer, J. Albering, G. Leising, R. Resel, and A. Winkler. Initial Steps of Rubicene Film Growth on Silicon Dioxide. *The journal of physical chemistry. C, Nanomaterials and interfaces*, 117(8):4115–4123, 2013. doi: 10.1021/jp3122598.

[243] J. A. Blackman and P. A. Mulheran. Scaling behavior in submonolayer film growth: A one-dimensional model. *Physical Review B*, 54(16):681–692, 1996.

[244] D. W. Scott. On optimal and data-based histograms. *Biometrika*, 66(3):605–610, 1979. doi: 10.1093/biomet/66.3.605.

[245] A. Pimpinelli and T. L. Einstein. Capture-Zone Scaling in Island Nucleation: Universal Fluctuation Behavior. *Physical Review Letters*, 99(22):226102, nov 2007. doi: 10.1103/PhysRevLett.99.226102.

[246] A. Pimpinelli, L. Tumbek, and A. Winkler. Scaling and exponent equalities in island nucleation: Novel results and application to organic films. *Journal of Physical Chemistry Letters*, 5(6):995–998, 2014. doi: 10.1021/jz500282t.

[247] A. J. Fleming, F. P. Netzer, and M. G. Ramsey. Nucleation and 3D growth of para - sexiphenyl nanostructures from an oriented 2D liquid layer investigated by photoemission electron microscopy. *Journal of Physics: Condensed Matter*, 21(44):445003, nov 2009. doi: 10.1088/0953-8984/21/44/445003.

[248] K. Müllen and U. Scherf, editors. *Organic Light Emitting Devices*. Wiley-VCH Verlag GmbH & Co. KGaA, Weinheim, FRG, dec 2005. ISBN 9783527607983. doi: 10.1002/3527607986.

[249] A. O. F. Jones, B. Chattopadhyay, Y. H. Geerts, and R. Resel. Substrate-Induced and Thin-Film Phases: Polymorphism of Organic Materials on Surfaces. *Advanced Functional Materials*, 26(14):2233–2255, apr 2016. doi: 10.1002/adfm.201503169.

[250] P. J. Hotchkiss, H. Li, P. B. Paramonov, S. A. Paniagua, S. C. Jones, N. R. Armstrong, J.-L. Brédas, and S. R. Marder. Modification of the Surface Properties of Indium Tin Oxide with Benzylphosphonic Acids: A Joint Experimental and Theoretical Study. *Advanced Materials*, 21(44):4496–4501, nov 2009. doi: 10.1002/adma.200900502.

[251] P. Milauer and S. Harris. Determination of step-edge barriers to interlayer transport from surface morphology during the initial stages of homoepitaxial growth. *Physical Review B*, 51 (20):14798–14801, 1995. doi: 10.1103/PhysRevB.51.14798.

[252] J. Krug. On the shape of wedding cakes. *Journal of Statistical Physics*, 87(3-4):505–518, may 1997. doi: 10.1007/BF02181234.

[253] S. Müllegger and A. Winkler. Hexaphenyl thin films on clean and carbon covered Au(111) studied with TDS and LEED. *Surface Science*, 600(6):1290–1299, mar 2006. doi: 10.1016/j.susc.2006.01.018.